LSU Doctoral Dissertations   Graduate School

2014

Observations of Terrestrial Gamma Flashes with TETRA And LAGO

Rebecca Ringuette

Louisiana State University and Agricultural and Mechanical College, rebecca.ringuette@gmail.com

OBSERVATIONS OF TERRESTRIAL GAMMA FLASHES WITH
TETRA AND LAGO

A Dissertation

Submitted to the Graduate Faculty of the
Louisiana State University and
Agricultural and Mechanical College
in partial fulfillment of the
requirements for the degree of
Doctor of Philosophy

in

The Department of Physics & Astronomy

by
Rebecca A. Ringuette
B. S., Louisiana State University, 2007
M. S., Louisiana State University, 2013
August 2014

This dissertation is dedicated primarily to the God of Abraham, Isaac and Jacob who blessed me with this opportunity and gave me the strength to complete it. I also dedicate this work to my husband, my child and my mother, without whom it would have been extremely difficult.

ACKNOWLEDGEMENTS

TABLE OF CONTENTS

LIST OF TABLES

LIST OF FIGURES

LIST OF ABBREVIATIONS

+CG – Positive polarity cloud-to-ground (lightning)

+IC – Positive polarity intracloud (lightning)

-CG – Negative polarity cloud-to-ground (lightning)

-IC – Negative polarity intracloud (lightning)

^{214}Bi – Isotope 214 of Bismuth

^{214}Pb – Isotope 214 of Lead

ADC – Analog-to-digital Conversion

ADELE – Airborne Detector for Energetic Lightning Emissions

AGILE – Astro-Rivelatore Gamma a Immagini Leggero

ASEC – Aragats Space Environment Center

ATIC – Advanced Thin Ionization Calorimeter

BATSE – Burst and Transient Source Experiment

BGO – Bismuth Germanate

CEC – Coincident Event Candidate

CG – cloud-to-ground (lightning)

CPU – Central Processing Unit

CSBF – Columbia Scientific Ballooning Facility

CST – Central Standard Time

DAQ – Data AcQuisition software

dBZ – Decibels

e± – positron and electron

EC – Event Candidate

FEM – Front End Module

FPGA – Field-programmable Gate Array

FWHM – Full Width Half Maximum

GBM – Gamma ray Burst Monitor

GPS – Global Positional System

GRID – Gamma-Ray Imaging Detector

HASP – High Altitude Student Payload

HF – High Frequency (3 – 30 MHz)

IC – intracloud (lightning)

ICLRT – International Center for Lightning Research and Testing

kft – kilofeet (1000 feet)

$LaBr_3$ – Lanthanum Bromide

$LaBr_3$:Ce – Cerium-doped Lanthanum Bromide

LAT – Large Area Telescope

LAGO – Lightning Associated Gamma-ray Observer

LIS – Lightning Imaging Sensor

LSU – Louisiana State University

MiniCal – MiniCalorimeter

NaI – Sodium Iodide

NaI(Tl) – Thallium-doped Sodium Iodide

NASA – National Aerospace and Space Administration

NEXRAD – Next Generation Radar

NLDN – National Lightning Detection Network

NOAA – National Oceanic and Atmospheric Administration

NSSL – National Severe Storms Laboratory

OTD – Optical Transient Detector

PVC – Polyvinyl chloride

PMT – photomultiplier tube

QNX – Qunix

RHESSI – Reuven Ramaty High Energy Solar Spectroscopic Imager

RREA – Relativistic Runaway Electron Avalanche

sferic – atmosphere radio signal emitted by a lightning flash

STP – Standard Temperature and Pressure

TEB – Terrestrial Electron Beam

TERA – Thunderstorm Energetic Radiation Array

TETRA – TGF and Energetic Thunderstorm Rooftop Array

TGF – Terrestrial Gamma-ray Flashes

TLM – Trigger Logic Module

UTC – Coordinated Universal Time

USPLN – United States Precision Lightning Network

UV – Ultraviolet

VHF – Very High Frequency (30 – 300 MHz)

VIL – Vertically Integrated Liquid

VILD – Vertically Integrated Liquid Density

VLF – Very Low Frequency (3 – 30 kHz)

WWLLN – World Wide Lightning Location Network

ABSTRACT

Terrestrial Gamma ray Flashes (TGFs) -- very short, intense bursts of electrons, positrons, and energetic photons originating from terrestrial thunderstorms -- have been detected with satellite instruments. The TGF and Energetic Thunderstorm Rooftop Array (TETRA), an array of NaI(Tl) scintillators at Louisiana State University, has now been used to detect similar bursts of 50 keV to over 2 MeV gamma rays at ground level. After 3.3 years of observation, twenty-eight events with durations 0.02 - 4.2 msec have been detected associated with nearby lightning, three of them coincident events observed by detectors separated by ~1000 m. Nine of the events occurred within 6 msec and 3 miles of negative polarity cloud-to-ground lightning strokes with measured currents in excess of 20 kA. The events reported here constitute the first catalog of TGFs observed at ground level in close proximity to the acceleration site. The ability to observe ground-level Terrestrial Gamma Flashes from close to the source also allows a unique analysis of the storm cells producing these events. The results of this analysis are presented here.

In addition to the ground-based TETRA array, a balloon-borne detector (the Lightning-Associated Gamma-ray Observer, LAGO) has been constructed and flown. Results from an engineering flight of this balloon payload are presented. Plans for an upgraded version of the ground-based array are also included.

CHAPTER 1 – INTRODUCTION

Lightning provides the most powerful natural accelerator available on Earth for producing high energy particles. Intense millisecond-scale bursts of gamma rays produced by upward-moving electrons accelerated to energies of tens of MeV or more have been detected with satellite instruments. These Terrestrial Gamma-ray Flashes (TGFs) have been shown to be associated mainly with positive polarity intracloud lightning, with the particle acceleration occurring at altitudes of 10-15 km. We show that negative polarity cloud-to-ground lightning accelerates particles downward and produces gamma rays with energies of at least 2 MeV.

TGF observations from satellite platforms are limited to events apparently beamed upward and large enough to be detected even in the presence of attenuation and Compton scattering by the atmosphere. Although these events observed from space are extremely intense (gamma ray rates in excess of 300 kHz measured with the Burst And Transient Source Experiment) [Fishman et al., 1994], the bulk of the events are presumably smaller events which can only be observed much closer to the lightning -- i.e., at aircraft or balloon altitude or at ground level [Smith et al., 2011; Briggs et al., 2013; Gjesteland et al., 2012; Østgaard et al., 2012]. Observations at ground level and in the atmosphere are necessary to observe the downward component, to better understand the TGF intensity distribution and emission pattern, to understand whether the observed 30° beaming is intrinsic to the emission process or is the result of atmospheric attenuation, and to measure the spectrum vs altitude relationship. The present work describes a program to observe TGFs from the ground and at balloon altitudes and presents a summary of the events detected in the first three years of observation.

Chapter 2 introduces the scientific motivation for the project. Chapter 3 describes the ground-based TGF and Energetic Thunderstorm Rooftop Array (TETRA) experiment, the main focus of this work. Chapter 4 gives the initial published results for July 2010 to February 2013 (~2.5 years of data) acquired with TETRA and the associated data analysis for the initial observations. These results are summarized in Table 4.1. Chapter 5 updates the results, extending them to March 2014, using an improved data analysis process. The most current details of the TETRA results can be found in Table 5.1. An analysis of the storms that produced event candidates is given in chapter 6. In addition to the ground-based TETRA array, a balloon-borne detector (the Lightning-Associated Gamma ray Observer, LAGO) has been constructed and is described in chapter 7. Results from an engineering flight of this balloon payload are also found in chapter 7. Conclusions based on the TETRA and LAGO data are presented in chapter 8. Plans for an upgraded version of the ground-based array are described in chapter 9. Appendix A contains the schematics of the electronics boards used in the rooftop array. The schematics of the electronics boards used in the balloon payload are included in Appendix B. The analysis code used to analyze the TETRA and LAGO data is described in Appendix C and can be accessed at http://heastro.phys.lsu.edu/lsutgfcode.

CHAPTER 2 – MOTIVATION[†]

Terrestrial Gamma-ray Flashes (TGFs) were first observed by the Burst and Transient Source Experiment (BATSE) aboard the Compton Gamma Ray Observatory [Fishman et al., 1994; Gjesteland et al., 2012]. The time profiles of the initial twelve events reported are shown in Fig. 2.1. These bursts have shorter durations – about one millisecond or less -- than cosmic gamma-ray bursts and are correlated with terrestrial thunderstorms. The gamma-ray community was not convinced of the physical nature of these events until Reuven Ramaty High Energy Solar Spectroscopic Imager (RHESSI) published a map of 820 TGF detected by the satellite over six years of its operation (Fig. 2.2) [Grefenstette et al., 2009]. If indeed these events were caused by noise, then the events should be distributed randomly across the satellite's orbit. Instead, these events are concentrated over Central America, central Africa and Southeast Asia -- areas correlated with intense lightning. Figure 2.3 shows the annual number of lightning strikes per square kilometer detected by the National Aeronautics and Space Administration's (NASA's) Optical
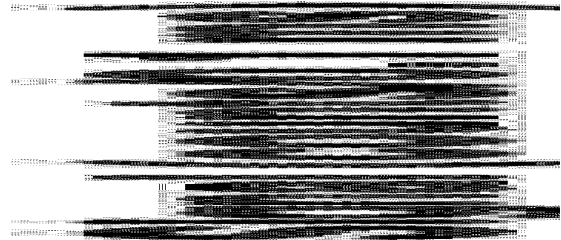
Figure 2.1 Time profiles of BATSE TGFs. The time resolution of the plots is 0.1 ms per bin. From Fishman et al., 1994.

[†]Portions of this chapter previously appeared in Ringuette, R., *et al.*, (2013), TETRA observation of gamma-rays at ground level associated with nearby thunderstorms. *J. Geophys. Res. Space Physics* **118**, 7841. It is licensed under CC 3.0.

Transient Detector (OTD) and Lightning Imaging Sensor (LIS) instruments. The comparison of the two figures shows clearly that these events are correlated with regions of high lightning density.
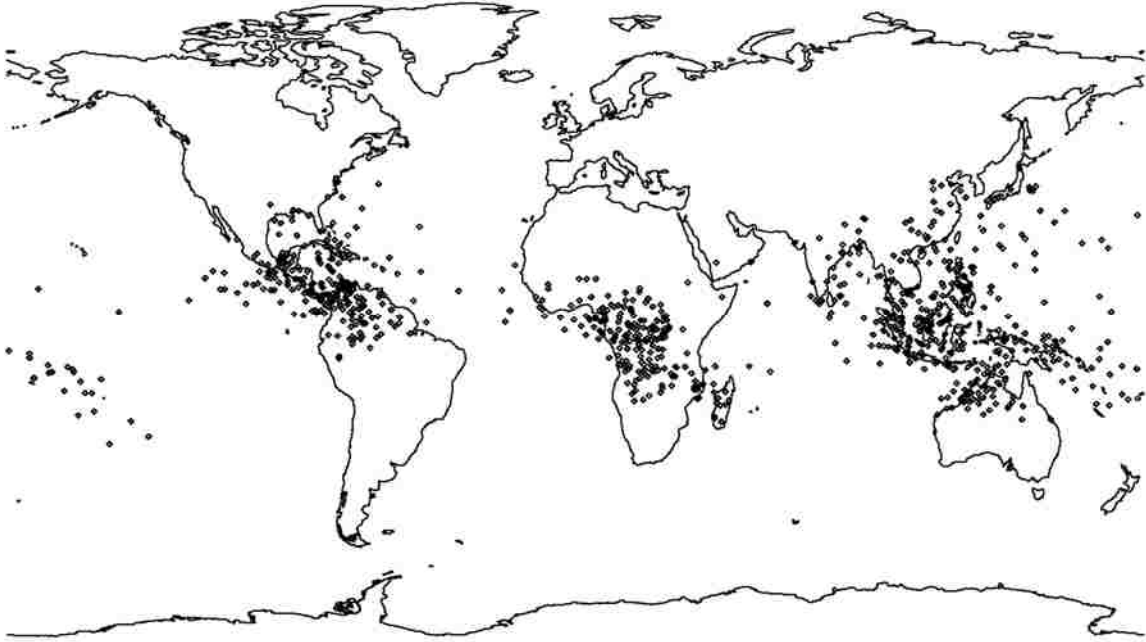
Fig. 2.2 Map of sub-satellite location for all 820 RHESSI TGFs. From Grefenstette et al., 2009.
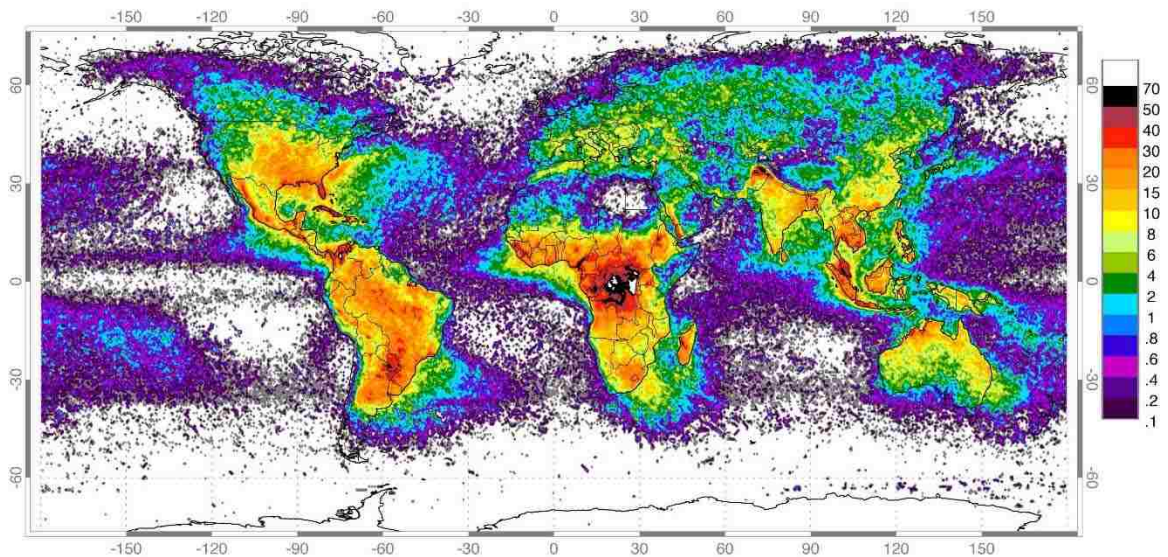
Fig. 2.3 High Resolution Full Climatology Annual Flash Rate. Global Distribution of lightning April 1995 - February 2003 from the combined observations of the NASA OTD (Apr 1995 – Mar 2000) and LIS (Jan 1998 – Feb 2003) instruments. From the National Weather Service.

Since the initial discovery of TGFs by the BATSE instrument, TGFs have now been observed by several additional satellite detectors including RHESSI [Smith et al., 2005; Grefenstette et al., 2009], the Gamma-Ray Imaging Detector (GRID) [Marisaldi et al., 2010] and MiniCALorimeter (MCAL) [Marisaldi et al., 2011; Tavani et al., 2011] on Astro-Rivelatore Gamma a Immagini Leggero (AGILE), and the Gamma ray Burst Monitor (GBM) [Cohen et al., 2010; Fishman et al., 2011; Briggs et al., 2013] and Large Area Telescope (LAT) [Grove et al., 2012] on the Fermi mission. A map of TGFs detected over Central America by GBM is shown in Fig. 2.4.
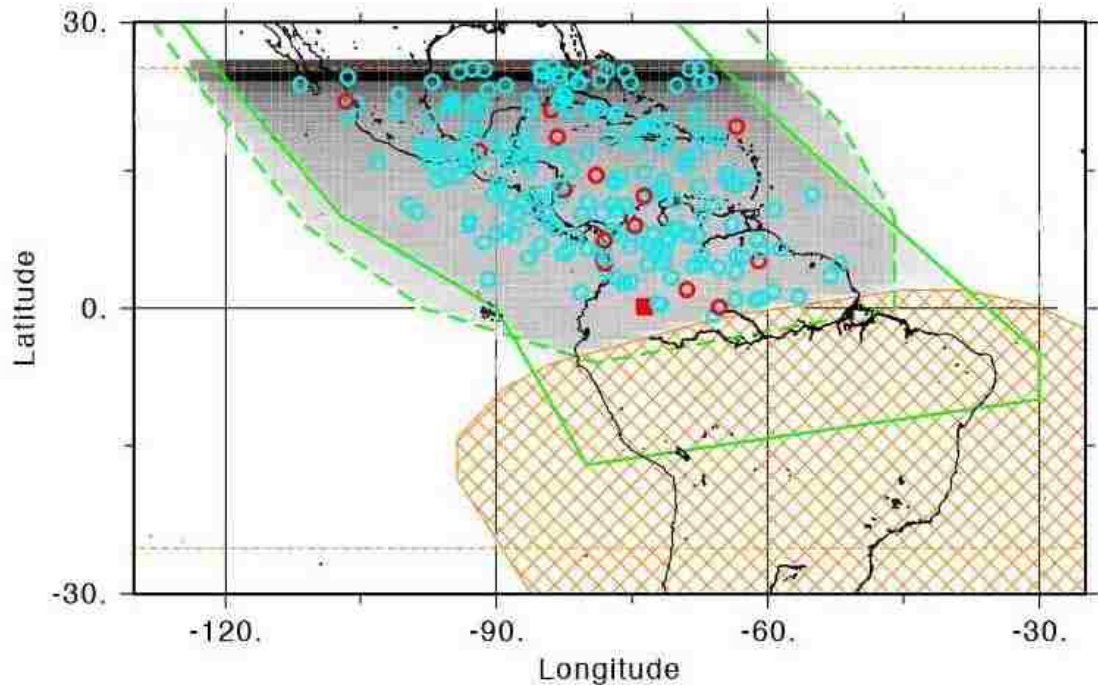
Figure 2.4 TGFs detected by GBM on the Fermi satellite. The cyan and red circles indicate 225 TGF detected in the Caribbean. From Briggs et al., 2013.

TGF events are typically detected close to the sub-satellite point [Grefenstette et al., 2009] and are correlated both with regions of high thunderstorm activity [Cohen et al., 2006; Fuschino et al., 2011; Marisaldi et al., 2011] and with individual positive polarity intracloud (+IC) and possibly positive polarity cloud-to-ground (+CG) lightning discharges to within 1 - 2 msec [Inan et al., 2006; Stanley et al., 2006; Hazelton et al., 2009]. (Positive polarity is needed to produce the upward beam of electrons and secondary photons necessary for detection of TGFs from space [Dwyer, 2003; Cohen et al., 2010].) Lightning flashes are known to emit a large fraction of their electromagnetic energy into low frequency (0.3 - 30 kHz) atmospheric radio signals, called sferics, which can be located accurately by arrival time measurements in a worldwide radio receiver network [Rodger et al., 2009]. TGFs are well correlated both with sferics [Inan et al., 2006; Connaughton et al., 2013] and the LIS-OTD (Fig. 2.3) and WWLLN high resolution lightning data [Hazelton et al., 2009; Smith et al., 2010; Fuschino et al., 2011].

GBM has also demonstrated that in some cases, as the original gammas propagate upward through the atmosphere, they produce secondary electron and positron (e±) via pair production [Cohen et al., 2010; Briggs et al., 2011] that escape into space. These secondaries are then able to spiral around magnetic field lines to the spacecraft far from the lightning location, producing Terrestrial Electron Beams (TEBs) characterized by 511 keV signals and both long duration pulses and delayed pulses resulting from particles moving past the spacecraft and then reflecting from magnetic mirror points and returning to be detected by GBM.

Given the altitude of the satellites around 500 km, the observations point to beaming of the photons upward with a ~30° half-angle cone coupled with attenuation of wide-angle photons passing through greater atmospheric path lengths [Grefenstette et al., 2008; Østgaard et al., 2008; Hazleton et al., 2009; Gjesteland et al., 2011]. Based on the spectra observed by RHESSI [Smith et al., 2005], Dwyer and Smith [2005] performed detailed Monte Carlo simulations showing that the spectra were consistent with bremsstrahlung from electrons accelerated by the relativistic runaway electron avalanche (RREA) mechanism [Gurevich et al., 1992; Dwyer, 2003] at altitudes near thunderstorm tops. Over the 0.1 - 10 MeV range, the spectrum observed by AGILE [Marisaldi et al., 2011] has been well fit by a cutoff power law of the form $F(E) \sim E^{-\alpha}e^{-E/E_o}$ with E_o compatible with the ~7 MeV electron energies predicted by RREA, but the observation of individual gamma rays with energies in excess of 40 MeV has posed a challenge for the emission models [Tavani et al., 2011; Celestin et al., 2012].

An accurate model of TGF production must account for many complex interactions. The primary factor involved in generating TGFs is the production of runaway electrons. In order for an electron to 'run away', it must gain energy from an electric field faster than it loses energy through ionization interactions and inelastic scattering [Wilson, 1925]. The effective frictional force that an electron must overcome is plotted against the electron's kinetic energy in Figure 2.5 (Dwyer, 2003). The minimum electric field strength at which this occurs is called the break-even field. The break-even field is defined as the field strength necessary for the average energy of a 1 MeV electron at standard temperature and pressure (STP) to remain constant as it gains energy from the electric field and loses energy in inelastic collisions with molecules and by emitting x-rays [Marshall et al., 1995]. With this definition, the break-even field is $E_b = 2.18 \times 10^5$ V/m $\times n$, where n is the density of air as compared to the air density at sea level [Dwyer, 2012a].

Electron energy losses in air increase with decreasing energy below ~1 MeV (with equivalent break-even field of eE_b), resulting in the curve on the left of Fig 2.5. Electrons with energies below ~0.1 keV (with equivalent break-even field of eE_c) are typically captured by ions as shown by the dip at the far left. For electrons with energies above 1.022 MeV -- twice the rest mass energy of two electrons -- bremsstrahlung emission and particle creation increase the effective frictional force, resulting in the dashed curve on the right. Including elastic scattering in the TGF model results in an increase in the strength of the break-even field by about 30% ($E_{th} = 2.84 \times 10^5$ V/m $\times n$), resulting in an electric field requirement comparable to those observed in thunderstorm clouds [Dwyer, 2012a; Rakov and Uman, 2003].

The production of runaway electrons is generally modeled beginning with energetic seed electrons with energies of a few MeV [Dwyer, 2003, 2008; Gjesteland et al., 2011]. These seed electrons have been argued to be produced by either cosmic ray air showers, cold runaway electrons, or lightning initiation processes [Gurevich, 1961; Dwyer, 2012a]. Cosmic ray air showers occur when a high energy proton or nucleus interacts with the atoms in the atmosphere, causing a shower of particles that decrease in energy as the shower altitude decreases. Cold runaway electrons are produced when the electric field exceeds the critical electric field strength (E_c in Fig. 2.5), causing the low-energy thermal electrons to run away. Recently, it has been shown that TGFs cannot be explained by cosmic rays or extensive cosmic ray air showers based on flux arguments [Dwyer, 2008]. The experimental association of TGFs with lightning suggests that TGFs are either seeded by cold runaway electrons produced by lightning leaders or the charge moment change in the early stages of lightning.
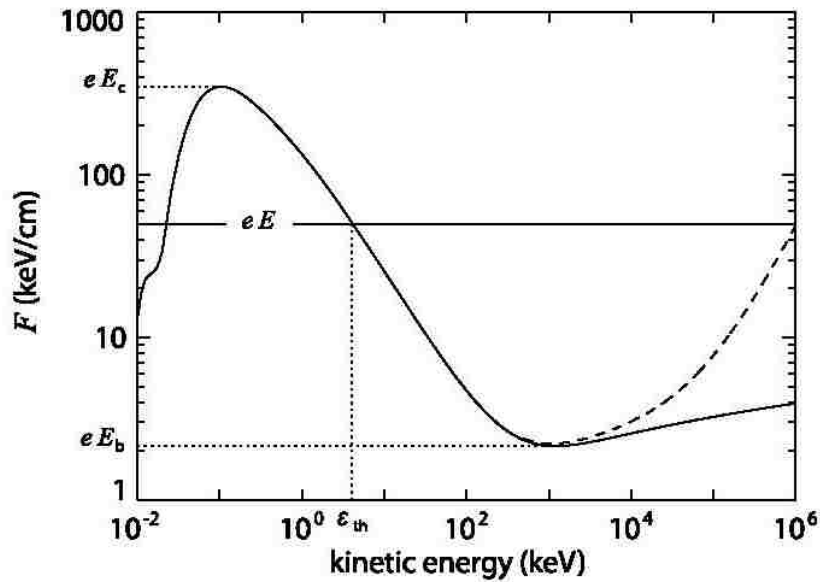
Figure 2.5 The effective frictional force experienced by a free electron moving through air at STP as a function of kinetic energy. The solid curve is due to inelastic scattering of the electron by air molecules, and the dashed curve indicates the effects of bremsstrahlung emission. The horizontal line shows the electric force from a 5.0×10^6 V/m electric field. Runaway electrons occur for kinetic energies greater than the threshold energy, $\varepsilon > \varepsilon_{th}$. Here E_c is the critical electric field strength for which low-energy thermal electrons will run away and E_b is the so-called breakeven field. Figure 1 from Dwyer, 2012a.

Runaway electrons produce avalanches with a characteristic energy scale of 7.2 MeV (Eq. 2.1). Using the electric field observed within thunderclouds ($E_{th} = 2.84 \times 10^5$ V/m $\times$ n), the runaway electron avalanche process produces a multiplication factor of 1.043. While this multiplication factor is large enough to produce a small avalanche, it is far below what is necessary for one seed electron to produce the ~10^{17} runaway electrons

observed by the BATSE, RHESSI and GBM instruments [Briggs et al., 2010]. For an electric field of 8×10^4 V/m $\times n$, as observed for negative polarity cloud-to-ground lightning, the multiplication factor increases to 8.031 – still far below observed TGF fluxes. This large flux difference between the standard avalanche model prediction and satellite TGF observations is resolved by including the relativistic feedback of positrons and backward-propagating x-rays.

Runaway electrons undergo avalanche multiplication due to Møller scattering (electron-electron elastic scattering), resulting in large numbers of runaway electrons for each initial seed electron as shown in the central portion of Fig. 2.6. When these relativistic electrons are deflected in the electric field of a nucleus, they emit bremsstrahlung X-rays, thus slowing the avalanche. A small portion of these X-rays Compton randomly backscatter towards the beginning of the avalanche region, producing more runaway electrons via Compton scattering or photoelectric absorption, causing a secondary avalanche (shown on the left in Fig. 2.6).
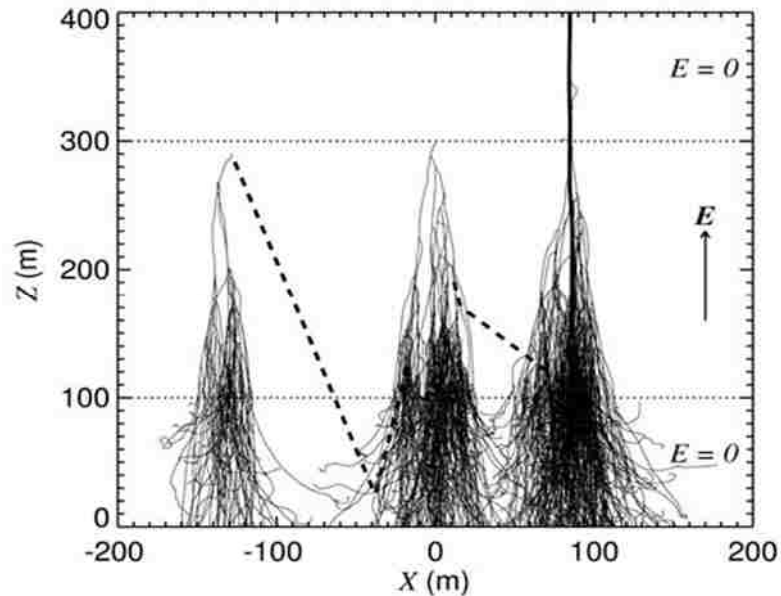
Fig. 2.6 Partial Monte Carlo simulation showing the runaway breakdown of air. The light tracks are the runaway electrons, the dashed lines are the gamma-rays and the dark track is a positron. The entire avalanche is initiated by one, 1 MeV, seed electron injected at the top center of the volume. The horizontal dotted lines show the boundaries of the electric field volume (E = 1000 kV/m). For clarity, only a small fraction of the runaway electrons and gamma-rays produced by the avalanche are plotted. The avalanches on the left and right illustrate the increase in the avalanche multiplication factors caused by the addition of the X-ray and positron feedback mechanisms, respectively. From Dwyer 2003a.

The backscattered X-rays can also pair produce, generating relativistic positrons traveling backwards in the electric field towards the avalanche region. As the positrons travel backwards, some emit secondary bremsstrahlung X-rays that can further seed the

avalanche (shown on the right in Fig. 2.6). They also interact with atomic electrons in the air via hard elastic scattering, producing additional runaway electrons that seed secondary avalanches. The positrons eventually annihilate, producing 511 keV gamma rays which can also increase the avalanche multiplication and produce a possible downward-directed positron and gamma ray signature [Dwyer 2012a]. This runaway mechanism is referred to as the relativistic runaway avalanche mechanism (RREA), or the 'snowball effect' [Wilson, quoted in Williams, 2010].

These relativistic feedback mechanisms lengthen TGF durations up to several milliseconds and explain the flux seen from TGFs at satellite altitudes [Dwyer, 2008; Dwyer et al., 2012a and references therein]. Ground-based lightning observations and comparisons of model calculations with the measured spectra indicate that the TGFs are produced at altitudes ~ 10-15 km [Dwyer and Smith, 2005; Grefenstette et al., 2008; Shao et al., 2010; Gjesteland et al., 2010; Cummer et al., 2011; Xu et al., 2012]. As a practical consideration, it has been suggested that lightning-induced gamma rays might produce a significant radiation exposure for airplane passengers flying close to a lightning stroke [Dwyer et al., 2010]. A more detailed review of TGF models and observations is presented by Dwyer et al. [2012b].

The majority of ground-level observation projects currently focus on correlating satellite-observed TGFs with lightning and measuring possible associated magnetic signatures [Cummer et al., 2011; Lu et al., 2011]. The International Center for Lightning Research and Testing (ICLRT) project, however, has reported two gamma ray bursts, one in association with triggered lightning of negative polarity [Dwyer et al., 2004] and another in association with nearby negative polarity cloud-to-ground (-CG) lightning [Dwyer et al., 2012c]. TGFs associated with negative polarity lightning strikes, as with these ICLRT events, produce downward beams of photons which can be detected from the ground. ICLRT operates in a triggered mode, requiring either a triggered lightning current above 6 kA or the simultaneous trigger of two optical sensors.

Other observations of gamma-rays from thunderstorms have been reported, although these events show different characteristics from the TGFs described here. The array of particle detectors at Aragats Space Environment Center (ASEC) has detected thunderstorm-associated ground enhancements above 7 MeV with timescales of microseconds and tens of minutes [Chilingarian et al., 2010, 2011]. These have been detected approximately once per year and seem to be correlated with -IC lightning. Longer duration (40 seconds to minutes or longer) X-ray and gamma ray events have been reported previously from the ground [Tsuchiya et al., 2011, 2013]. In comparison, only the two ICLRT events exhibit the same spectral properties and the same timescale as the TGFs detected from space. The only other case in which a TGF-like event with millisecond emission of MeV gammas has been observed from within the atmosphere is the observation by the Airborne Detector for Energetic Lightning Emissions (ADELE) aboard an aircraft at an altitude of 14 km [Smith et al., 2011].

Observations of TGFs from the ground are necessary to resolve several detection issues. Although hundreds of TGFs have been detected from space, satellites have difficulty

distinguishing low flux events from the observed background. For upward-directed TGFs, the predicted positron signature must be observed from beneath the source. Also, the location uncertainty of the majority of these events is 300 km – much larger than individual thunderstorm cells [Briggs et al., 2013]. By monitoring with a ground-based detection array, we are able to detect TGFs, associate them with specific portions of thunderstorms, and look for trends between the TGFs and the properties of the storms producing them. Here we present observations from July 2010 through October 2013 of twenty-eight TGF-like events in which 50 keV - 2 MeV gamma rays are observed at ground level in shorter than 5 msec bursts associated with nearby negative polarity lightning. These observations increase the number of TGFs detected from the ground by a factor of 14, compared to the two previously known TGFs detected from the ground by ICLRT.

CHAPTER 3 – TETRA DETECTOR DESCRIPTION[†]

The TGF and Energetic Thunderstorm Rooftop Array (TETRA) consists of an array of twelve 19 cm × 19 cm × 5 mm Thallium-doped sodium iodide (NaI(Tl)) scintillators designed to detect the gamma ray emissions from nearby lightning flashes over the range 50 keV - 2 MeV. The scintillators are mounted in four detector boxes, each containing three sodium iodide (NaI) detectors viewed by individual photomultiplier tubes (PMTs) (pictured in Fig. 3.1). The boxes are spaced at the corners of a ~700 × 1300 m^2 area on four high rooftops at the Baton Rouge campus of Louisiana State University (LSU) at latitude 30.41º and longitude -91.18 º (Fig. 3.2). Unlike ICLRT, TETRA operates in a self-triggered mode, allowing for events to be recorded without requiring the direct detection of lightning.

Figure 3.1 One of the four TETRA detector boxes. The boxes are covered with Mylar to reflect ultraviolet (UV) radiation. The PVC curved pipes shown are to promote air flow through the box. This box is located on the roof of the LSU School of Veterinary Medicine. The Mississippi River can be seen in the background.

Each TETRA detector box contains three NaI scintillator plates oriented at 30° from the zenith direction and separated by 120° in azimuth (Fig 3.2). Each NaI(Tl) crystal is hermetically sealed between a 6.4 mm thick glass optical window on one flat face and a 0.75 mm thick Aluminum entrance window on the other face. An ultraviolet transmitting Lucite lightguide is coupled to the glass window, and the light is viewed by an Electron Tubes 9390KB 130 mm photomultiplier tube (PMT) with a standard bialkali

[†]Portions of this chapter previously appeared in Ringuette, R., *et al.*, (2013), TETRA observation of gamma-rays at ground level associated with nearby thunderstorms. *J. Geophys. Res. Space Physics* **118**, 7841. It is licensed under CC 3.0.
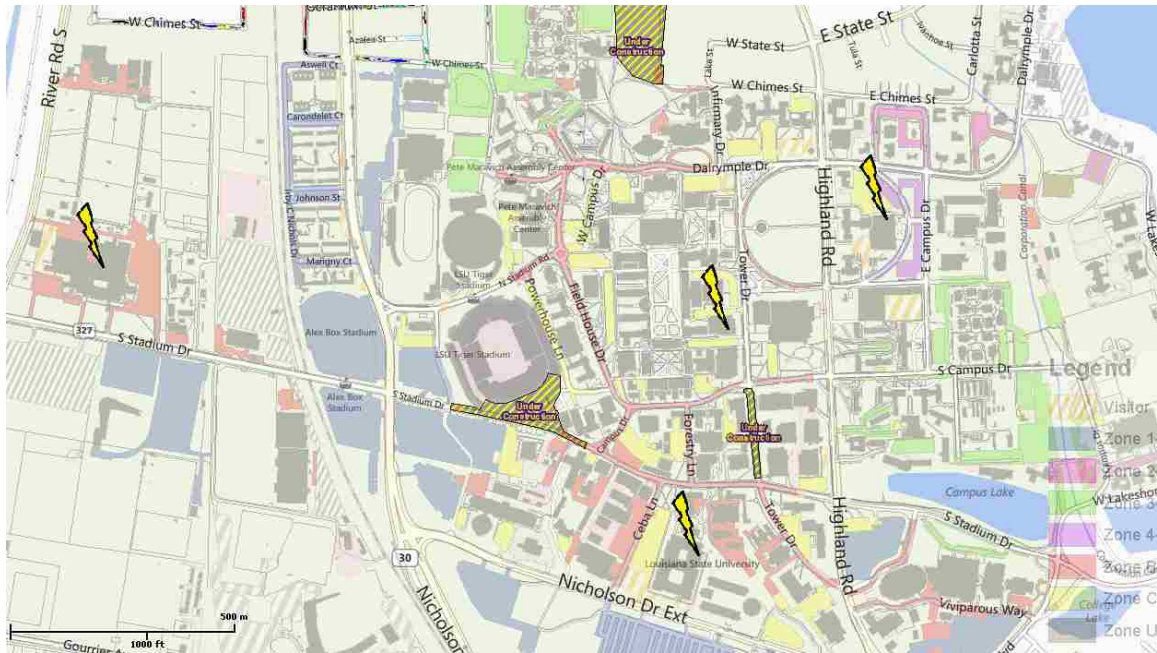
Figure 3.2 Map of TETRA detection box locations. A map of the campus of LSU is shown. The lightning symbols mark the locations of the four TETRA detection boxes.

photocathode (Fig 3.3, PMT electronics shown in Fig 3.4). The scintillator-PMT assemblies are housed in $\sim 1''$ thick plastic foam insulation to prevent rapid temperature changes. Electronics boards in each detector box supply high voltage, amplify and shape the PMT outputs, provide an internal trigger for the data acquisition software, digitize the data, assign timestamps, and record analog-to-digital conversion (ADC) values for each event. Once triggered, each PMT anode output is integrated and assigned a 12-bit ADC value. A detailed description of the electronics used in TETRA is given in Appendix A. A 32-channel 12-bit ADC board, a Lassan iQ Global Positional System (GPS) board, and a Mesa Field-programmable Gate Array (FPGA) board are incorporated onto a PC104 stack controlled by a Microcomputer Systems VDX-6357 800 MHz 486 Central Processing Unit (CPU) board running a Qunix (QNX) operating system. The FPGA is programmed to handle trigger logic, clock functionality, and event time stamping. We refer to the Mesa board together with its FPGA as the Trigger Logic Module (TLM). Each is capable of detecting events at a sustained rate of 30 kHz and a burst rate of up to 70 kHz. The data are then transferred over a wireless link to a central station for analysis. The initial version of the data acquisition software, used from October 2010 to January 2013, utilized a network time protocol to keep timestamps accurate to within approximately 2 msec and to monitor the absolute timing uncertainty. The current version of the software, implemented in January 2013, uses a GPS-disciplined clock to produce timestamps accurate to within 200 ns. This improvement in timing accuracy will improve detection significance by a factor of 10^4 for events observed on more than one detection box.

The ADC-to-energy conversion is calibrated with radioactive sources (^{22}Na, ^{137}Cs, ^{60}Co). Individual detector energy resolution ranges from 9 to 13.5% full width half maximum

11

Figure 3.3 Inside a TETRA detection box. The three foam blocks house the NaI PMTs described above. The electronics boards are located at the bottom right. The PC104 stack is located at the bottom left. Power and Ethernet cabling is to the left (not shown).

Figure 3.4 One of TETRA's NaI PMT assemblies. The 19 cm x 19 cm x 5 mm NaI(Tl) scintillator is shown at the bottom of the assembly. The clear prism in the middle is the acrylic light guide described above. A 130mm PMT views the light guide from the top, shown wrapped in electrical tape. This assembly is turned upside-down in the detection box to view gamma rays from thunderstorms.

(FWHM) at 662 keV and from 5.5 to 10.8% at 1.3 MeV. The total interaction probability in the NaI scintillators is 95% at 100 keV, 82% at 500 keV, and 10% at 1 MeV (with photoelectric interaction probabilities 93%, 26%, and 0.63% respectively). In addition to the three NaI scintillators, one detector box contains a one inch diameter by one inch thick cerium-doped lanthanum bromide (LaBr$_3$:Ce) scintillator that provides high energy resolution measurements (3.5% FWHM at 662 keV) of intense events. Beginning in October 2012, all boxes contain a bare PMT (photomultiplier tube without a scintillator) to check for electronic noise.
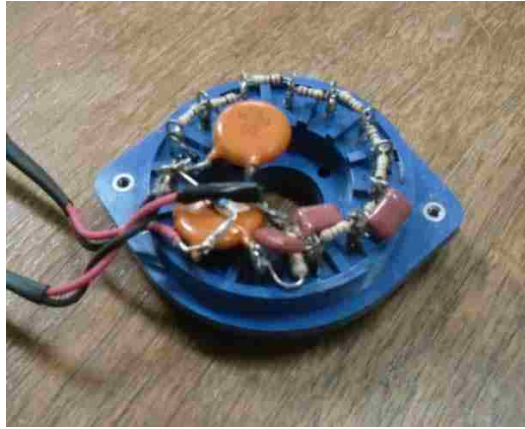
Figure 3.5 Standard voltage divider used for TETRA's NaI PMTs.

Data are accumulated for a day at a time for each of the four detector boxes individually. The daily analysis software selects events with signals corresponding to at least 50 keV deposited energy within 1 μsec. The data are then binned into 2 msec bins and assigned a timestamp. TETRA triggers are selected with counts/2 msec at least 20 standard deviations above the mean for the day. Once days with excessive electronic noise or other instrumental problems are removed, there are 835.09 days of live time and 1303 TETRA triggers.

CHAPTER 4 – TETRA DATA ANALYSIS AND RESULTS: JULY 2010 TO FEBRUARY 2013[†]

In Fig. 4.1, the heavy black line shows a time history of the count rates for the three NaI photomultiplier tubes of > 50 keV events in a single detector box for one day. The total count rate, plotted in counts per minute, is reasonably constant for the first seventeen hours, and then increases by a factor of approximately 2 beginning at about 1800 Central Standard Time (CST). The small peak in the count rate seen at about 1200 CST is due to noise in the system seen only in a single PMT on a 60-second timescale. The thin black histogram near the bottom shows the local radar reflectivity in decibels (dBZ) acquired from www.wunderground.com, indicating rain, thunderstorms, hail, or strong winds. The increase in the NaI detector rate is clearly correlated with the radon fallout caused by rainstorms. The gamma ray spectrum, measured during a rain event with the high
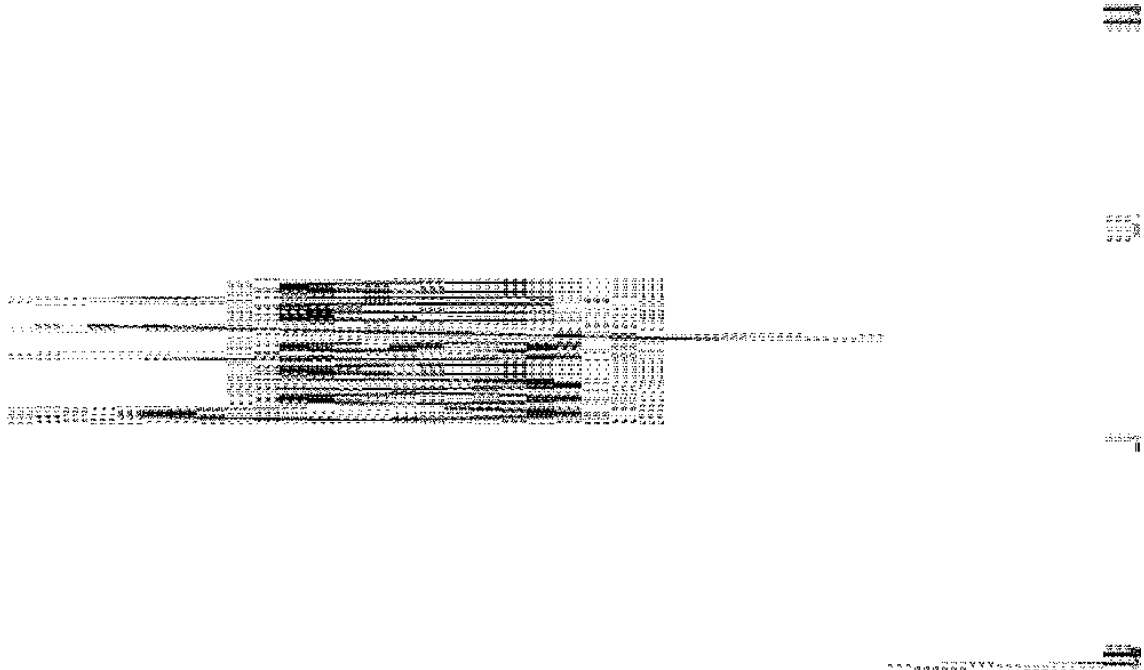
Figure 4.1 Summed NaI counting rate per minute in Box 3 on 8/18/2011 (heavy black line, left hand scale). Thin black histogram near the bottom (right hand scale) shows radar reflectivity. The filled rectangle at the bottom marks times of lightning strikes within 5 miles. The row of filled circles near the top marks intervals in which the count rate in 60 sec bins exceeds the day's average by 3 σ; the open square marks the TETRA trigger, i.e., the interval when the rate in 2 msec bins exceeds the day's average by 20 σ.

resolution LaBr$_3$:Ce detector mounted together with the NaI detectors in one of the detector boxes, shows a clear indication of 295, 352, 609, 1120, and 1764 keV ^{214}Bi and ^{214}Pb lines characteristic of radon decay (Fig. 4.2).

The filled rectangle near the bottom of Fig. 4.1 at approximately 1800 CST marks the times of lightning strikes detected by the United States Precision Lightning Network (USPLN) Unidata Program within 5 miles of the LSU campus. These are mainly cloud-to-ground events with positions accurate to approximately ¼ - ½ mile. In the upper section of the diagram, the line of filled circles marks 60-second intervals in which the NaI detector count rate is 3 standard deviations higher than the average rate for the day; these are correlated with the peak of the extended rise at the time of the rainstorms. TETRA triggers are defined as intervals during which the rate in a 2 msec window exceeds the day's average by 20 σ. The TETRA trigger observed is indicated near the top of the plot as an open square. (For a typical average counting rate of 8900 min^{-1} in a detector box above 50 keV, a 20 σ excess corresponds to 10 counts in the three PMTs in a detector box within a 2 msec window.)
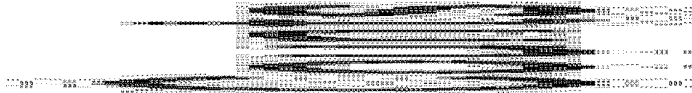
Figure 4.2 LaBr$_3$:Ce Rain Spectrum. LaBr$_3$:Ce background-subtracted spectrum during a 6 hour precipitation event showing radon lines at 295 keV, 352 keV, 609 keV, 1120 keV and 1764 keV.

Figure 4.3 shows an expanded view of the data on the same day, illustrating the correlation of the triggers in individual boxes with lightning and cloud density overhead. Panel A shows the times of the triggers in each detector box. Panel B shows the rate per second of lightning strikes within 5 miles of the detectors, and Panel C shows the distance of all lightning strikes recorded by the USPLN network within 100 miles. Panel D shows the overhead cloud density as measured by Next Generation Radar (NEXRAD) data.
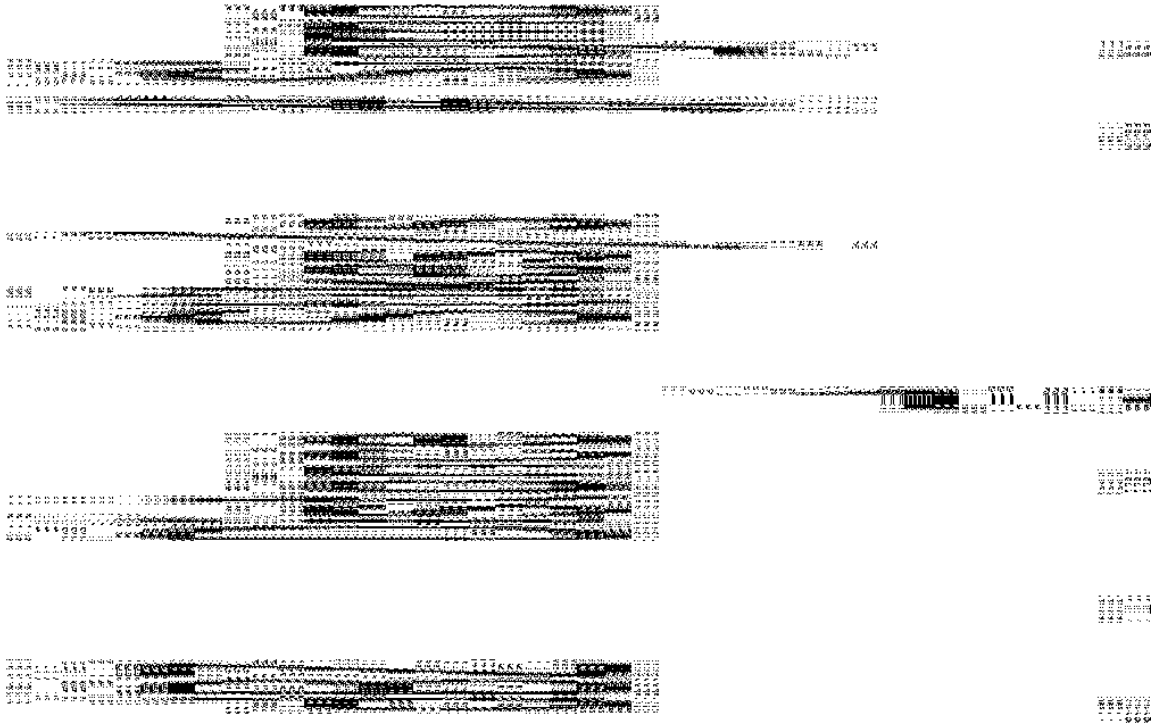
Figure 4.3 TETRA Report for 8/18/2011 events. Panel A (top): Triggers detected on 8/18/2011 (NaI signals above 50 keV in a single detector box with count rate per 2 msec in excess of 20 σ above the 8/18/2011 daily mean counting rate). Box 1 triggers are indicated by plus signs, Box 3 by triangles and Box 4 by squares. Panel B: Rate per second of USPLN lightning strikes within 5 miles. Panel C: Distance to each recorded lightning strike within 100 miles. Panel D: Overhead cloud density.

From July 2010 through February 2013, TETRA recorded a total of twenty-four events with triggers occurring within several minutes of thunderstorm activity producing at least one lightning flash within 5 miles of the detectors. Such events are classified as Event Candidates (ECs) and are listed in Table 4.1. In this table each event trigger time is listed, along with the number of lightning flashes detected within ±2.5 minutes and 5 miles and the cloud density above TETRA. Also listed for each EC is the time difference to the

16

lightning stroke closest in time to the event trigger, the distance to that lightning stroke, the current, the number of gamma rays detected in the EC, and the T_{90} duration of the event (i.e., the time over which a burst emits from 5% to 95% of its total measured counts in a single detector box). The number of sigma above the mean is listed in the second to last column for each event. (For the first three events in the table, observed simultaneously in multiple detector boxes, the smallest number of sigma above the mean is listed. These coincident events, labeled Coincident Event Candidates -- CECs -- are discussed in more detail below.)

TETRA's events, with an average of 20 ± 2 photons detected, are significantly smaller than the typical events observed in space. For TETRA's events, the T_{90} duration was calculated by considering all events detected within a ± 3 msec window around the trigger time, discarding the first and last 5% of timestamps for each event, and recording the time difference between the first and last events remaining. The uncertainty in the T_{90} determination is approximately ± 200 μsec based on a simple Monte Carlo simulation of the data.

In each of the 24 events, 7 to 45 γ-rays were detected within a time window of less than 5 msec, with the total energy deposited per event ranging from 2 to 32 MeV. The distances to the nearest lightning flashes were 0.4 - 2.9 miles. For 14 events, absolute timing was available with ~2 msec accuracy. For each of these 14 events, lightning was observed within 7 seconds of the trigger time. Nine of these events were associated with negative polarity cloud-to-ground (-CG) lightning detected within 6 msec of the trigger. Another 10 ECs were detected during June - July 2012 during a period when accurate trigger-lightning time differences were not recorded due to network timing difficulties. Eight of the ECs during that period were correlated with two intense thunderstorms that passed directly over TETRA on 6/6/2012.

The accidental rate of triggers coincident within 7 sec of a lightning flash that is less than 5 miles distant (i.e., events masquerading as ECs) is calculated based on the rate of TETRA triggers (due mainly to cosmic ray showers), the live time, and the duration of storm activity. The storm activity time is taken to be the sum of all time windows where there was lightning within 5 miles and 7 seconds and there was no electronic noise or other instrumental problems. For a total storm time of 12.65 hrs, we calculate the expected number of ECs due to accidental triggers to be 0.82. This assumes 100% lightning detection efficiency. The USPLN is part of the National Lightning Detection Network (NLDN), which has an efficiency above 99% in our area for cloud-to-ground lightning. However, the efficiency of the USPLN for total (IC + CG) lightning in our area has not been tested. If we assume a similar sensitivity to that measured by Jacques et al. (2011) (for cloud-to-ground lightning with peak current in excess of 20 kA) of approximately 25% to account for undetected lightning flashes, then we would expect 3.3 accidental ECs compared to the 14 observed.

The expected number of CECs due to random triggers is small: Given an initial EC with counting rate in one box in excess of 20 σ above the daily average, the likelihood that a second or third trigger occurred at random in another box within the timing uncertainty of

Table 4.1 Properties of the 24 Event Candidates.

Date	Trigger Time (CST) (hh:mm:ss)	Max Lightning Rate within 5mi. (sec^{-1})	Cloud Density (dBZ)	# Flashes within 5mi. and 5min.	Trigger-Lightning Difference (ms)	Lightning Distance (mi)	Lightning Current (kA)	T_{90} Event Duration (μs)	Total γ Rays Detected	Total Energy (MeV)	σ Above Mean	Probability of CEC
31 Jul 2011	16:21:44.976	2	45	12	-6	1.4	-43.6	702	22	14.7	25.5	1.7E-06
31 Jul 2011	16:21:45.300	2	45	12	-4	1.8	-29.1	1326	24	11.7	25.5	1.7E-06
18 Aug 2011	17:57:38.984	4	50	40	6743	1.3	-23.4	1318	40	20.3	22.5	1.2E-13
24 Feb 2011	23:11:15.787	3	45	1	-6	2.9	-20.9	953	20	1.7	24.6	-
29 Jul 2011	10:38:58.932	6	45	42	5	0.4	-57.7	153	8	4.8	22.6	-
18 Aug 2011	17:57:39.202	4	50	40	6525	1.3	-23.4	24	7	3.6	26.1	-
12 Mar 2012	11:30:16.500	6	45	4	5	1.6	-81.3	1997	7	3.2	21.8	-
2 Apr 2012	12:29:30.554	3	50	8	6	0.6	-29.9	464	30	31.6	104.3	-
4 Apr 2012	02:49:21.900	5	55	21	-3	1.9	-158.4	515	24	21.3	88.6	-
5 Aug 2012	14:43:35.661	7	40	16	-849	0.6	-56.5	392	18	12.4	40.6	-
6 Aug 2012	19:17:33.359	5	50	1	1017	0.8	-23.1	465	13	4.5	21.9	-
9 Aug 2012	15:27:29.804	4	50	21	2	0.4	-27.8	2412	12	2.9	29.0	-
9 Aug 2012	15:28:36.070	4	50	27	80	0.9	-36.7	4217	24	7.4	41.3	-
9 Aug 2012	15:28:36.560	4	50	27	2	0.8	-19.2	146	12	8.0	33.9	-

CECs are listed in the top section; ECs for which the absolute timing uncertainty is known are listed in the middle section; and ECs for which the absolute timing uncertainty is unknown are listed on the next page. The date and time of each EC trigger are listed (Columns 1 and 2), along with the properties of the storm associated with each event (Columns 3-5). The properties of the associated lightning (Columns 6-8), event duration (Column 9), number of gamma rays detected (Column 10), total energy (Column 11) and event significance (Column 12) are also listed for each event. The probability of each CEC occurring is listed in the last column (Column 12) for the CECs. Refer to text for details.

(Table 4.1 Continued)

Date	Trigger Time (CST) (hh:mm:ss)	Max Lightning Rate within 5mi. (sec^{-1})	Cloud Density (dBZ)	# Flashes within 5mi. and 5min.	Trigger-Lightning Difference (ms)	Lightning Distance (mi)	Lightning Current (kA)	T_{90} Event Duration (μs)	Total γ Rays Detected	Total Energy (MeV)	σ Above Mean	Probability of CEC
6 Jun 2012	15:37:31	6	55	40	-	-	-	865	45	27.2	86.1	-
6 Jun 2012	15:44:18	6	55	16	-	-	-	609	14	8.5	45.7	-
6 Jun 2012	19:23:27	6	55	40	-	-	-	2979	18	6.7	45.7	-
6 Jun 2012	19:29:43	6	55	33	-	-	-	2376	24	9.7	55.3	-
6 Jun 2012	19:31:21	6	55	19	-	-	-	919	40	29.8	48.3	-
6 Jun 2012	19:32:41	6	55	19	-	-	-	827	9	5.4	21.0	-
6 Jun 2012	19:36:40	6	55	18	-	-	-	2035	8	5.2	20.1	-
6 Jun 2012	19:36:41	6	55	18	-	-	-	631	32	31.4	63.1	-
9 Jun 2012	13:40:16	6	50	1	-	-	-	1930	15.0	8.6	55.1	-
7 Jul 2012	17:38:45	5	45	1	-	-	-	510	14.0	8.0	33.9	-

CECs are listed in the top section of the previous page; ECs for which the absolute timing uncertainty is known are listed in the middle section of the previous page; and ECs for which the absolute timing uncertainty is unknown are listed on the current page. The date and time of each EC trigger are listed (Columns 1 and 2), along with the properties of the storm associated with each event (Columns 3-5). The properties of the associated lightning (Columns 6-8), event duration (Column 9), number of gamma rays detected (Column 10), total energy (Column 11) and event significance (Column 12) are also listed for each event. The probability of each CEC occurring is listed in the last column (Column 12) for the CECs. Refer to text for details.

2 msec on the same day is estimated as (4 msec × N/86400 sec)$^{b-1}$, where N is the total number of random 20 σ triggers detected per day through February 2013 and b is the number of boxes triggered in the event. (For simplicity, we neglect here the increase in trigger rate during a thunderstorm shown in Fig. 4.1.) Multiplying by the number of ECs then gives the expected number of spurious CECs involving two boxes occurring by chance as 1.7 x 10-6, as listed in Table 4.1.

Figure 4.4 compares data acquired within 7 seconds of lightning to the remaining data with accurate timing information. The distribution of events vs σ within 7 seconds of a USPLN lightning strike within 5 miles is shown in black. The significance distribution of the remaining data has been normalized to the total storm activity time of the lightning distribution for comparison, shown in grey. The excess of events above 20 sigma in the lightning distribution (black) as compared to the normalized distribution (grey) indicates the association of the gamma ray events with nearby lightning. (Note that, since three events involve seven separate coincident triggers in individual detector boxes, there are 18 individual triggers shown in Fig. 4.4 compared to the 14 ECs with accurate timing information in Table 4.1.) A Kolmogorov-Smirnov test of the two distributions results in
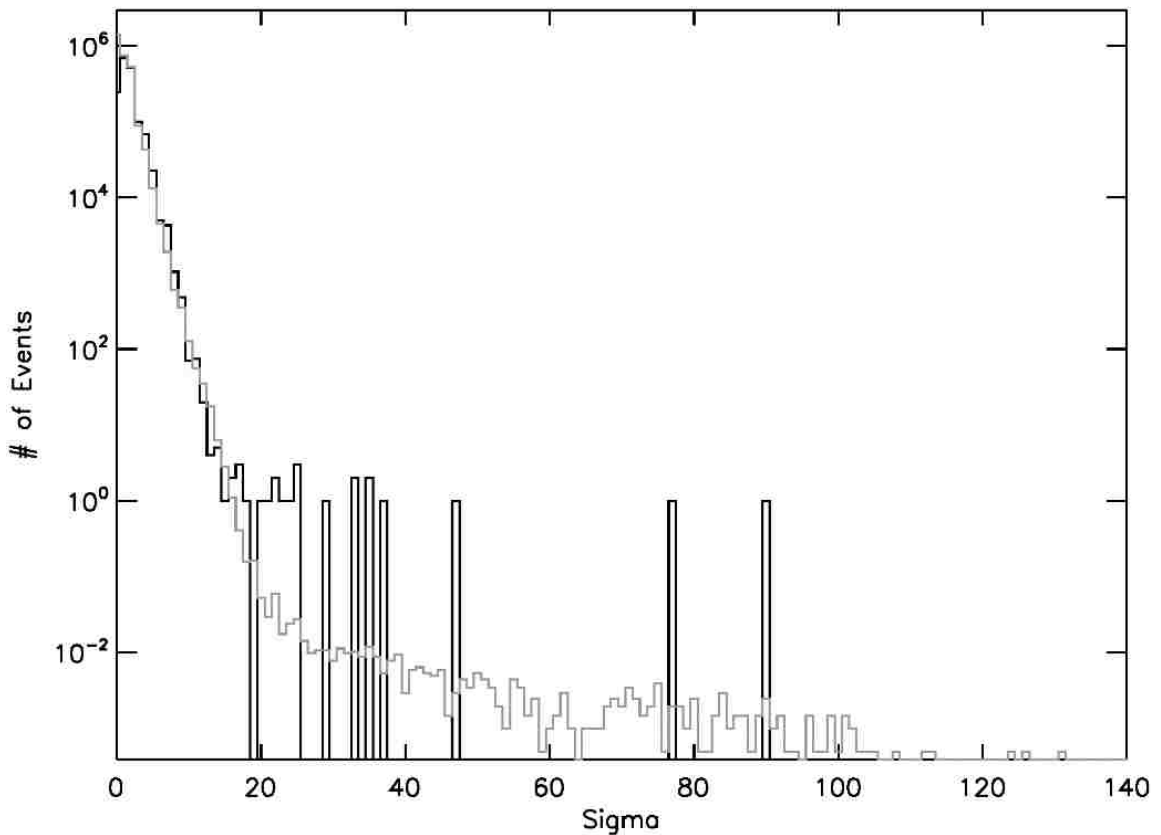
Figure 4.4 Distribution of events with significance σ. Distribution of events within 7 seconds of nearby (< 5 miles) lightning is shown in black. Distribution of all data, normalized to 0.52 days of live time, is shown in grey, showing excess of lightning-associated ECs at σ > 20.

a D parameter of 0.25, corresponding to high confidence that the two distributions are distinct.

The dark solid histogram in Fig. 4.5 shows the deposited energy spectrum of the 24 Event Candidates, with events observed up to 2.7 MeV deposited energy. It should be emphasized that, with TETRA's thin detectors, only a portion of the incident gamma ray energy is actually detected. Between 200 keV and 1.2 MeV, the EC spectrum is fit with a power law $E^{-\alpha}$, with $\alpha = 0.92 \pm 0.19$ and χ^2/degree of freedom = 0.9 (dark dashed line). On the same figure, the grey line shows the spectrum of non-EC triggers (i.e., triggers not associated with lightning within 5 miles and 7 seconds); this spectrum is softer, with a best fit power law index $\alpha = 1.46 \pm 0.05$ and χ^2/degree of freedom = 1.5 (grey dashed line). The EC spectrum below shows no evidence of the predicted positron-electron annihilation line at 511 keV. This may be due to a lack of statistics, the resolution of the detectors, or the atmospheric attenuation between the event and the array. As before, the associations of the events reported here with negative polarity lightning strikes and the low likelihood that these are background events, along with the durations observed, are indicative of downward directed TGFs produced by the RREA mechanism.
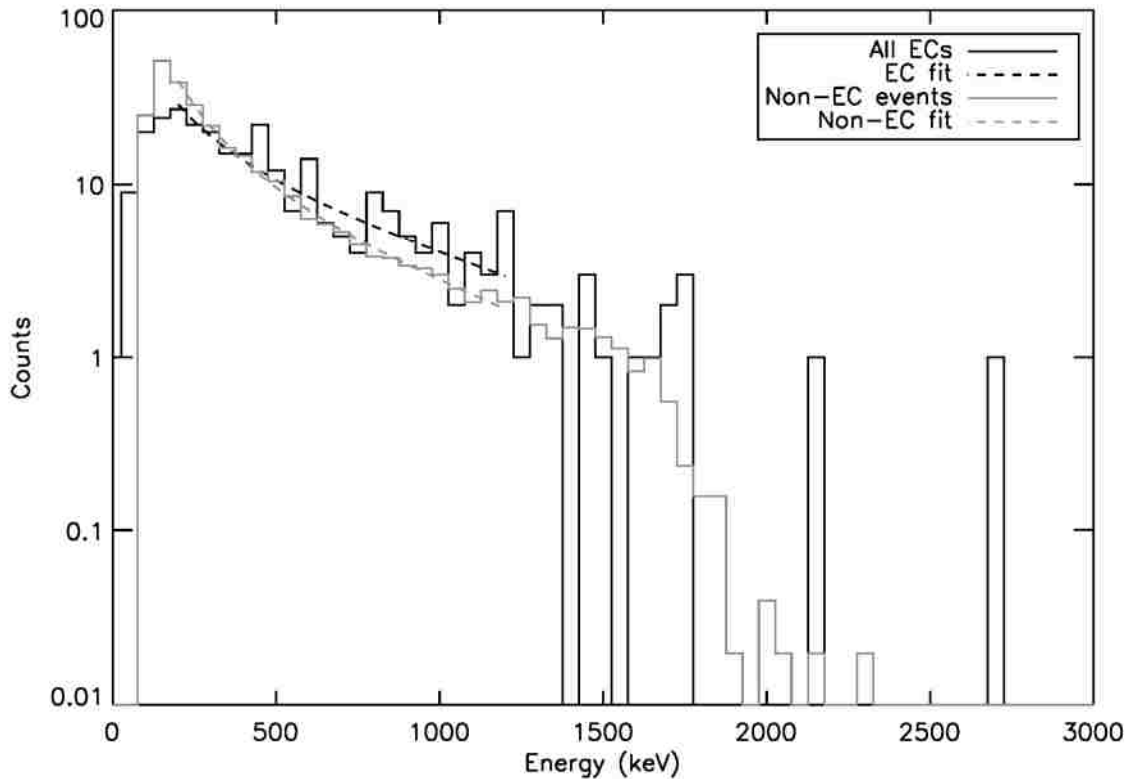
Figure 4.5 Spectra of Event Candidates and non-EC TETRA triggers. Spectrum of ECs is shown in black. Spectrum of non-EC TETRA triggers (triggers not associated with lightning nearby in time and distance) is shown in grey. Power law fits between 200 keV and 1200 keV of the form $E^{-\alpha}$ are shown with dotted lines, where $\alpha = 0.92 \pm 0.19$ and 1.46 ± 0.05 for EC and non-EC events respectively.

In three of the 24 ECs, triggers were recorded in two or more boxes separated by ~1000 m within less than ±2 msec. This is approximately the relative timing accuracy between separate boxes. All three of these Coincident Event Candidates (CECs) occurred in July and August of 2011, when storms in southern Louisiana tend to be associated with disturbances in the Gulf of Mexico rather than frontal lines. No CECs were detected when there was no lightning activity within 5 miles.

Time histories for the three CECs are shown in Fig. 4.6. The plot shows a 50 msec window centered on the event trigger time, defined as the center of the first 2 msec bin containing a trigger. The counts for each box (i.e., the number of phototubes detecting a signal with amplitude in excess of 50 keV within the 1 microsecond PMT anode output integration time) are plotted vs time relative to the event trigger time. For the two events on 7/31/2011 (panels A and B), the lightning strikes closest in time occurred within
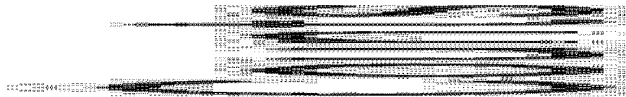
Figure 4.6 NaI time histories over 50 msec window centered on the trigger time for each CEC. Lightning strikes within 5 miles in the 50 msec window have a ±2 msec timing uncertainty and are shown with X's in panels A and B. No lightning was detected within 5 miles in the 50 msec window for the event shown in Panel C. Panel A: CEC on 7/31/2011 at 16:21:44.976 CST. The Box 3 time history is centered at 0 msec and Box 4 at 2 msec. Panel B: CEC on 7/31/2011 at 16:21:45.300 CST. The Box 3 time history is centered at 0 msec and Box 4 at 2 msec. Panel C: CEC event on 8/18/2011 at 17:57:38.984 CST with the Box 3 time history centered at 0 msec, Box 1 at 2 msec and Box 4 at 4 msec. Refer to text for details.

approximately 6 and 4 msec of the event trigger. For those cases, the time of the lightning strike is shown as an X with a timing uncertainty of ±2 msec near the top of the plot. In the first 7/31/2011 event (Panel A of Fig. 4.6), one PMT in box #3 fired, followed by two PMTs in box #4 2.3 msec later. The distance between the two boxes was 1500 m, corresponding to a gamma ray travel time difference of up to 5 μsec. In fact, we infer the differences between the event times in the separate boxes in Fig. 4.6 are a direct measure of the absolute timing differences between the boxes.

A composite energy spectrum summed over the 3 CECs is shown in Fig. 4.7. A total of 80 gamma ray pulse heights above 50 keV and within the T_{90} interval of each coincidence trigger are shown. The average photon energy detected is approximately 0.5 MeV, an energy at which the fraction that passes through a nominal 1 mile of atmosphere at ground level (STP) without interaction is $\sim 10^{-7}$. This average energy is low compared to the typical energies observed by the orbiting detectors (Dwyer et al., 2012b) and is presumably biased to low energies by the 0.5 cm thickness of the TETRA NaI scintillators.

Figure 4.7 CEC Event Spectra. Combined NaI detector energy spectrum for the three CECs. 80 photons were detected within the T_{90} interval of each individual detector box's trigger time.

Figure 4.8 shows the distance from the detectors and the measured current for each lightning flash within 5 miles of TETRA from 7/1/2010 to 2/28/2013 as reported by the

USPLN. There were a total of 5360 flashes within 5 miles. For each of the 10 ECs and CECs with lightning within 5 miles and ±100 msec of the trigger time, the distance and measured current are plotted with black X's. Although all the TETRA events correspond to lightning less than 3 miles away, the two lightning flashes within ±100 msec of a CEC are both more than a mile away. No CECs were detected with closer lightning strikes. If all discharges produce TGFs (Østgaard et al., 2012), then the rate of detection and the CEC distances point to either a range of intensities extending below the sensitivity limit of TETRA, strongly beamed emission, or the possibility that the gamma ray emission is only indirectly associated with the lightning (Connaughton et al., 2013). This can also occur if some gamma ray events are produced by intracloud (IC) strikes, since the USPLN data record primarily cloud-to-ground strikes.
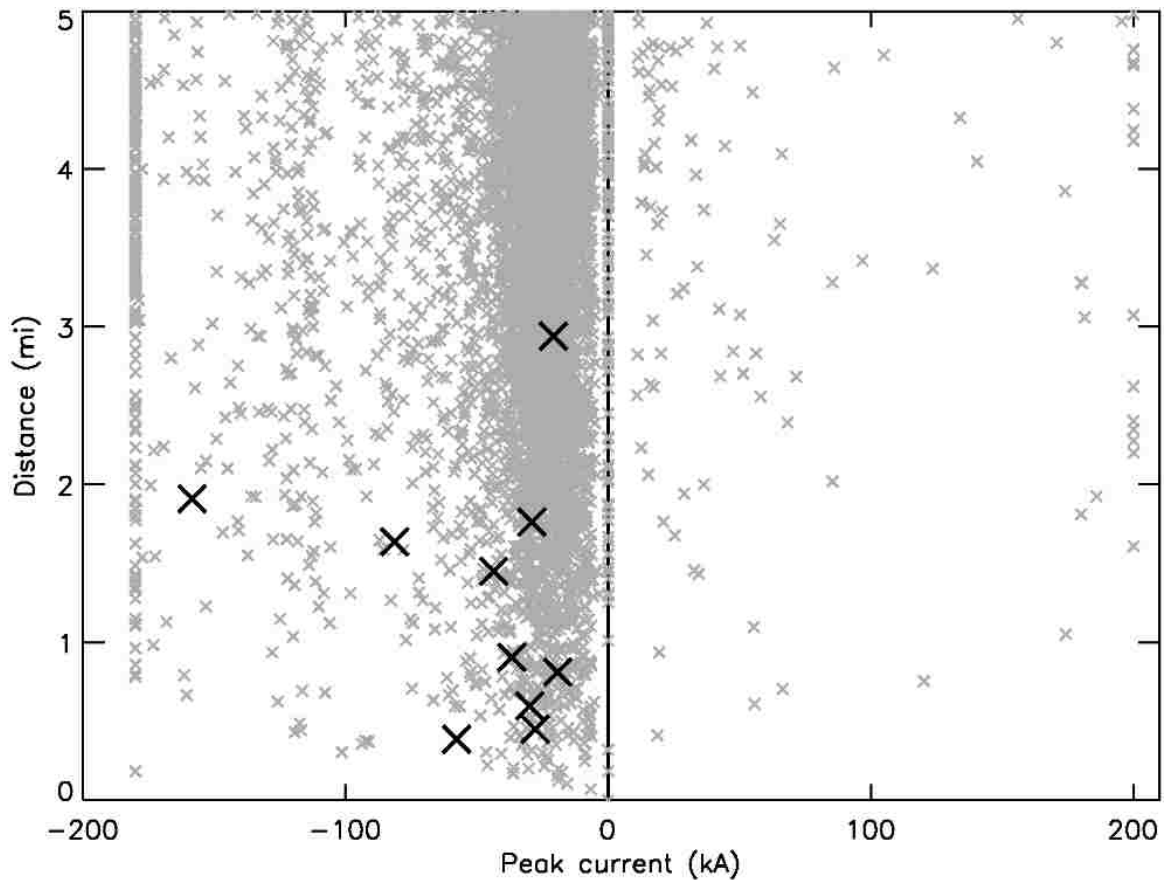
Figure 4.8 All Lightning Activity within 5 miles of TETRA from 7/1/2010 to 2/28/2013. The current and distance for all USPLN lightning flashes within 5 miles of TETRA are indicated by grey X's. Lightning strikes that are within 5 miles and 100 msec of an EC or CEC are considered coincident strikes and are plotted with black X's. The vertical line at 0 kA indicates IC lightning.

Out of the 10 ECs shown in Fig. 4.8, nine were found to be within 6 msec of a negative polarity CG lightning strike within 3 miles with current above 20 kA (Table 4.1). For the two CECs that occurred on 7/31/2011, lightning strikes are recorded at 6 msec and 4 msec before the TETRA triggers. In both cases, these were nearby, cloud-to-ground

events at 1.4 miles distance with current -43.6 kA and 1.8 miles distance with current -29.1 kA. For four ECs with accurate timing information, the lightning strikes closest in time to the TETRA triggers were in excess of ±100 msec before or after the NaI signal and so are not considered coincident with a USPLN observed strike. Again, this can occur if some gamma ray events are produced by intracloud (IC) strikes or if the gamma rays are not all directly associated with the lightning.

CHAPTER 5 – UPDATED TETRA DATA ANALYSIS AND RESULTS: JULY 2010 TO MARCH 2014

Accurate trigger-lightning time differences were not recorded during June - July 2012 due to network timing difficulties, resulting in timing errors of several minutes. During this period, event times were generated by alternating between an onboard system clock and network timing. In a secondary analysis, it was found that the data acquisition software (DAQ, v6.5) produced groups of erroneous timestamps while these difficulties were experienced. One such group is shown in Fig. 5.1. The top panel plots the time in microseconds originally assigned to each individual count with increasing index number (event number). Normally, this type of plot shows an approximately linear increase of time with index number. In this case, a large 'dip' is evident, indicating that erroneous timestamps were used. These dips indicate clock offsets tens of milliseconds below the projected time.
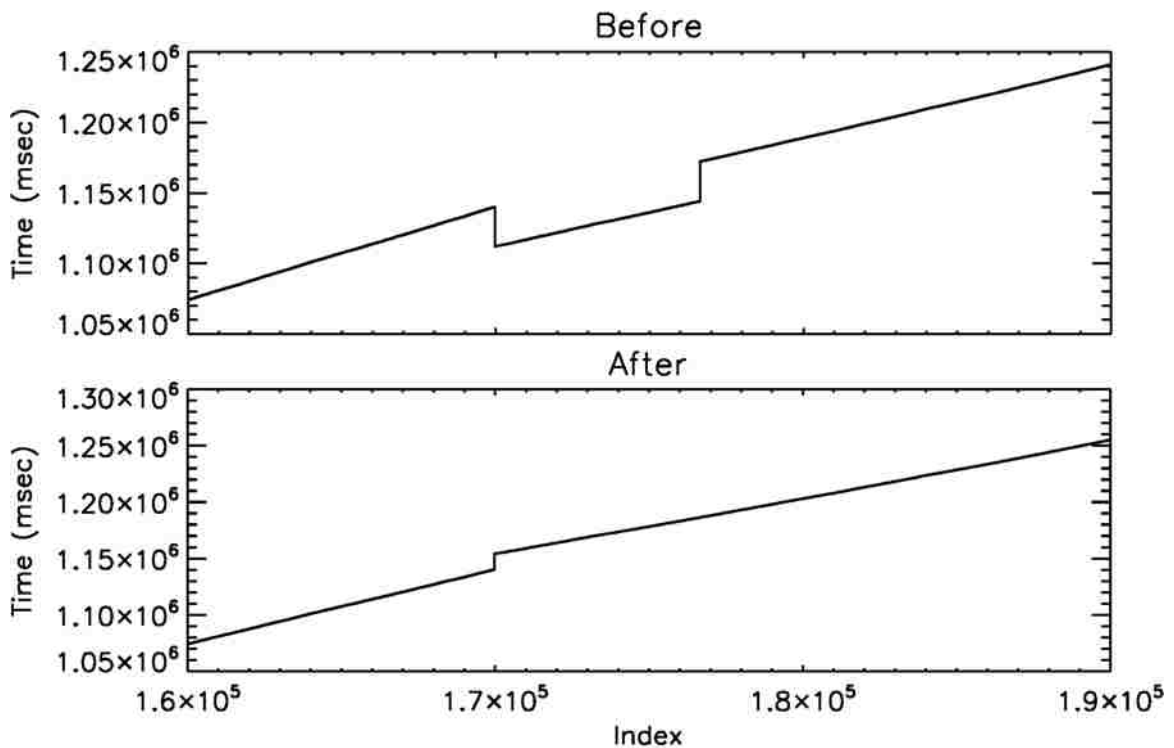
Figure 5.1 Time assigned to a group of counts by DAQ v6.5 during June - July 2012. Top Panel: Original time in msec assigned to counts with increasing index number. Bottom Panel: Corrected time in msec for the same counts.

Instead of discarding these groups, software was written to correct for the offset. The maximum time offset on either side of the dip was added to each timestamp within the dip. The bottom panel of Fig. 5.1 shows the corrected time for the same counts. The small step in the bottom panel of Fig. 5.1 is a result of the differing time offsets on either side of the dip. After the count times were corrected for the event candidates (ECs) affected

by this error, four ECs were no longer within ±7 seconds of lightning within 5 miles of TETRA, specifically the events on June 9, 2012, July 7, 2012 and two events on June 6, 2012 at 19-32-41 and 19-36-40 (hh-mm-ss). Since the trigger-lightning time was no longer within the defined limit, these ECs were removed from the list. This clock monitoring and correction software is included in the analysis of the 2013 and future events.

One more EC was removed from the list due to noise on one detector during the event, specifically the EC on June 6, 2012 at 19:23:27.057. The individual detector count rates for each event are shown in Fig. 5.2. For this case, two NaI photomultiplier tubes (PMTs) in each box were operating on that day, but no counts on the second PMT were recorded within ±3 milliseconds of the trigger time. It was also found that several false triggers exhibited similar behavior. As a result, this and future ECs found to exhibit noise on one detector during the event are classified as false triggers. An updated version of Table 4.1 is presented in Table 5.1.
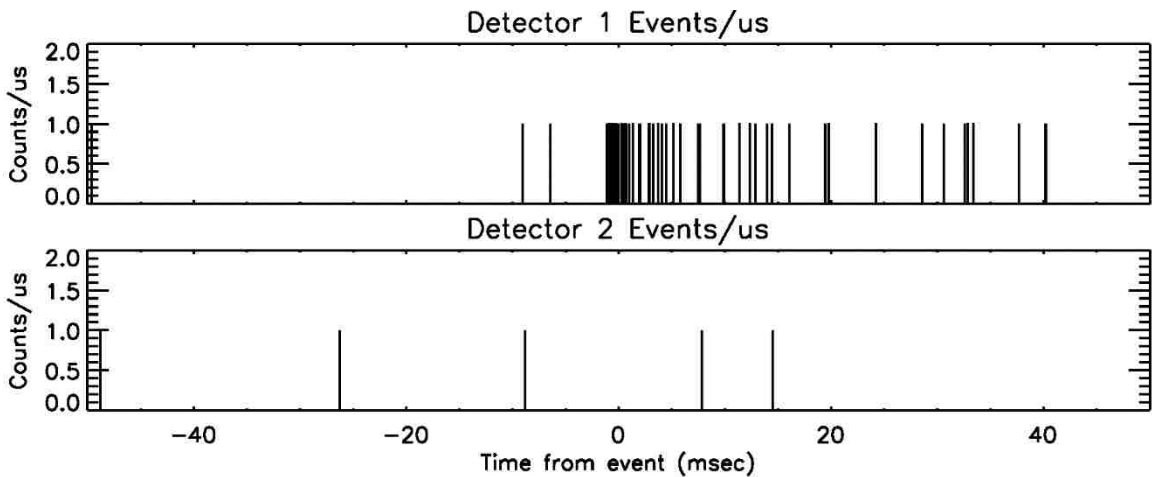
Figure 5.2 NaI time histories over ±50 msec window centered on the trigger time for noise EC detected on June 6, 2012 at 19:23:27.057. Top Panel: Detector 1 count rate. Bottom Panel: Detector 2 count rate.

Table 5.1 also includes the timing uncertainty for each event. The timing uncertainty is calculated by finding the Gaussian standard deviation of the offsets of each time correction listed on the day an EC is detected. The software used for this calculation is described in Appendix C and located at http://heastro.phys.lsu.edu/lsutgfcode. For DAQ v6.5, the time correction is performed up to 600 times per 24-hour period from October 2010 to October 2012. The magnitudes of these corrections are from 0.5 to 5 milliseconds. The GPS timing software included in DAQ v8.1 performs this time correction every second with correction magnitudes less than 60 nanoseconds from October 2012 to March 2014. Consequently, the timing uncertainties associated with the 2013 events are less than 60 nanoseconds while the timing uncertainties of earlier events are 0.5 to 5 milliseconds. Two ECs were detected with DAQ v8.01 (a test version of v8.1) with GPS timing (accurate to within ±200 nsec) on Aug 5 and 6, 2012, but the exact timing uncertainty is unknown.

27

Table 5.1 Properties of the 28 Event Candidates.

CECs are listed in the top section; ECs for which the absolute timing uncertainty is known are listed in the second section; and ECs for which the absolute timing uncertainty is unknown are listed in the third section of the table (from previous chapter). Events detected during the 2013 season are listed on the next page. The date and time of each EC trigger are listed (Columns 1 and 2), along with the properties of the storm associated with each event (Columns 3-5). The properties of the associated lightning (Columns 6-8), event duration (Column 9), number of gamma rays detected (Column 10), total energy (Column 11) and event significance (Column 12) are also listed for each event. Refer to text for details.

(Table 5.1 Continued)

Date	Trigger Time (CST) (hh:mm:ss)	Timing Error (µs)	Max Lightning Rate within 5mi. (sec⁻¹)	Cloud Density (dBZ)	Storm Type	# Flashes within 5mi. and 5min.	Trigger-Lightning Difference (ms)	Lightning Distance (mi)	Lightning Current (kA)	T_{90} Event Duration (µs)	Total γ Rays Detected	Total Energy (MeV)	σ Above Mean
14 Apr 2013	01:26:02.390	0.037	4	45	Coastal	2	-493	0.7	-46.9	1552	9	3.9	51.4
24 Apr 2013	07:11:37.894	0.024	5	50	Front	24	6595	1.9	-64.8	616	7	1.6	25.6
10 May 2013	03:51:57.412	0.034	5	55	Front	166	969	1.3	-23.9	1032	29	-	101.3
10 May 2013	03:51:58.116	0.047	5	55	Front	163	265	1.3	-23.9	80	6	2.1	25.2
22 Jun 2013	14:31:28.794	0.058	5	50	Coastal	7	-292	1.7	-33.8	159	8	1.9	25.8
22 Jun 2013	14:52:49.063	0.043	5	50	Coastal	6	199	1.3	-48.9	1757	15	5.6	50.4
29 Jun 2013	04:24:11.550	0.038	4	40	Front	17	-169	1.7	-32.9	732	14	7.0	89.7
29 Jun 2013	04:24:11.614	0.038	4	40	Front	17	-233	1.7	-32.9	164	4	3.0	31.6
13 Sep 2013	18:11:13.263	0.019	5	50	Coastal	39	403	1.4	-35.3	1539	18	6.2	40.9

CECs are listed in the top section on the previous page; ECs for which the absolute timing uncertainty is known are listed in the second section on the previous page; and ECs for which the absolute timing uncertainty is unknown are listed in the third section of the table on the previous page (from Table 4.1). Events detected during the 2013 season are listed on the current page. The date and time of each EC trigger are listed (Columns 1 and 2), along with the properties of the storm associated with each event (Columns 3-5). The properties of the associated lightning (Columns 6-8), event duration (Column 9), number of gamma rays detected (Column 10), total energy (Column 11) and event significance (Column 12) are also listed for each event. Refer to text for details.

In Table 5.1, the reader may notice that the γ-rays detected, total energy and σ above mean entries have changed for some of the ECs. When the data were reanalyzed with the time correction software, the times of some of the counts were moved away from the event, causing a general decrease in the significance of the 2 msec time bin. No ECs were removed by this effect. An upper cutoff energy corresponding to each detector's saturation energy was also included to ignore the higher energy photons -- presumably cosmic rays -- present in the events. This cutoff was applied after the event duration was calculated and before the energy and number of γ rays were totaled. This caused a decrease in the number of γ rays detected and in the total energy observed for several of the events.

Table 5.1 also includes the event candidates detected by TETRA during March 2013 - March 2014 using the code located at http://heastro.phys.lsu.edu/lsutgfcode. This code is the same software used to analyze the data presented in chapter 4, but with the corrections described above. During this period, TETRA recorded nine events occurring within ±7 seconds of lightning within 5 miles of the array. These events are listed on the second page of Table 5.1. No events were detected later than October of 2013. As in chapter 4, this table lists the properties of each event, including the timing errors described above. No CECs were detected in the 2013 season.

The properties of the nine events detected in 2013 are similar to previously reported events with the exception of lightning associations. Nine of the 13 previously reported events were associated with lightning. However, none of the 2013 events were linked to lightning within 100 milliseconds of the event time and 5 miles (8 km) of TETRA. This confirms that some gamma ray events observed from the ground are not directly associated with lightning or are produced by intracloud (IC) strikes which are not easily detected by USPLN [Strader et al., 2013].

As mentioned in chapter 3, a blank PMT (sealed photomultiplier tube without a scintillator) was included in each box beginning in October of 2012. Figure 5.3 shows the count rate of each detector channel during the event on 13 Sep 2013. Panel A shows the total count rate per μsec, Panels B and C show the count rates for the two NaI scintillators, Panel D for the LaBr$_3$ scintillator and Panel E for the blank PMT. No counts were observed on the blank PMTs during these events, confirming that the events were not due to electronic noise.

As described in chapter 4, the accidental rate of triggers coincident within 7 sec of a lightning flash that is less than 5 miles distant (i.e., events masquerading as ECs) is recalculated based on the rate of TETRA triggers (due mainly to cosmic ray showers), the live time, and the duration of storm activity. 2091 TETRA triggers were detected during 909.16 days of live time (21.09 storm hours) since July 1, 2010, resulting in 2.02 expected false ECs compared to the 28 total ECs observed. If a total (IC + CG) lightning detection efficiency of 25% is assumed, then we would expect 8.08 accidental ECs. The five false ECs already removed from this list are described above.

Figure 5.4 is an updated version of Fig. 4.4, replotted to include the 2013 events and remove false events discovered in the reanalysis. As before, ECs without timing are not included in this figure and the three CECs account for seven ECs. A Kolmogorov-Smirnov test of the two distributions results in a D parameter of 0.867, higher than the previously reported value of 0.25. This distinguishes the ECs from the background distribution with higher confidence.
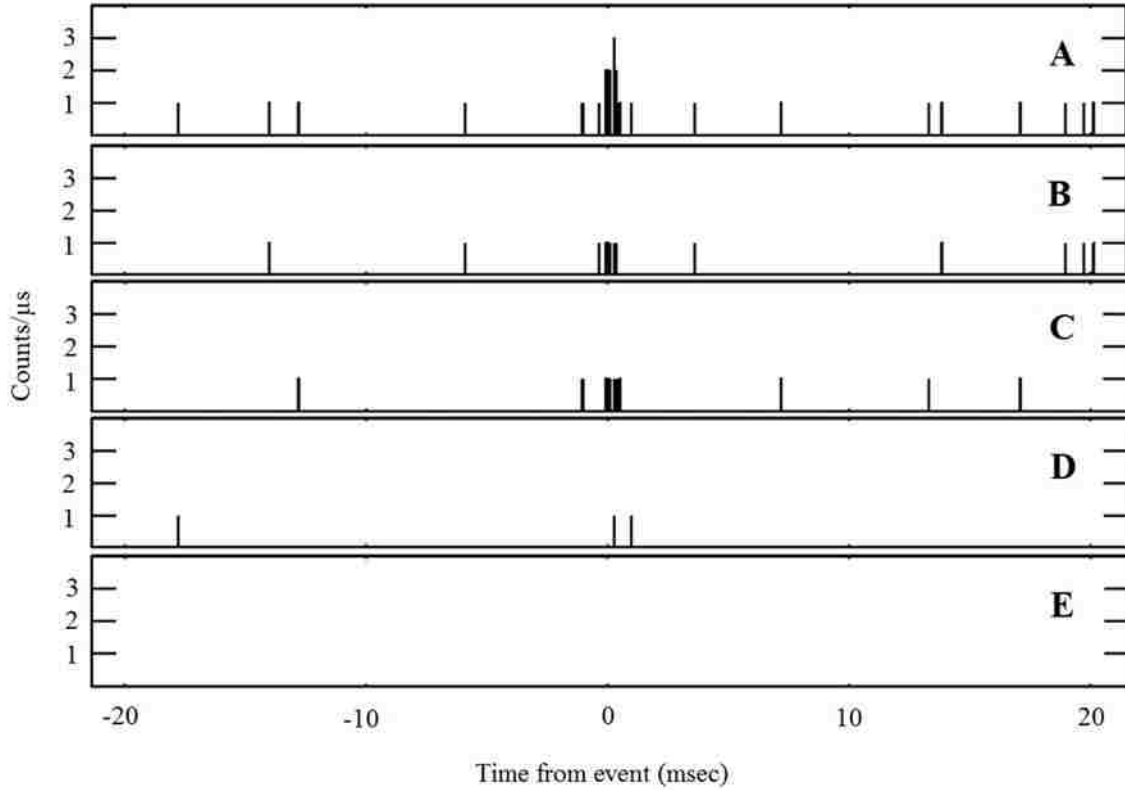
Figure 5.3 Detector count rates during event on 13 Sept 2013. Time from the event time is plotted in milliseconds. Panel A: Total count rate per μsec for all detector channels. Panels B and C: Individual count rates for the NaI scintillators. Panel D: Count rate for the LaBr₃ scintillator. Panel E: Count rate for the blank PMT.

The energy spectrum of the event candidates is recalculated to include the 2013 events (Fig. 5.5, an updated version of Fig. 4.5). Between 200 keV and 1.2 MeV, the EC spectrum is fit with a power law $E^{-\alpha}$, with $\alpha = 0.90 \pm 0.14$ and χ^2/degree of freedom = 0.95 (dark dashed line). On the same figure, the grey line shows the spectrum of non-EC triggers (i.e., triggers not associated with lightning within 5 miles and 7 seconds); this spectrum is significantly softer, with a best fit power law index $\alpha = 1.58 \pm 0.04$ and χ^2/degree of freedom = 2.0 (grey dashed line). These fit parameters are within the uncertainties of those reported in chapter 4, implying that the events detected in 2013 have similar energy spectra as earlier events.

31

The events presented here were detected with TETRA from July 2010 to March 2014 with nine events in 2013. The majority of these events occurred from June to August, when storms in southern Louisiana tend to be associated with disturbances in the Gulf of Mexico rather than frontal lines. However, almost half of the events in Table 5.1 were associated with fronts, hinting that the source of the storm associated with the TGF may not be as important as the strength and maturity of the storm itself. These and other storm characteristics are analyzed in the next chapter.
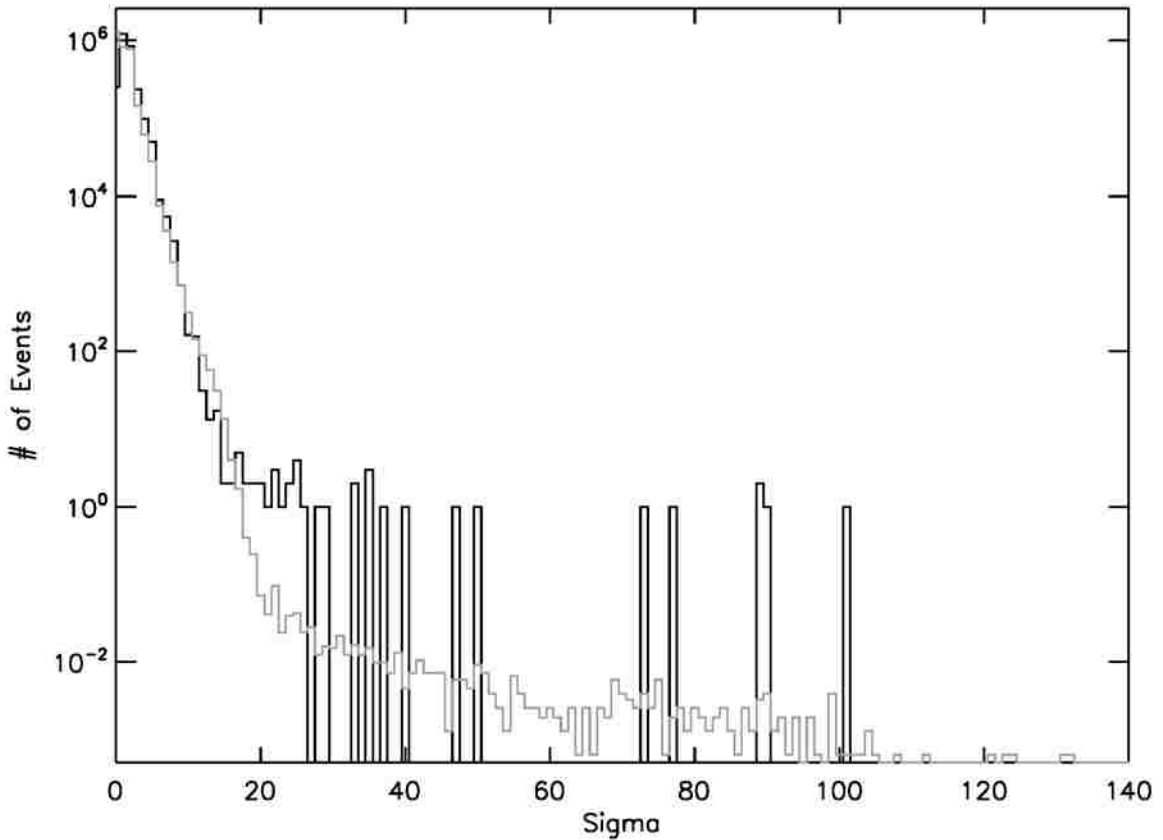
Figure 5.4 Distribution of events with significance σ for July 1, 2010 to October 31, 2013. Distribution of events within 7 seconds of nearby (< 5 miles) lightning is shown in black. Distribution of all data, normalized to 0.88 days of live time, is shown in grey, showing excess of lightning-associated ECs at σ > 20.
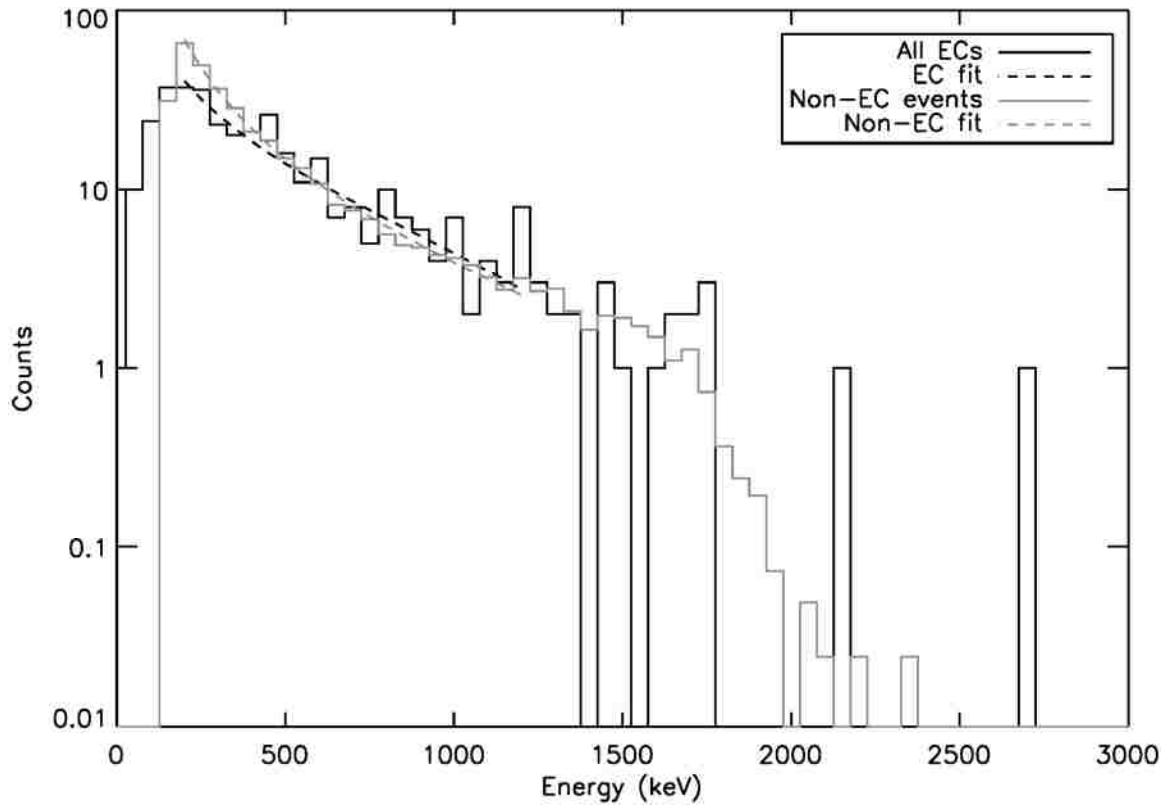
Figure 5.5 Spectra of Event Candidates and non-EC TETRA triggers from July 1, 2010 to October 31, 2013. Spectrum of ECs is shown in black. Spectrum of non-EC TETRA triggers (triggers not associated with lightning nearby in time and distance) is shown in grey. Power law fits between 200 keV and 1200 keV of the form $E^{-\alpha}$ are shown with dotted lines, where $\alpha = 0.90 \pm 0.14$ and 1.58 ± 0.04 for EC and non-EC events respectively.

CHAPTER 6 – TETRA STORM ANALYSIS

Since their discovery, TGFs have been known to be associated with thunderstorms [Fishman et al., 1994]. A substantial percent of TGF have been matched with individual lightning strikes detected by ground-based lightning networks [Cummer et al., 2011; Inan et al., 1996; Lu et al., 2011]. Specific studies of TGF-associated lightning have shown that the radio signatures (sferic) produced by TGFs occur in a variety of frequency bands [Connaughton et al., 2012]. In some cases, the altitudes of TGF-sferics have been determined using ionosphere reflections [Shao et al., 2010]. Although efforts have been made to correlate TGF production with storm evolution based on lightning flash rates [Smith et al., 2010], there has been only one study to date on the properties of the storms that produce TGFs [Splitt et al., 2010]. Splitt et al. performed a population study of storms associated with RHESSI TGFs, but was unable to analyze the maturity stage of the storms due to lack of radar information. With TETRA's reliable detection of TGFs from the ground, the detailed characteristics of the associated storms can be analyzed for the first time.

In general, thunderstorms have three main stages of development (Fig. 6.1). In the initial phase, moist, unstable air forms an updraft, leading to the development of towering cumulus clouds as pictured on the left. Hills, mountains, surface heating and colliding air masses provide the lifting mechanism for these updrafts. As the updraft nears the tropopause (boundary between the troposphere and the stratosphere near 15 km), the warm air cools and forms a downdraft of precipitation towards the rear of the storm. A thunderstorm is considered 'mature' when both an updraft and a downdraft are present. In the mature stage, heavy rain, lightning, hail and sometimes tornadoes are produced. In most cases, the precipitation downdraft eventually chokes the updraft and dominates the thunderstorm. Without a strong updraft to feed the thunderstorm, the storm begins to
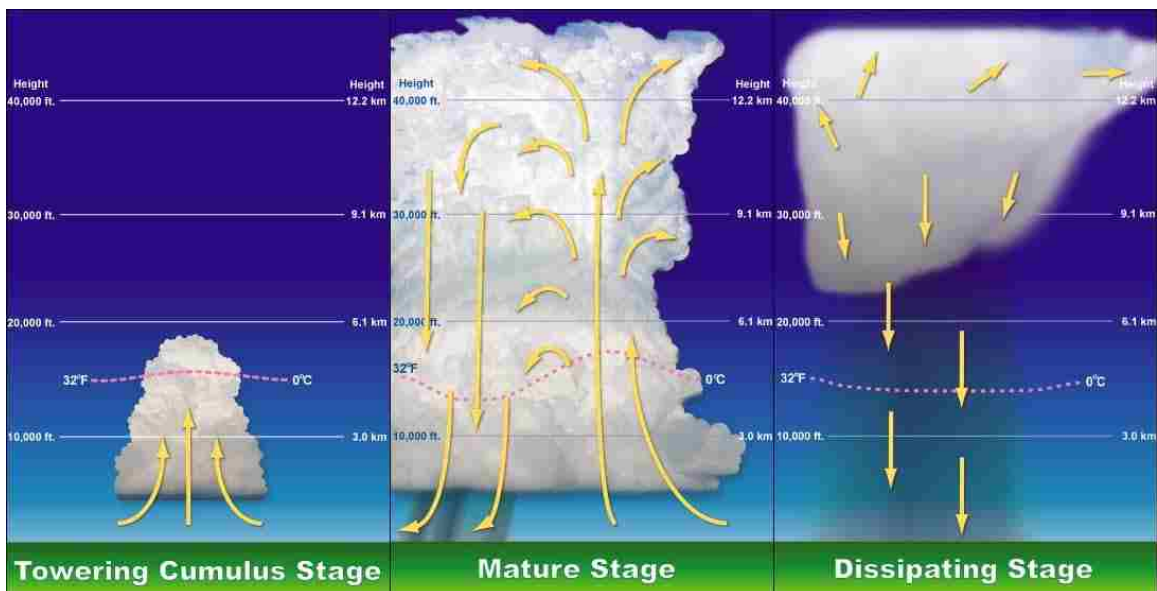

Figure 6.1 Main Thunderstorm Stages. From the National Weather Service.

dissipate, resulting in light precipitation and decreasing cloud cover. In some cases, lightning can still be produced as the storm dissipates.

The thunderstorms associated with TETRA events fall into two categories: single cell thunderstorms and squall lines. Single cell thunderstorms are generally short-lived (a few hours) and only rarely produce severe weather. These storm types are commonly associated with isolated and scattered thunderstorms. In Louisiana, these storms are produced by warm, moist updrafts common to coastal environments and approach from all directions. Squall line thunderstorms form the basis of frontal lines but also occur with some summer storms. In Louisiana, frontal lines usually approach from the west while summer thunderstorms associated with squall lines approach from the northwest, north and northeast. Of the 17 storms producing the 28 events, eight were single cell thunderstorms and nine were squall lines.

Half of the TGFs observed by TETRA were produced by variations of single cell thunderstorms. An example of a single cell thunderstorm at the time of a TETRA TGF is shown in Fig. 6.2. The smoothed radar scan is shown here, produced by the GR2Analyst software (available at http://www.grlevelx.com/gr2analyst_2/) using radar data requested at http://www.ncdc.noaa.gov/nexradinv/. The front of the storm is located near White Castle, LA and is moving SE towards Donaldsonville, LA, as indicated by the white arrow. The colors in the image correspond to the varying densities of the cloud at the

Figure 6.2 Smoothed radar image of the single cell thunderstorm producing the TETRA TGF on 12 Mar 2012. Colors in the image correlate to the density of the cloud in decibels at the lowest elevation angle (0.5°) as indicated in the scale at left. The white arrow indicates the direction of storm movement. The green triangle indicates the location of hail. The red square near the top of the figure is the location of TETRA. Local interstates and highways are shown with red and orange lines near the top of the image. The locations of various cities are also labeled for reference. The image is approximately 90 km by 50 km.

lowest elevation angle (0.5°, see scale in image). As is common for thunderstorms, the main updraft of this storm is located at the front of the storm, shown by the purple and red areas in the southern portion of Fig. 6.2. The downdraft is located behind this area and fans out to the northwest, north and northeast. The green triangle in the southern section of the image indicates the location of hail less than one inch in diameter detected by Next Generation Radar (NEXRAD) algorithms [Stumpf et al., 1997].

A three-dimensional image of this thunderstorm is shown in Fig. 6.3. In this image, the storm is viewed from the east from slightly above the image plane. The smoothed radar image is shown on the bottom layer of the volume. Altitude is indicated by the horizontal grey lines in tens of thousands of feet. As in Fig. 6.2, the arrow indicates the movement of the storm. Iso-density surfaces of 30 dBZ, 40 dBZ and 50 dBZ are shown in green, yellow and red, respectively, to visualize the structure of the thunderstorm cloud. As expected, the updraft shown by the dense clouds (on the left of the image) is also correlated with the tallest clouds of the storm. The trailing downdraft is again located towards the rear of the storm (right side of the image) and is associated with clouds of decreasing altitude as distance from the updraft increases. In general, winter storm clouds have lower maximum altitudes than summer thunderstorms. This storm occurred in the winter season, producing clouds with a maximum altitude of 10.9 km (35.9 kilofeet (kft)) based on the maximum height of the cloud with a reflectivity value of 18.5 dBZ or
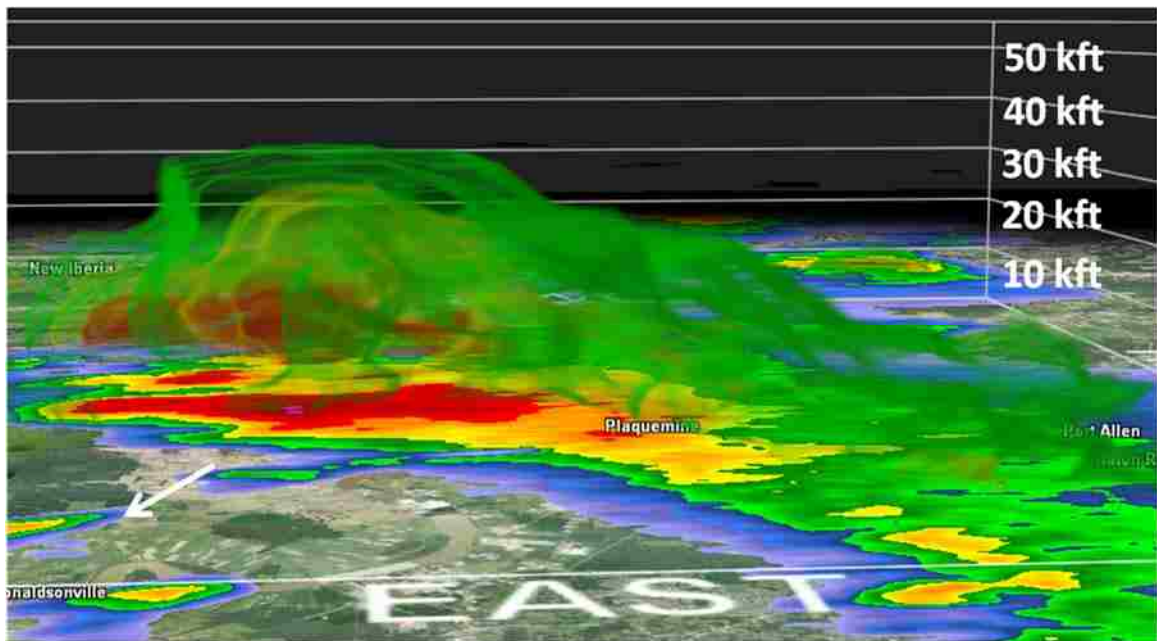
Figure 6.3 Three dimensional radar image of the single cell thunderstorm producing the TETRA TGF on 12 Mar 2012. Altitude is indicated by the grey horizontal lines in tens of thousands of feet. The smoothed radar image in Fig. 6.2 is shown on the bottom plane for comparison. Iso-density surfaces of 30 dBZ, 40 dBZ and 50 dBZ are shown in green, yellow and red, respectively. The white arrow indicates the direction of the thunderstorm movement. TETRA is located under the trailing edge of the storm – just below Port Allen. The bottom plane of the image is approximately 90 km by 50 km.

Higher (see Fig. 6.8 and preceding discussion). For comparison, summer thunderstorms in Louisiana often reach up to 15-18 km (50 to 60 kft). This variation in altitude is caused by the seasonally varying altitude of the tropopause. These altitudes are comparable with the TGF production altitudes of 10-15 km previously discussed [Dwyer and Smith, 2005; Grefenstette et al., 2008; Shao et al., 2010; Gjesteland et al., 2010; Cummer et al., 2011; Xu et al., 2012].

Thunderstorms associated with squall lines produced the remaining half of the TGFs observed by TETRA. The general structure of squall line thunderstorms is shown in Fig. 6.4. As with single cell thunderstorms, the updraft of a squall line thunderstorm is located at the front of the storm with the heavy precipitation (downdraft) immediately behind. In some cases, the updraft of the storm is strong enough to break through the tropopause, causing the protruding cloud shown in the top right of the image. Developed squall lines also have trailing stratiform clouds, producing additional light rain in the rear of the storm. The trailing clouds associated with squall lines can extend to hundreds of kilometers downdraft of the storm. The tops of these storms often take the shape of an anvil and can cover several thousand square kilometers.
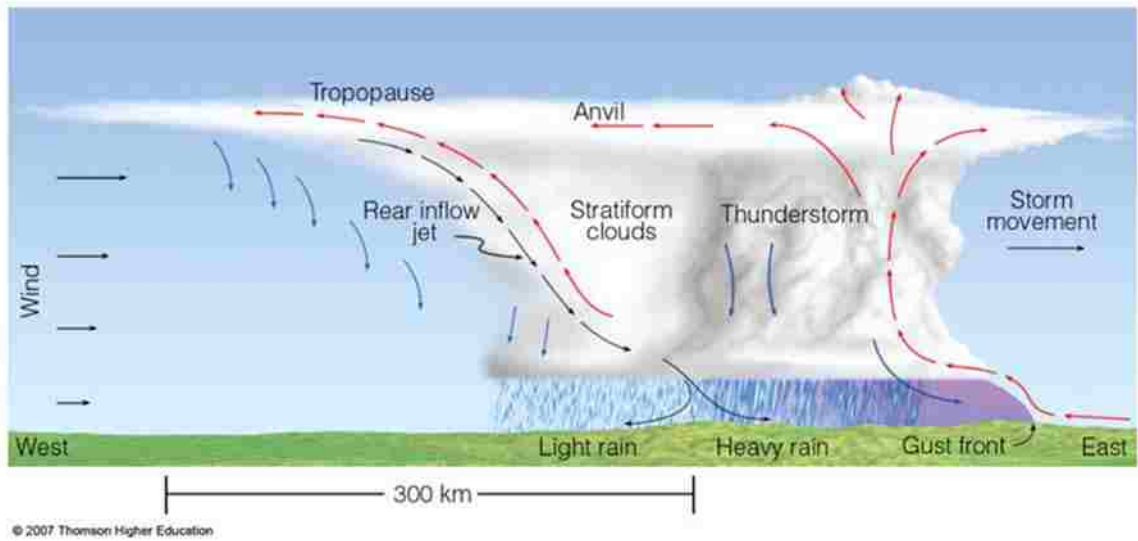
Figure 6.4 Basic structure of a squall line thunderstorm. From Ackerman and Knox, 2007.

Squall line thunderstorms can extend not only for hundreds of kilometers downdraft of the storm front, but also for hundreds of kilometers along the storm front. An example of a squall line thunderstorm is shown in Fig. 6.5. This thunderstorm produced the TGF observed by TETRA on 29 Jun 2013 at the time of the image. The smoothed radar image was produced in the same manner as Fig. 6.2. The main squall line extends from Livingston, LA to Breaux Bridge, LA – approximately 120 kilometers in length. The trailing stratiform clouds extend north to New Roads, LA (approximately 50 km from the front of the storm). The storm is moving southeast towards the Gulf of Mexico as

37

indicated by the white arrow. As in Fig. 6.2, the colors in the image correlate to the varying densities of the cloud at the lowest elevation angle (see scale in image). The green triangles in the southern section of the image indicate the location of hail less than an inch in diameter detected by NEXRAD algorithms [Stumpf et al., 1997]. The red square is the location of TETRA.

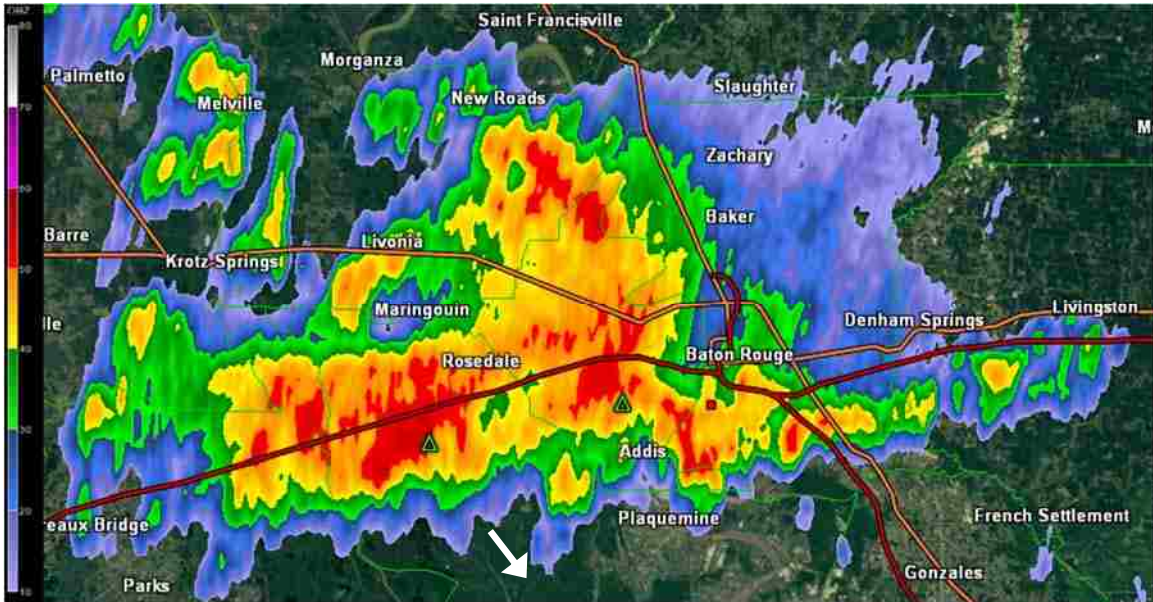Figure 6.5 Smoothed radar image of a squall line of thunderstorms producing the TETRA TGF on 29 Jun 2013. Colors in the image correlate to the density of the cloud in decibels at the lowest elevation angle (0.5°) as indicated in the scale at left. The white arrow indicates the direction of storm movement. The green triangles indicate the location of hail. The red square is the location of TETRA. Local interstates and highways are shown with red and orange lines near the top of the image. The locations of various cities are also labeled for reference. The image is approximately 120 km by 60 km.

For the 17 storms observed to produce TETRA TGFs, the position of the array relative to the updraft and the maturity of the storms at the time of the events were recorded. Based on the arguments above, the updraft of the storms was assumed to be located at the front of the storm with downdrafts trailing behind. For the majority of the storms, TETRA events were correlated with collapsing cloud formations.

One such storm produced two TETRA TGFs on 22 Jun 2013 within 15 minutes. Figure 6.6 shows the smoothed radar image of the storm at the time of the first event. The storm is located above TETRA and is gradually moving southwest towards Addis, LA. As in Figs 6.2 and 6.5, the colors in the image correspond to the cloud densities at the lowest elevation. Based on the examples above, the storm is classified as a single cell thunderstorm. The main updraft of the storm is directly above TETRA when the TGFs are observed. A time sequence of nine three-dimensional radar images of the storm is included in Fig. 6.7. In general, radar images are taken every four to five minutes (as soon as the previous scan is completed). The sequence starts about ten minutes (two

scans) before the first event and continues until about ten minutes (two scans) after the second event. Thus, the nine images in the sequence show the behavior of the storm over 45 minutes. The colored cloud surfaces in the image correspond to iso-density surfaces of 30 (green), 40 (yellow) and 50 (red) decibels as in Fig. 6.3. The storm is viewed from the northeast from a slightly tilted angle and, the altitudes are given in tens of thousands of feet. The smoothed radar image at each time is shown on the bottom plane. The time of the radar scan is given in Coordinated Universal Time (UTC) at the top of each image. The radar images taken closest to the time of the TGFs are labeled above the time at the top of the images.

Figure 6.6 Smoothed radar image of the storm producing two TETRA TGFs on 22 Jun 2013. Image was taken at the time of the first TETRA TGF. Colors in the image correlate to the density of the cloud in decibels at the lowest elevation angle as indicated in the scale at left. The white arrow indicates the direction of storm movement. The red square is the location of TETRA. Local interstates and highways are shown with red and orange lines near the top of the image. The locations of various cities are also labeled for reference. The image is approximately 25 km by 40 km.
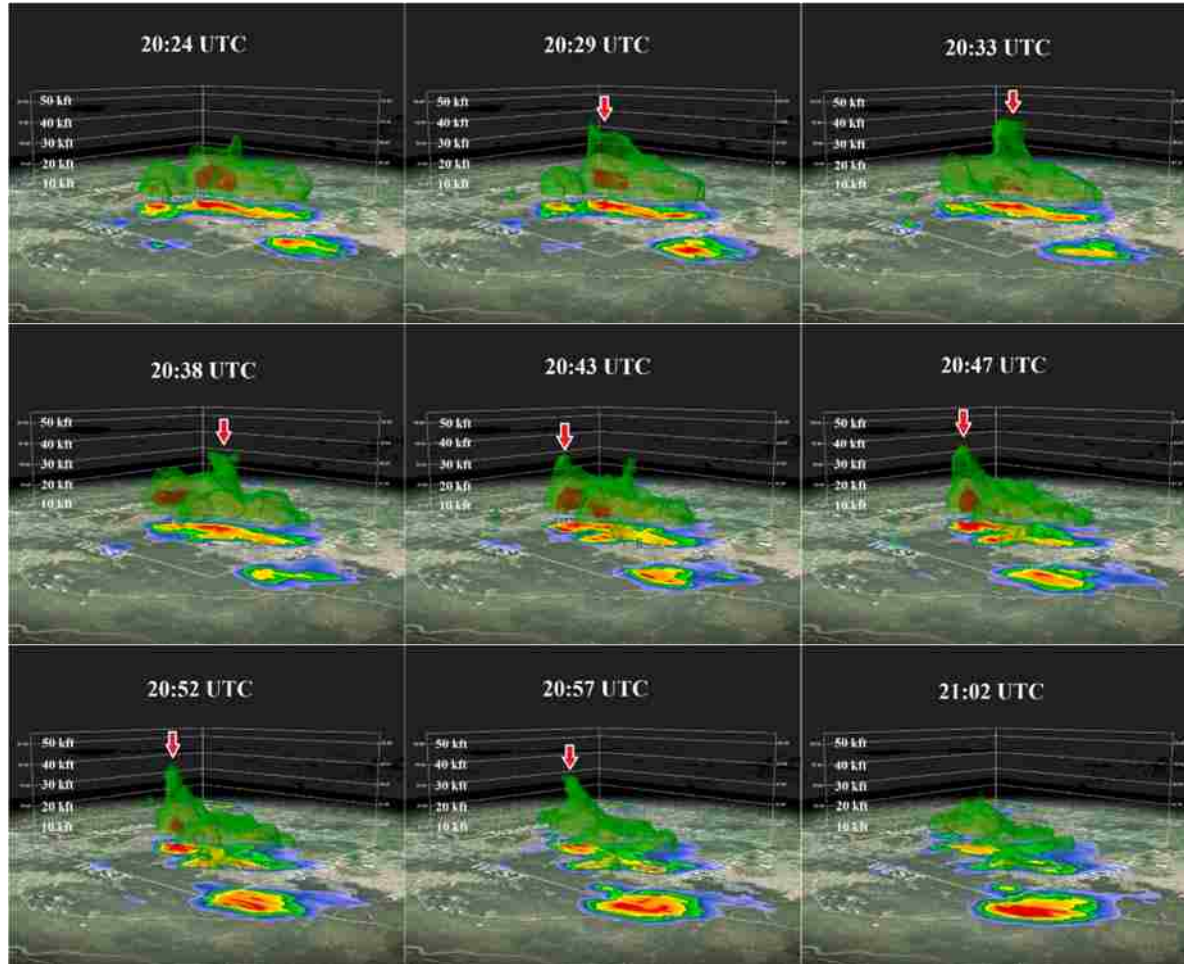
Figure 6.7 Three dimensional radar image sequence of the thunderstorm producing two TETRA TGFs on 22 Jun 2013. Time (hh:mm UTC) is indicated at the top of each image. The red arrows point to cloud features near TETRA with decreasing altitude. TETRA is located at the center of the bottom plane in each panel. Each panel is similar to Fig. 6.3. The TETRA TGFs were observed at 20:31 and 20:52 UTC. The bottom plane of each image is approximately 30 km by 30 km.

The sequence begins during the initial intensifying stage of the storm. In the first image, the updraft is beginning to form a cloud tower directly above TETRA. By the third image (20:33 UTC), the cloud tower is well defined and subsequently collapses after the TGF at 20:31 UTC. A second cloud tower forms by 20:47 UTC, and also collapses after the second TGF at 20:52 UTC. After these two events are observed, the storm completely dissipates.

In a more detailed analysis, various properties of the storm associated with the TETRA TGFs on 22 Jun 2013 are plotted to show the behavior of the storm from its initial development to 30 minutes after the TGFs were produced. Publicly available NEXRAD data obtained from http://www.ncdc.noaa.gov/nexradinv/ were used to track and analyze the storm throughout its lifetime.

As a measure of the intensity of the thunderstorm, the echo top and the total vertically integrated liquid density (VILD) water content of the storm were calculated for each radar image throughout the lifetime of the storm (Fig. 6.8). The echo top (or estimated top) is the maximum height of the cloud with a reflectivity value of 18.5 dBZ or higher (solid line, right-hand scale). Vertically integrated liquid (VIL) is the amount of liquid water that the radar detects in a vertical column of the atmosphere. VIL density (VILD) is the VIL value divided by the estimated top (dashed line, left-hand scale), corresponding
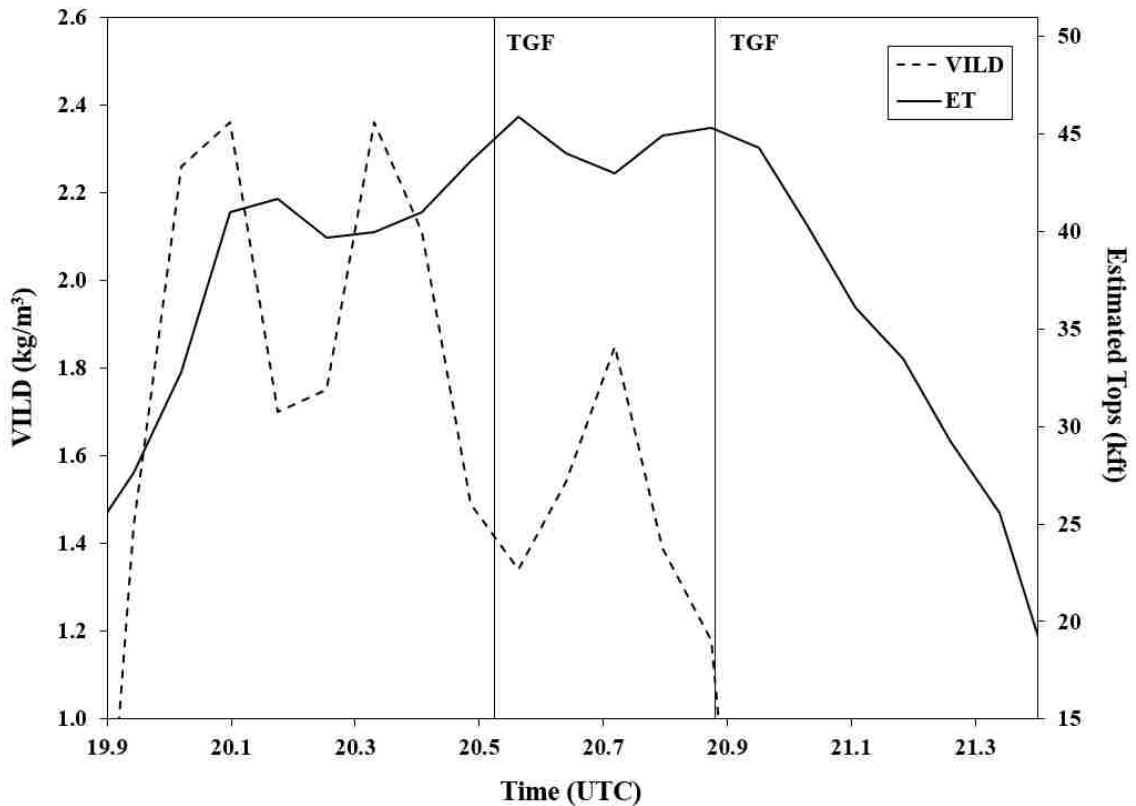

Fig. 6.8 VILD and Estimated Tops of the storm on 22 Jun 2013. The TGF times are marked with labeled vertical lines.

41

to the size of the particles inside the cloud. The times of observed TGFs are indicated with vertical lines.

As shown in Fig. 6.8, the VILD of the thunderstorm reaches 2.4 kg/m^3 about 20 minutes before the first TGF is observed. At this time, the estimated top of the storm is also increasing. The first TETRA TGF is observed when the VILD decreases to 1.4 kg/m^3 and the estimated top is above 45000 feet. The storm cloud then begins to collapse, thus increasing the VILD to 1.85 kg/m^3. As the cloud top begins to increase in height to above 45000 feet again, the VILD again decreases and a second TGF is observed by TETRA at 20:52 UTC with the estimated cloud top again above 45000 feet. After the second TGF, the VILD values fall below 1kg/m^3 and the cloud formation collapses, falling below 20000 feet within 35 minutes. No other TGFs were observed from this storm.

The lightning network used in this study is a very low frequency (VLF) lightning detection array. In general, VLF arrays are primarily used for cloud-to-ground (CG) lightning detection due to the stronger emission of CG lightning radio signals in this frequency band. (Note the sparsity of lightning with small current (intracloud (IC)) compared to the amount of lightning with non-zero current (CG) in Figure 4.8.) Although VLF lightning arrays are capable of detecting a small percentage of IC lightning, high frequency (HF) and very high frequency (VHF) lightning arrays have been proven to detect both CG and IC lightning radio signals more efficiently [Hager et al., 2010].

Several studies have correlated total (IC + CG) lightning behavior with the onset of severe weather [Metzger and Nuss, 2013; Steiger et al., 2007]. In general, an increase in IC lightning rate implies an increase in thunderstorm intensity and probable impending severe weather. CG lightning rates are less strongly correlated with severe weather events such as tornadoes, hail and severe wind [Schultz et al., 2011]. In the current analysis, the total and individual -CG, +CG, and IC lightning rates are shown in Fig. 6.9. These rates include all lightning detected by the USPLN within 10 miles of TETRA, binned into 5 minute sections for comparison with the radar properties of the storm. The two TGFs are observed during an abrupt increase in the total and -CG lightning rates.

The analysis above shows the storm on 22 Jun 2013 to be collapsing at the time of the TGFs produced. This conclusion is supported by the increase in VILD and the decrease in the estimated cloud height (Fig. 6.8). At the same time, jumps in the total and -CG lightning rates (Fig. 6.9) occur. It is unknown if the eventual collapse of the storm is due to the production of the two TGFs, or another entirely different cause.

Out of the 18 storms analyzed, 14 storms were found to produce cloud formations with decreasing maximum altitude (estimated tops) near the time of the TGFs observed by TETRA. For three of these storms, no change in cloud altitude was detected. The remaining storm actually showed an increase in cloud height at the time of the event. This particular storm produced the CEC and EC observed by TETRA on 18 Aug 2011 (see Table 5.1 for details). Three-dimensional time sequences for each storm are shown in Figures 6.7 and 6.10 – 6.26.
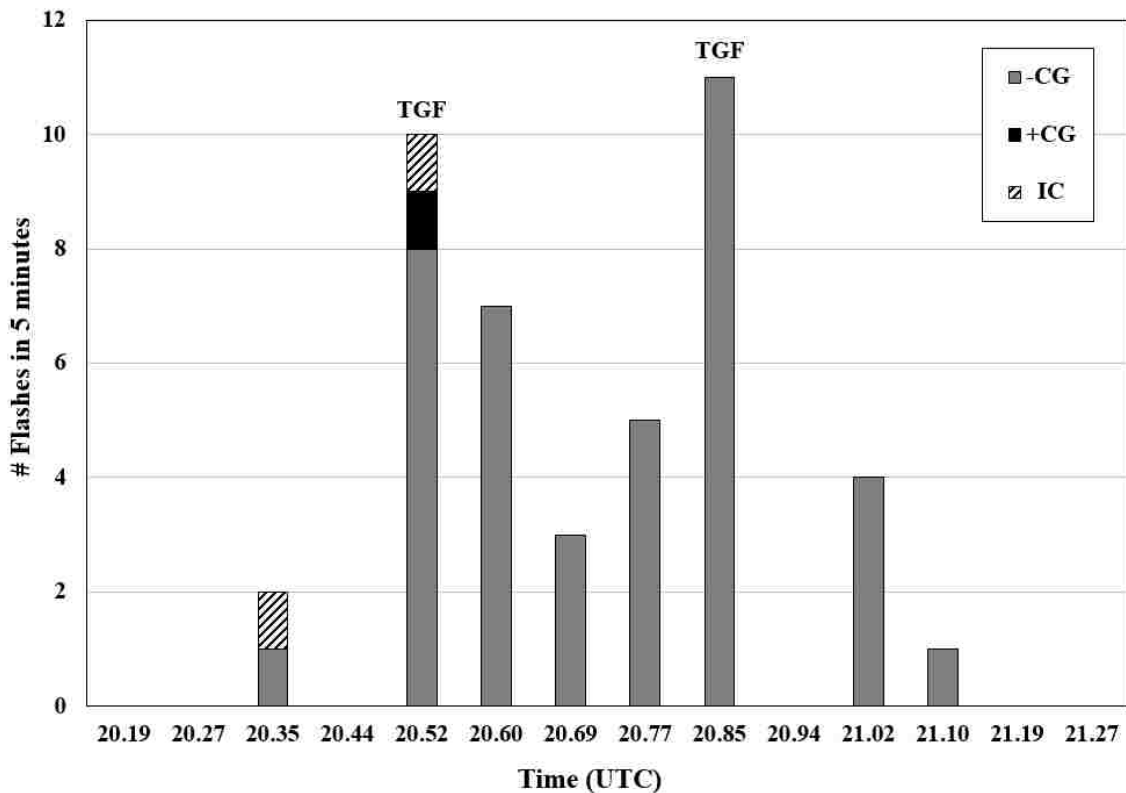
Fig. 6.9 Lightning flash rate observed with the storm producing the TETRA TGFs on 22 Jun 2013. The TGF times are labeled.

The analysis presented here correlates 22 TGFs with cloud formations with decreasing altitude (Figs. 6.7, 6.10, 6.11, 6.12, 6.14, 6.15, 6.17, 6.18, 6.19, 6.20, 6.21, 6.22, 6.25 and 6.26). Three of the remaining TGFs were produced by storms exhibiting no change in cloud altitude near the times the TGFs were observed (Figs. 6.16, 6.23 and 6.24). As described earlier, two TGFs were produced by an intensifying storm passing over TETRA (Fig. 6.13). Although the association of these TGFs with collapsing clouds does not classify TGFs as an indicator of decreasing storm strength, it does serve as an example for future work. In order to test this relationship, other TGF-producing storms should be analyzed in a similar fashion. If TGFs can indeed be established as an indicator of storm collapse, then TGFs may potentially be used in conjunction with other radar properties in the prediction processes of meteorologists. Instead of attempting to detect TGFs from the ground over large areas, the specific lightning signatures produced by TGFs (described in Cummer et al. [2011]) can be used to report these TGFs in real time to meteorologists.

Figure 6.10 Three dimensional radar image sequence of the thunderstorm producing one TETRA TGF on 24 Feb 2011. Similar to Fig. 6.7. The TETRA TGF was observed at 05:11 UTC.

Figure 6.11 Three dimensional radar image sequence of the thunderstorm producing one TETRA TGF on 29 Jul 2011. Similar to Fig. 6.7. The TETRA TGF was observed at 16:39 UTC.

Figure 6.12 Three dimensional radar image sequence of the thunderstorm producing two TETRA TGFs on 31 Jul 2011. Similar to Fig. 6.7. The TETRA TGFs were both observed at 22:21 UTC within 400 milliseconds.

Figure 6.13 Three dimensional radar image sequence of the thunderstorm producing two TETRA TGFs on 18 Aug 2011. Similar to Fig. 6.7. The TETRA TGFs were both observed at 23:57 UTC within 300 milliseconds. The absence of red arrows indicates no decrease in altitude was observed near the TGF times.
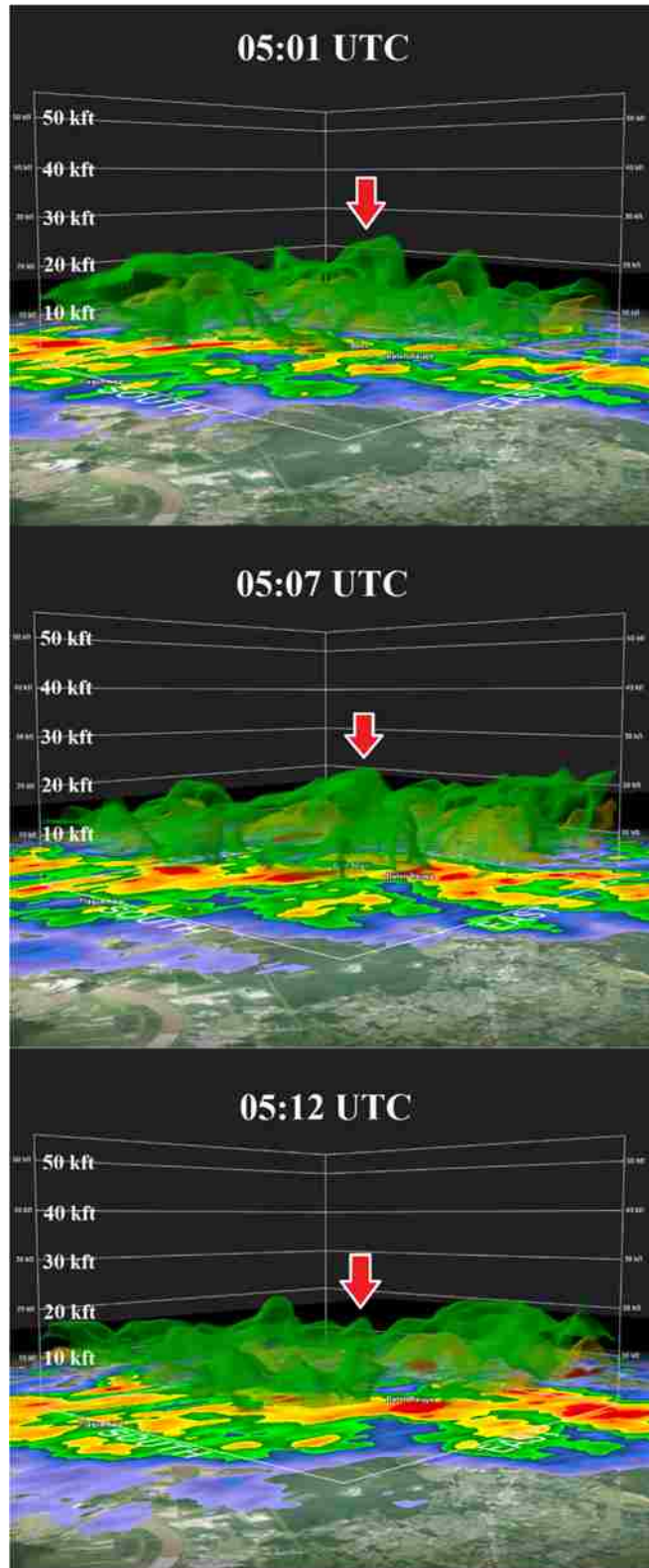
Figure 6.14 Three dimensional radar image sequence of the thunderstorm producing one
TETRA TGF on 12 Mar 2012. Similar to Fig. 6.7. The TETRA TGF was observed at
17:30 UTC.
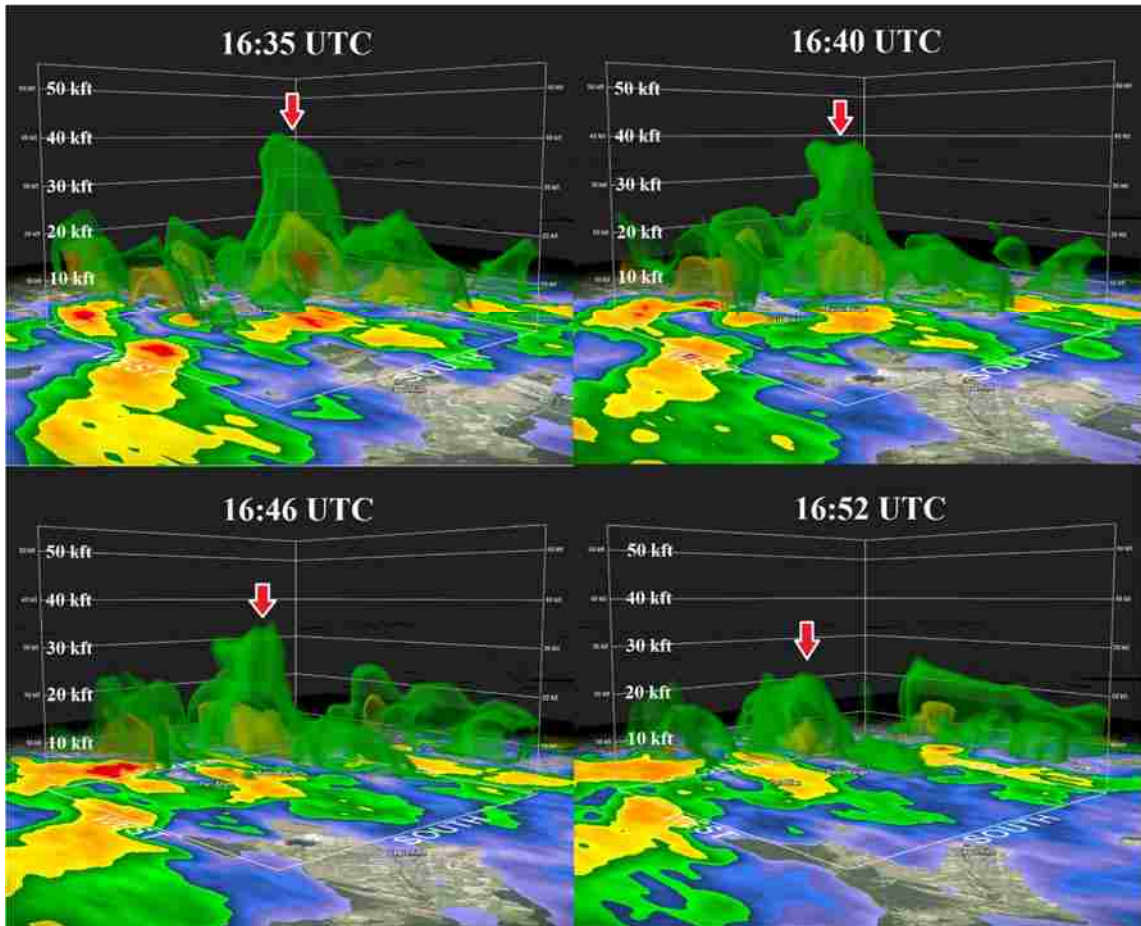
Figure 6.15 Three dimensional radar image sequence of the thunderstorm producing one TETRA TGF on 2 Apr 2012. Similar to Fig. 6.7. The TETRA TGF was observed at 18:29 UTC.

Figure 6.16 Three dimensional radar image sequence of the thunderstorm producing one TETRA TGF on 4 Apr 2012. Similar to Fig. 6.7. The TETRA TGF was observed at 08:49 UTC. The absence of red arrows indicates no decrease in altitude was observed near the TGF times.
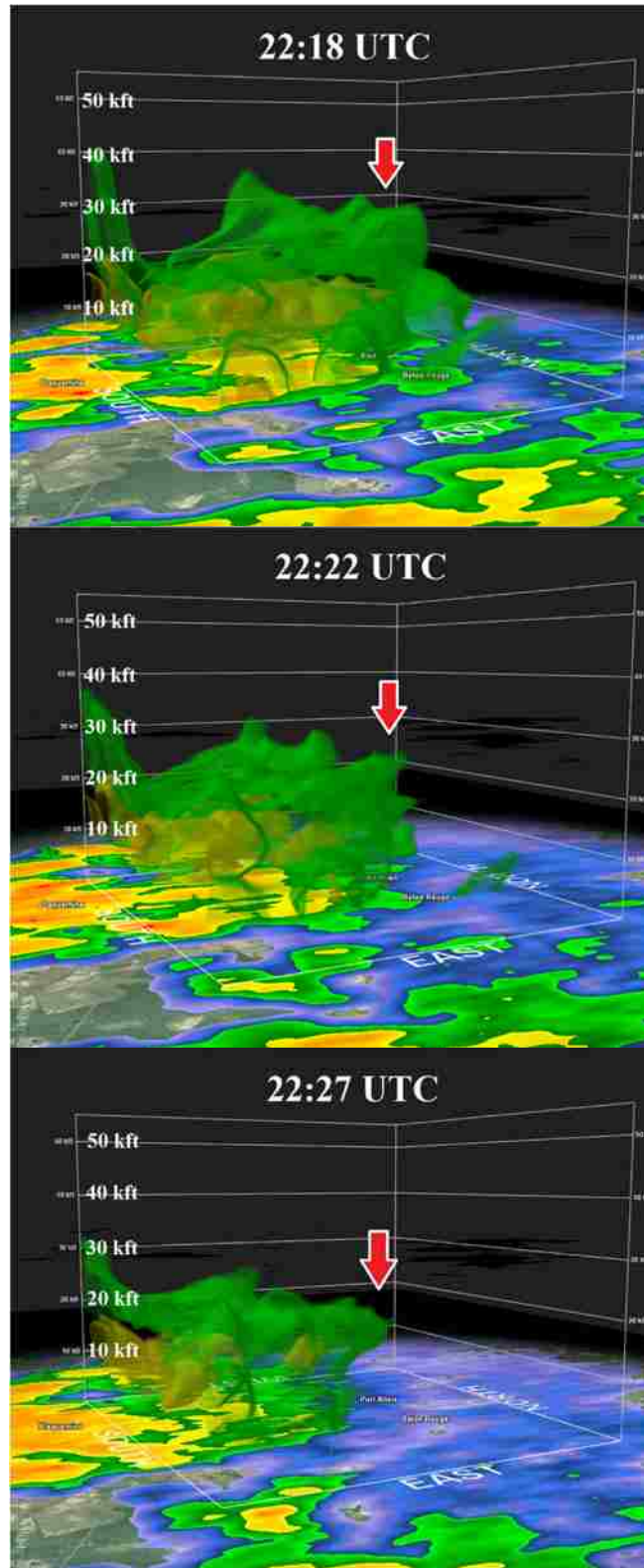
Figure 6.17 Three dimensional radar image sequence of the thunderstorm producing two TETRA TGFs on 6 Jun 2012. Similar to Fig. 6.7. The TETRA TGFs were observed at 21:37 and 21:44 UTC.
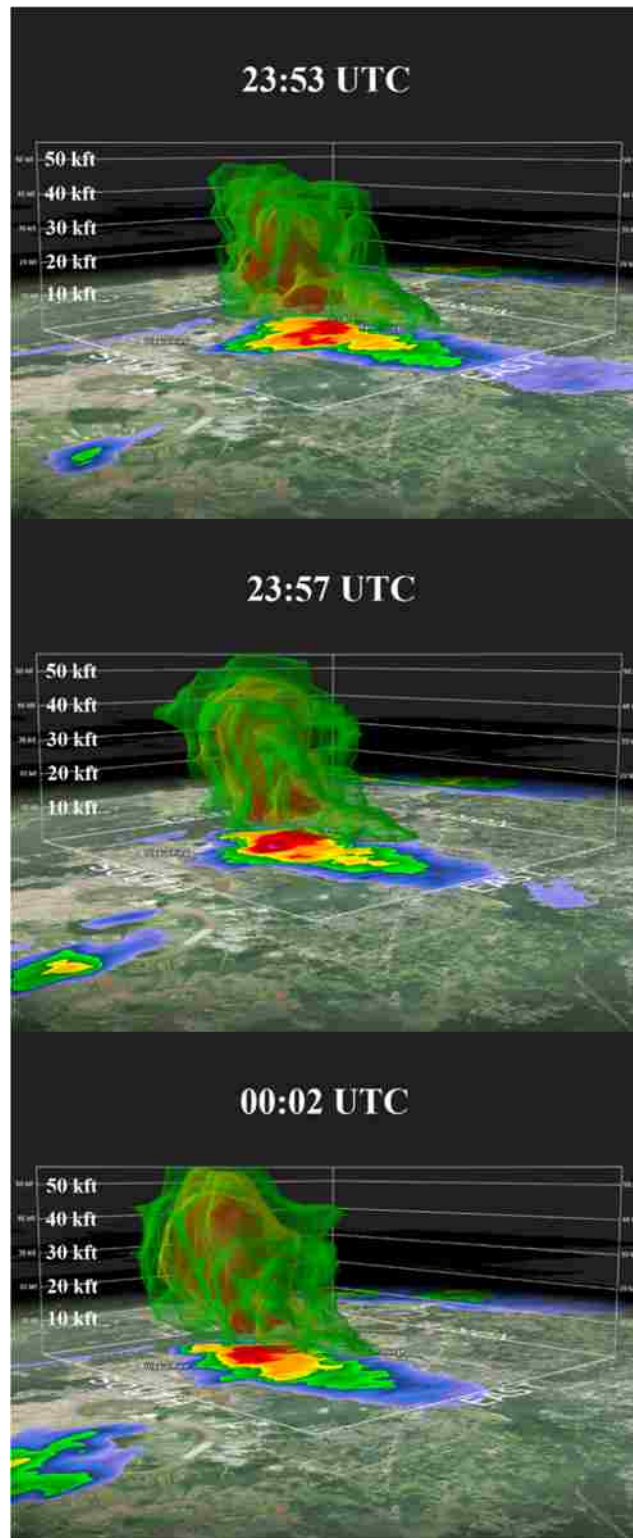
Figure 6.18 Three dimensional radar image sequence of the thunderstorm producing three TETRA TGFs on 6 Jun 2012. Similar to Fig. 6.7. The TETRA TGFs were observed at 01:29, 01:31 and 01:36 UTC.

Figure 6.19 Three dimensional radar image sequence of the thunderstorm producing one TETRA TGF on 5 Aug 2012. Similar to Fig. 6.7. The TETRA TGF was observed at 20:43 UTC.

Figure 6.20 Three dimensional radar image sequence of the thunderstorm producing one TETRA TGF on 6 Aug 2012. Similar to Fig. 6.7. The TETRA TGF was observed at 01:17 UTC.
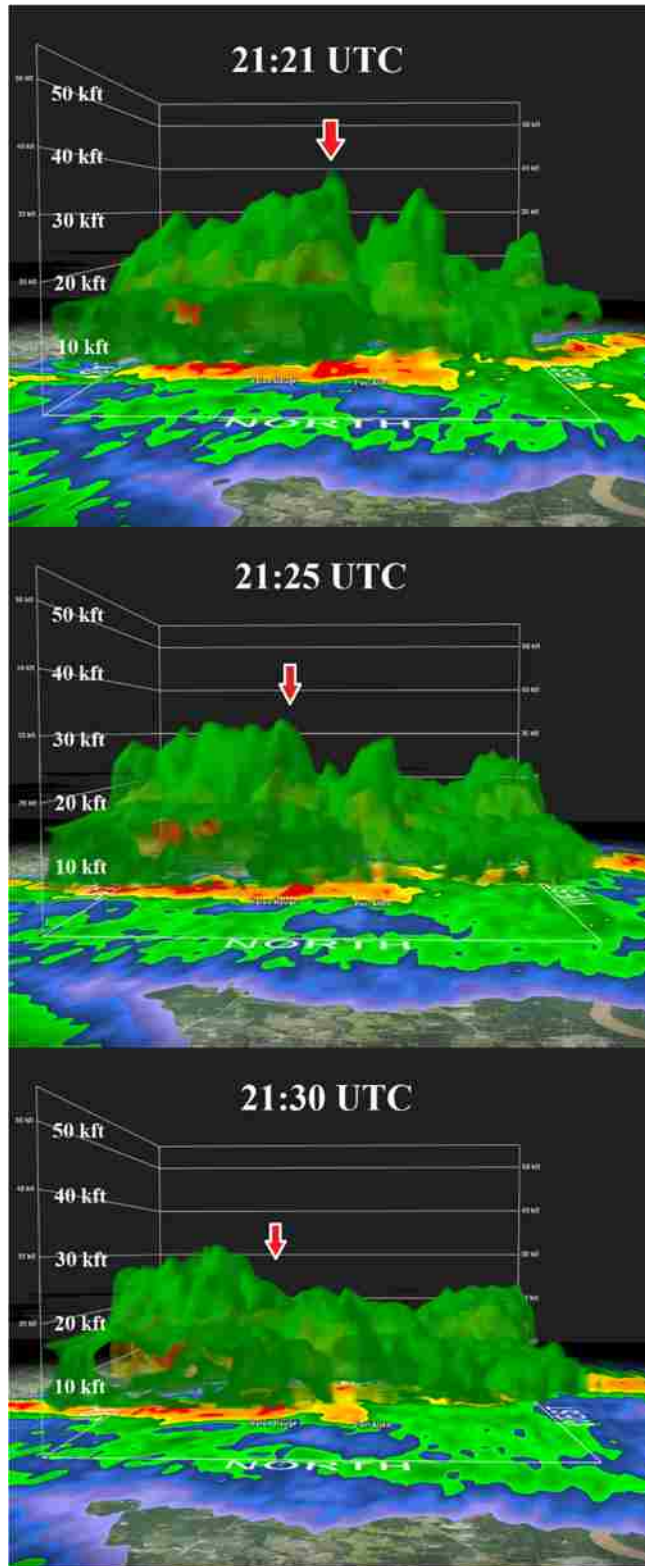
Figure 6.21 Three dimensional radar image sequence of the thunderstorm producing three TETRA TGFs on 9 Aug 2012. Similar to Fig. 6.7. The TETRA TGF were all observed at 21:28 UTC within 7 seconds.
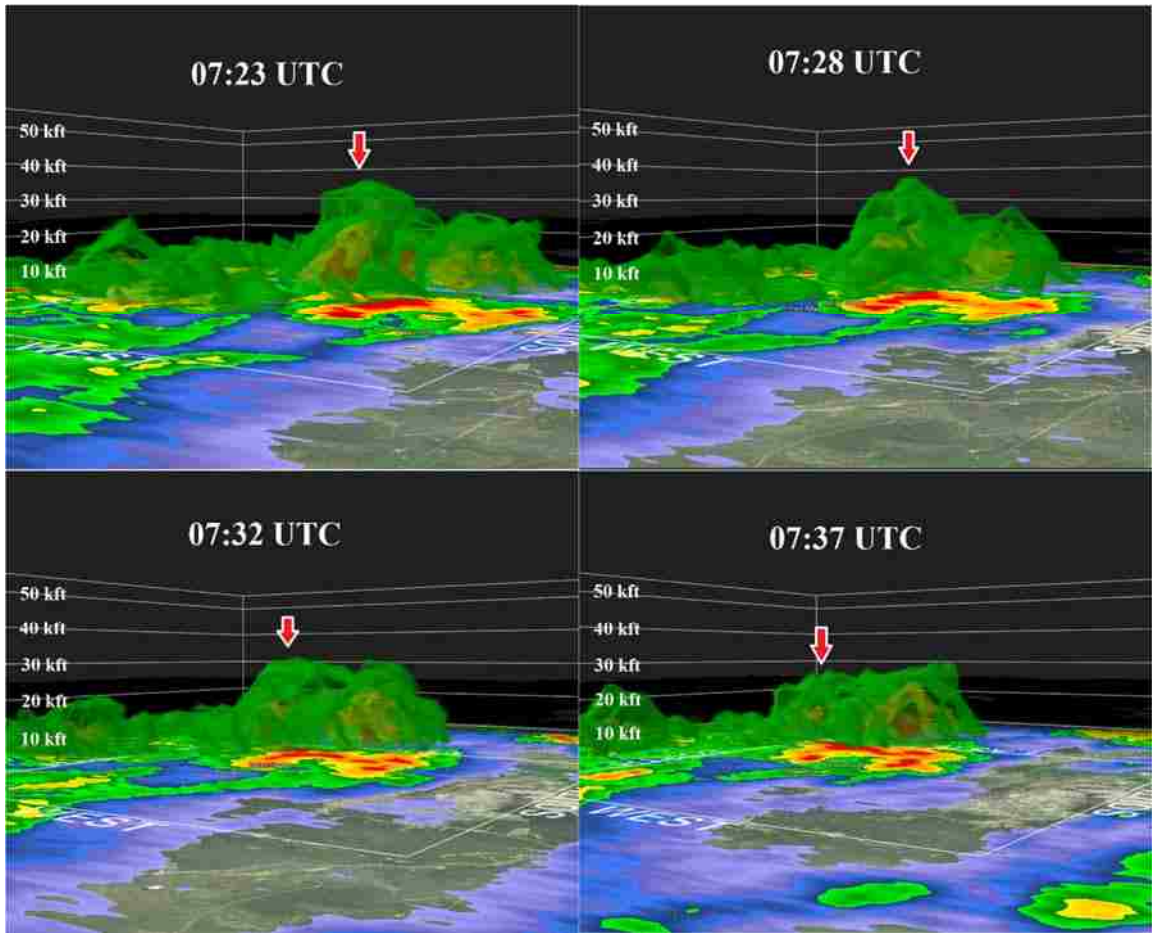
Figure 6.22 Three dimensional radar image sequence of the thunderstorm producing one TETRA TGF on 14 Apr 2013. Similar to Fig. 6.7. The TETRA TGF was observed at 07:26 UTC.
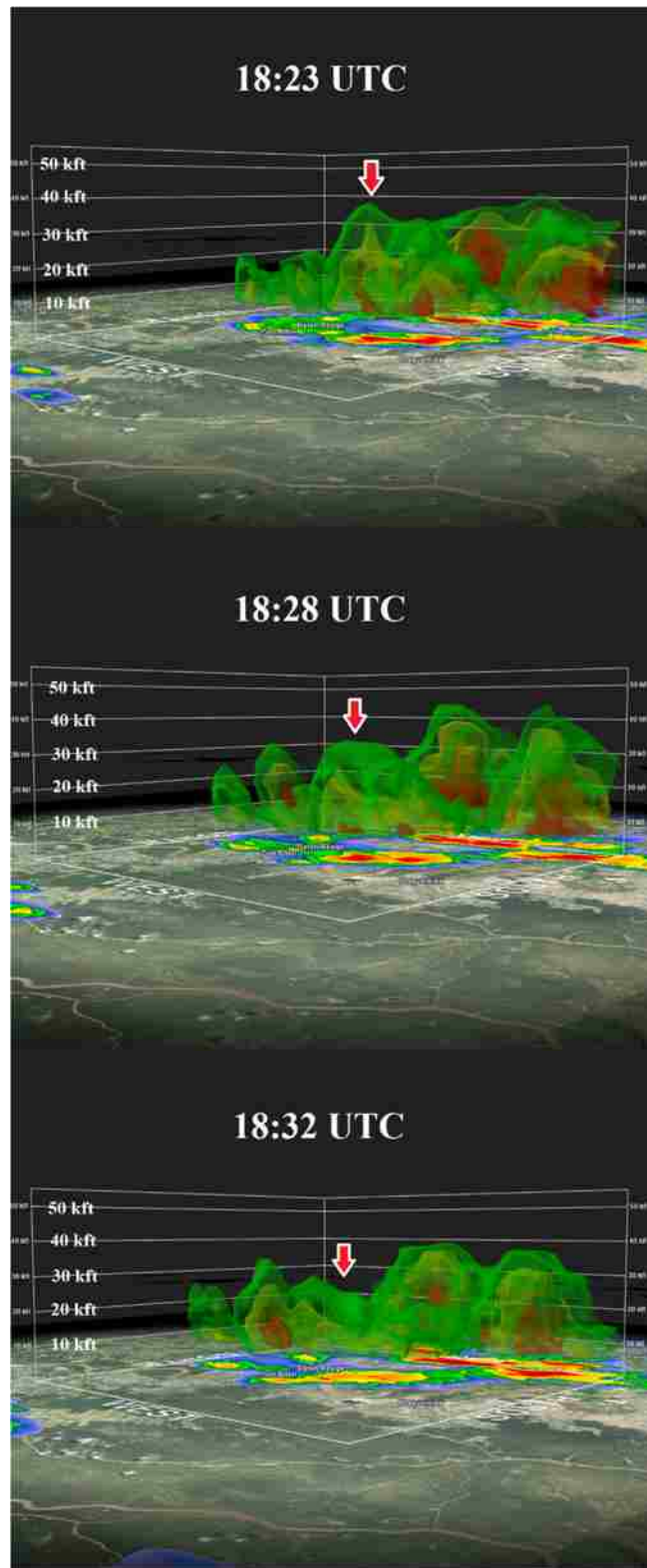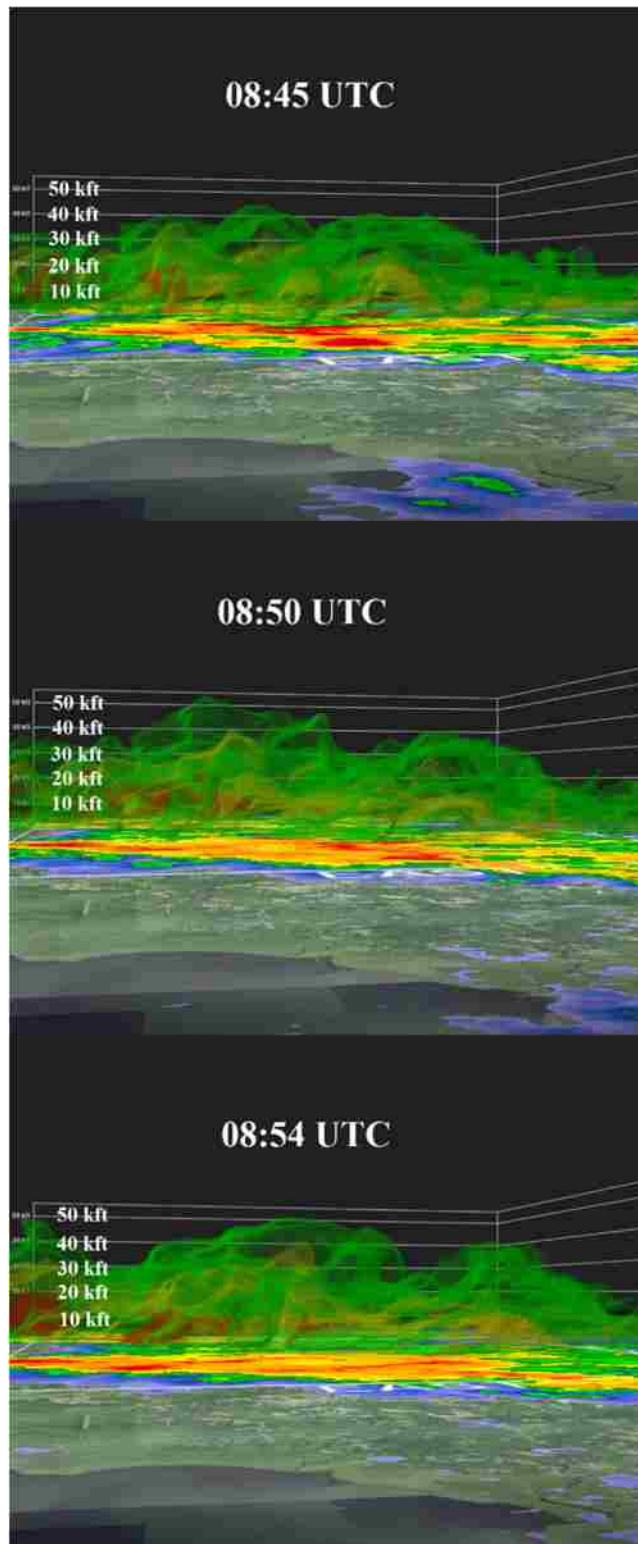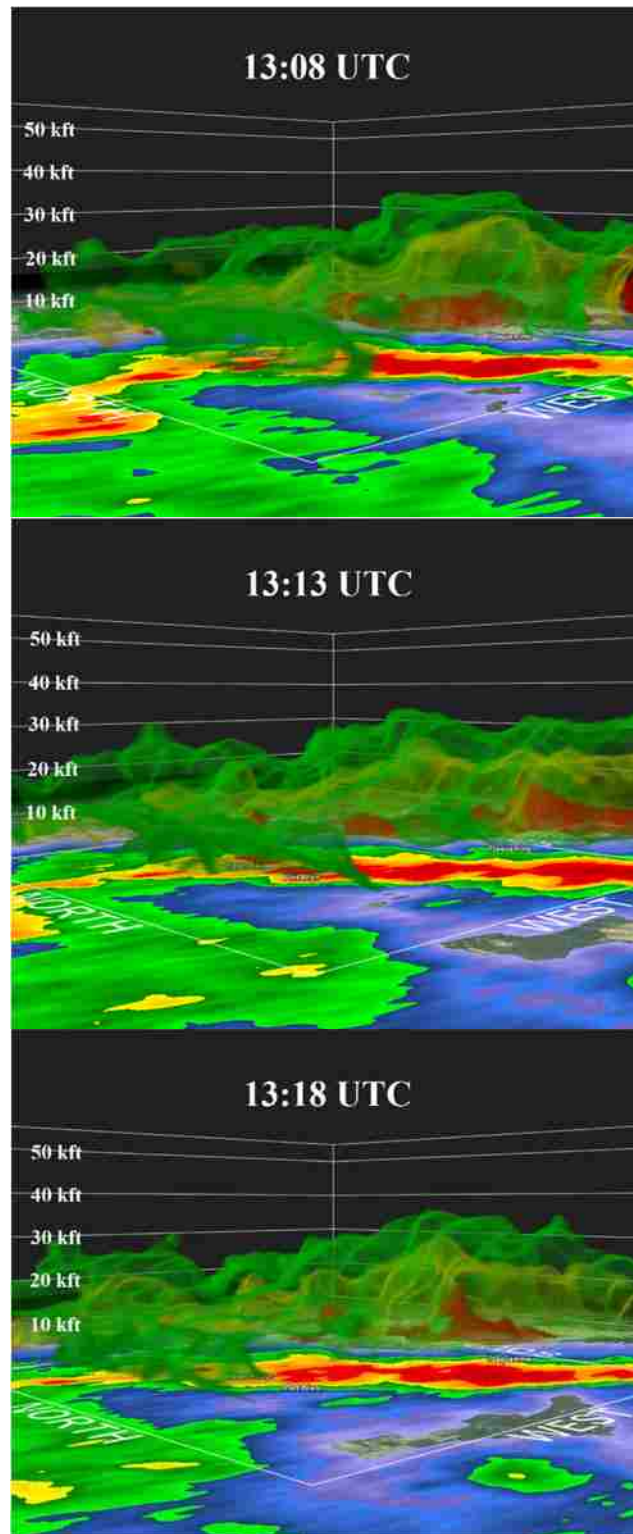
Figure 6.23 Three dimensional radar image sequence of the thunderstorm producing one TETRA TGF on 24 Apr 2013. Similar to Fig. 6.7. The TETRA TGF was observed at 13:11 UTC. The absence of red arrows indicates no decrease in altitude was observed near the TGF times.
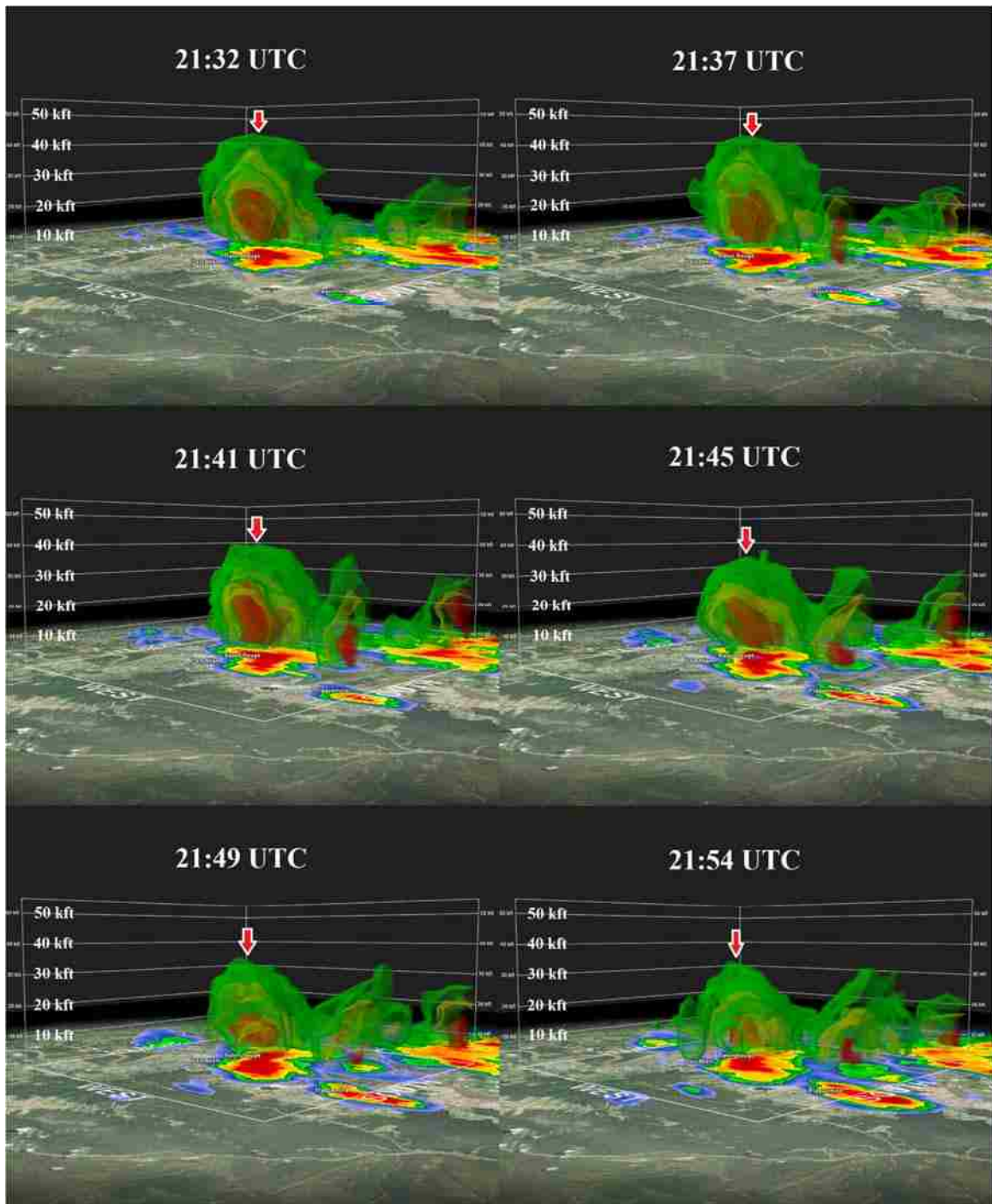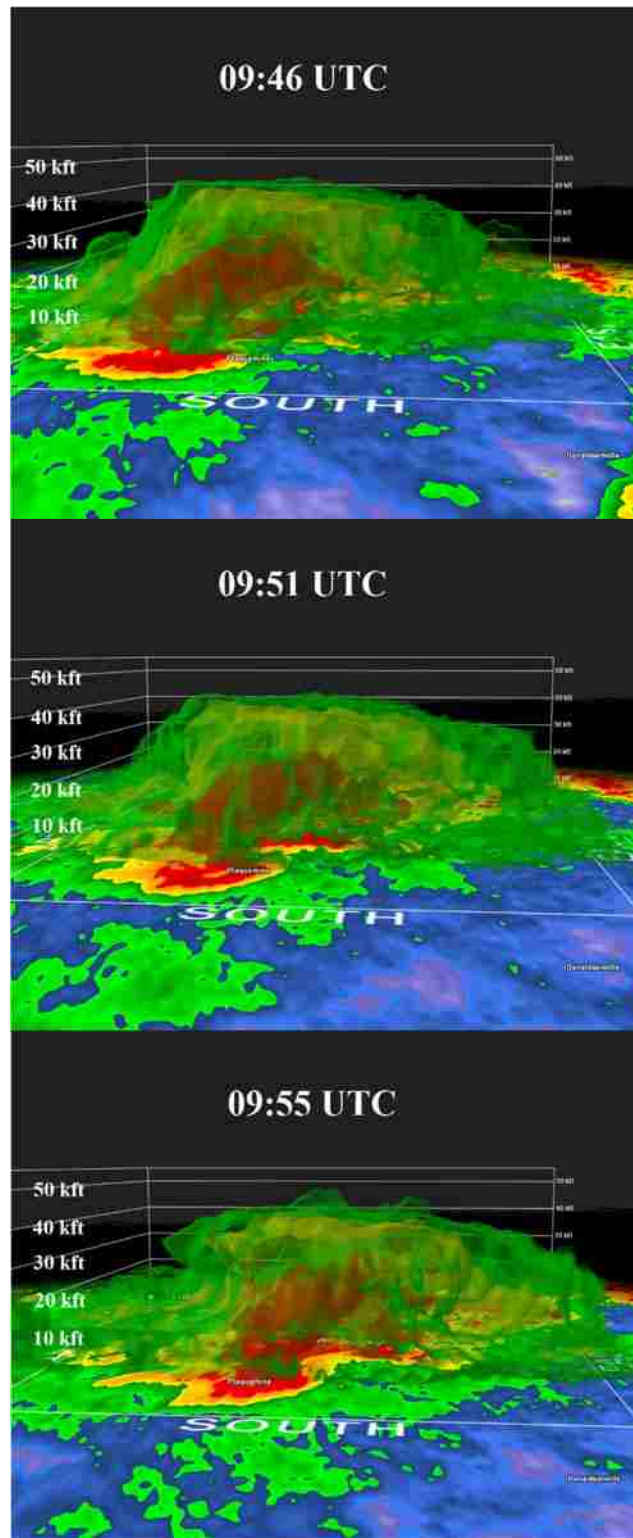
Figure 6.24 Three dimensional radar image sequence of the thunderstorm producing two TETRA TGFs on 10 May 2013. Similar to Fig. 6.7. The TETRA TGFs were observed at 09:51 UTC within 700 milliseconds. The absence of red arrows indicates no decrease in altitude was observed near the TGF times.

Figure 6.25 Three dimensional radar image sequence of the thunderstorm producing two TETRA TGFs on 29 Jun 2013. Similar to Fig. 6.7. The TETRA TGFs were observed at 10:24 UTC within 70 milliseconds.
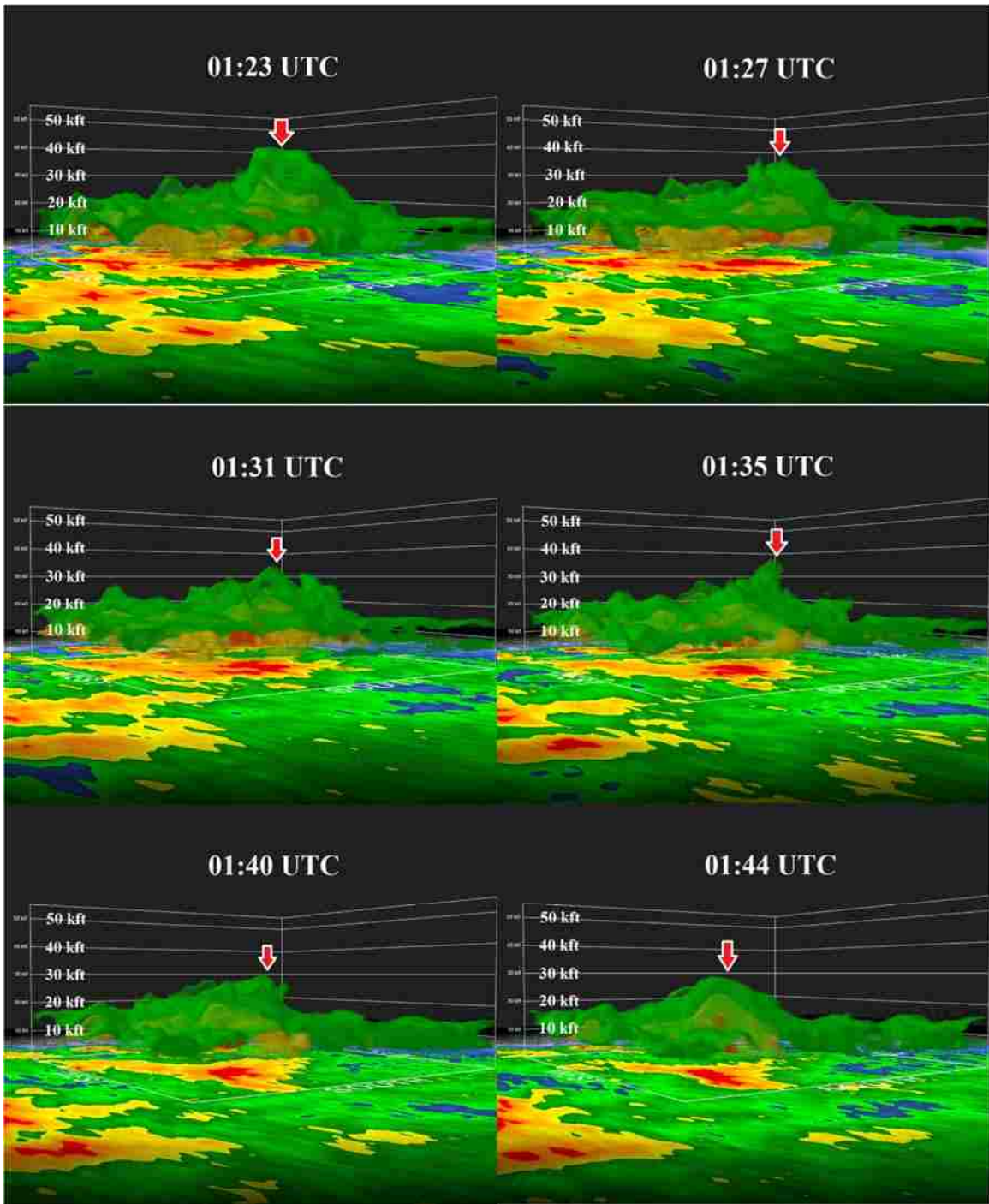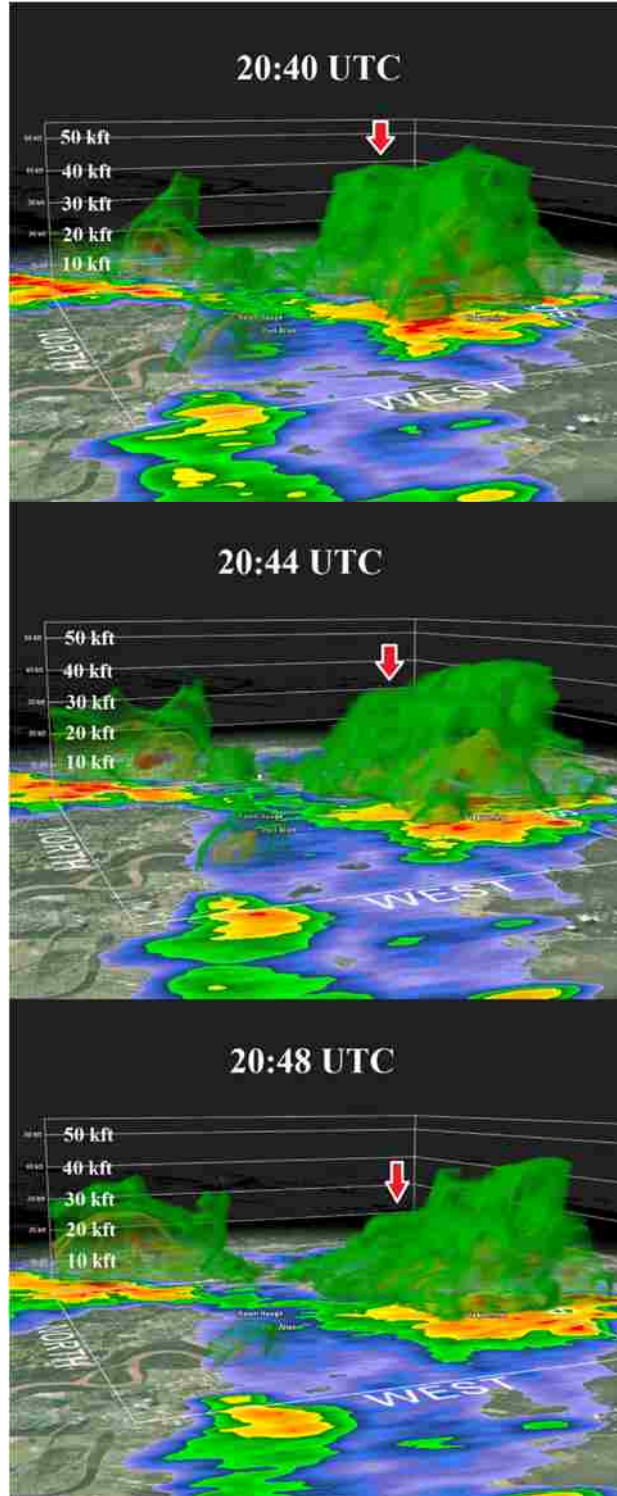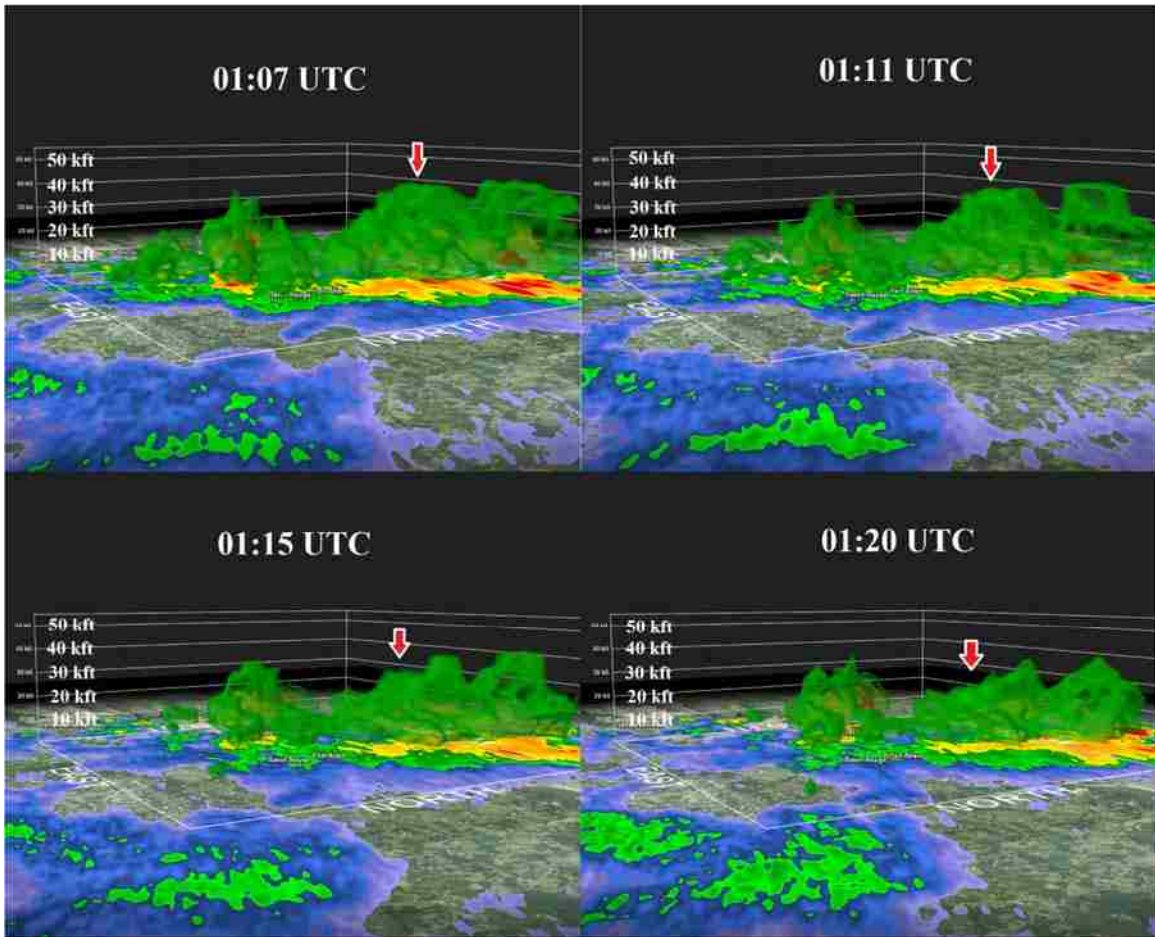
Figure 6.26 Three dimensional radar image sequence of the thunderstorm producing one TETRA TGF on 13 Sep 2013. Similar to Fig. 6.7. The TETRA TGF was observed at 00:11 UTC.
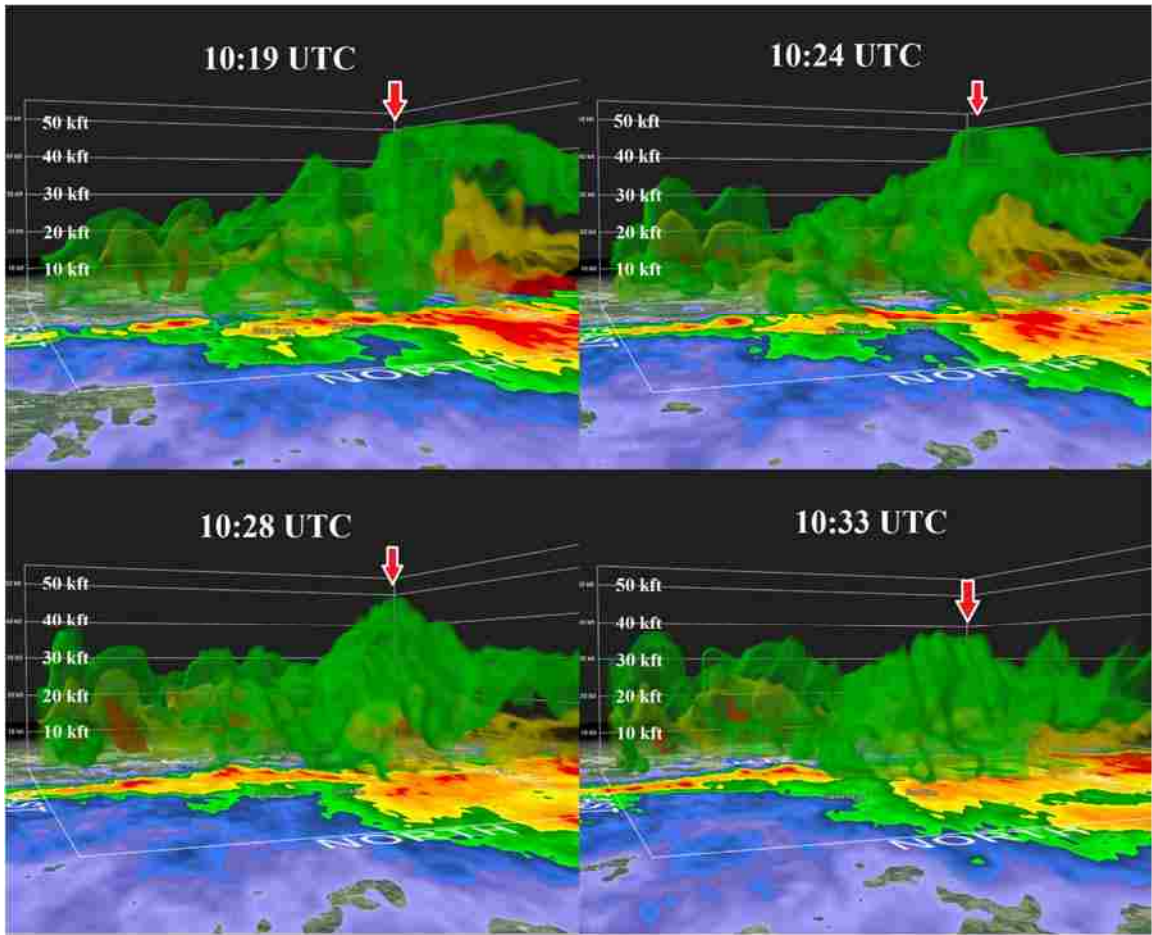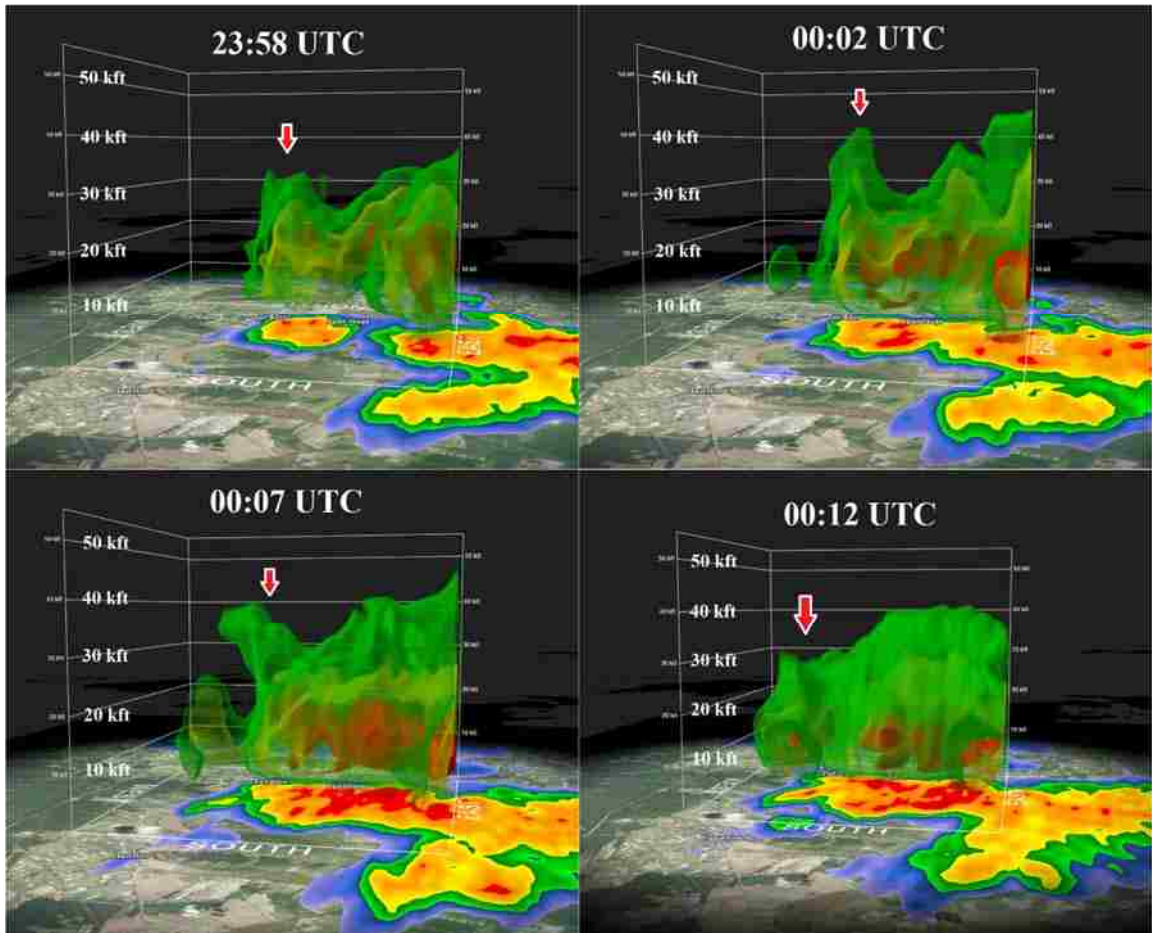
CHAPTER 7 – LAGO DESCRIPTION AND ANALYSIS

TGF observations from satellite platforms are limited by the event beaming direction and attenuation and Compton scattering by the atmosphere. Although these events observed from space are extremely intense (gamma ray rates in excess of 300 kHz measured with BATSE), the bulk of the events are presumably smaller events which can only be observed much closer to the lightning -- i.e., at aircraft or balloon altitude [Smith et al., 2011; Briggs et al., 2013; Gjesteland et al., 2012; Østgaard et al., 2012]. Observations in the atmosphere are necessary to better understand the TGF intensity distribution and emission pattern, to understand whether the observed 30° beaming is intrinsic to the emission process or is the result of atmospheric attenuation, and to measure the spectrum vs altitude relationship. This chapter describes a program to observe TGFs at balloon altitudes.

The Lightning Associated Gamma-ray Observer (LAGO) is a 50 lb (23 kg) balloon payload stationed at the Columbia Scientific Ballooning Facility (CSBF) in Palestine, TX. LAGO consists of an array of four $1'' \times 1'' \times 5''$ bismuth germanate (BGO) crystal scintillators designed to detect gamma-ray emissions from lightning below the payload in the ranges 300 keV - 3 MeV and 10 MeV to more than 20 MeV. In order to minimize the distance between the payload path and the thunderstorm path, LAGO must be launched within a few hours prior to the arrival of the storm at the launch site, placing a strict upper limit on the size of the high altitude balloon needed to support the weight of the payload. Due to these limitations, the Winzen 0.194 million cubic foot Stratofilm high altitude balloon was chosen. Like TETRA, LAGO also operates in a self-triggered mode, allowing for post-flight correlations of detected events with lightning.

The four BGO scintillators are arranged in a 2 x 2 array with one $3''$ (76 mm) diameter Lucite lightguide coupled to each end of the array (Fig. 7.1). The BGO scintillator array is housed in ~ ½″ thick plastic foam insulation to prevent rapid temperature changes in the crystals. The light at each end is viewed through optical grease by a potted Electron Tubes 9305KFLA 78 mm photomultiplier tube (PMT) with ten dynodes and a standard bialkali photocathode. This detector assembly is housed in a polyvinyl chloride (PVC) tube and wrapped with ~ 1″ thick plastic foam insulation. The detector is mounted on the bottom of the payload frame to view gamma-rays coming up from storms below the payload. Each PMT bleeder chain is wired to output the anode signal for low energy signals and the eighth dynode signal for higher energy signals (circuit in Appendix A).

Electronics boards above the detector supply high voltage, amplify and shape the PMT outputs, provide an internal trigger for the data acquisition software, digitize the data, assign timestamps, and record ADC values for each event. Once triggered by a PMT anode signal, each PMT anode and dynode output is integrated and assigned a 12-bit ADC value. The LAGO ADC and TLM designs are identical to TETRA except that a solid state hard drive is implemented to enable data recording during flight. These electronics boards are attached to the payload frame above the detector. Temperatures of the BGO, PMTs, and electronics boards are monitored during flight. Power to the payload and required CSBF equipment is supplied by two 30V battery packs mounted on

the outside of the payload frame above the detector viewing angle. The payload's internal time is synchronized during preflight procedures. The ADC-to-energy conversion is calibrated with radioactive sources (^{22}Na, ^{137}Cs, ^{60}Co, ^{232}Th). The detector energy resolution at 662 keV is 29.4% FWHM.

Figure 7.1 2 x 2 BGO scintillator array mounted in 4″ PVC.

As described above, the electronics boards and the PC104 stack of LAGO are almost identical to those used in TETRA. The circuit layout on the LAGO electronics boards was rearranged to conserve space. This required a slightly more complex assembly as shown in Appendix B. On LAGO, the data acquisition code version 6.5 was kept while the code on TETRA was upgraded to include GPS timing (version 8.1). To prevent arcing at high altitudes, LAGO's PMT bases were potted. Since it is not feasible to use a hard disk drive for data storage in high altitude conditions, the standard TETRA hard drive was replaced with a solid state drive.

The initial LAGO payload integration and testing occurred from Feb. 21 to Feb. 24, 2012 at CSBF in Palestine, TX. During this session, the standard CSBF equipment was integrated with the LAGO payload, the combined payload was thermal vacuum tested and the electrical and mechanical checkouts were completed. The detector's field of view was not obscured by CSBF equipment in this process. The payload was then attached to the parachute and balanced. The weight of the integrated payload was 80 lbs (36 kg), including the CSBF parachute and strobe.

The criterion for a successful balloon launch was set so that LAGO must be within a maximum lateral distance between the payload and the thunderstorm of ten standard miles. This distance was calculated using the TGF beaming angle of 30° - 45° and a flight altitude of ~100,000 ft. The thunderstorm chosen to be in the flight trajectory must also show a reasonable chance of producing a *peak* of at least 2 lightning flashes per second within 5 miles. The minimum required peak lightning flash rate was determined by finding the smallest peak lightning flash rate associated with the event candidates

reported in chapters 4 and 5. In order to increase the payload's chances of flying over a promising thunderstorm, it is better to fly over a line of strong thunderstorms, such as those that come through Palestine, TX, instead of trying to catch a scattered thunderstorm.

In the spring 2012 season, the PC104 stack suffered heat damage, requiring replacement of the stack. This prevented launch for a promising thunderstorm that came through Palestine that spring. In fall 2012, the payload was launched on High Altitude Student Payload (HASP) as an engineering flight. The data accumulated on this flight are described below. Although the payload stood ready throughout the 2013 season at Palestine, TX and at Fort Sumner, NM, no suitable flight opportunity arose. The LAGO balloon payload currently stands ready for the 2014 flight season in Palestine, TX.

LAGO was flown in September 2012 onboard the High Altitude Student Payload (HASP) to test the behavior of the payload in flight. The HASP/LAGO balloon payload was launched from CSBF in Fort Sumner, NM with more than 8 hours above 30 km (110,000 ft). The US Precision Lightning Network (USPLN) Unidata Program recorded 128 lightning strikes within a 50 mile radius of the payload. Of these lightning strikes, there was one IC strike of undetermined polarity 45 miles away from the payload. All the remaining strikes recorded within a 50 mile radius of the payload path were negative polarity CG lightning discharges.

In Fig. 7.2, the averaged high energy (dynode) and low energy (anode) count rates per sec are plotted against the payload altitude. The count rate reflects the data rate due to background events during the flight. The launch is indicated by the vertical line on the left and is also reflected in the initial dip in the low energy background rate. The rate increases on the high and low energy channels as the balloon payload passes the Pfotzer maximum (~60000 ft, 18 km) and decreases as the payload approaches float altitude above 110000 ft (30 km) [Bazilevskaya and Svirzhevskaya, 1998]. The gradual decrease in the high energy and low energy count rate at float altitude seen in Fig 7.2 may be due to changing temperature or to the loss of optical grease between the PMT and the acrylic light guide during flight. After the 2012 engineering flight, the remaining optical grease was removed to prevent future problems. Post-flight testing of LAGO confirmed that all components of the payload still operate as designed.

Data were accumulated for the entire flight and transmitted via the internet to LSU for post-flight analysis. The analysis software selects events with signals corresponding to at least 200 keV deposited energy per channel within 1 μsec. Anode signals above this energy seen on only one PMT are discarded as noise. The data are then binned into 2 msec bins and assigned a timestamp in the center of the bin. The significance of each 2 msec bin is calculated as the number of statistical standard deviations above the average rate at float. The frequency of each significance level is plotted against the significance level sigma in Fig. 7.3 (solid line). The distribution plotted shows an exponentially decreasing number of counts per sigma bin with increasing sigma. A significance of 10 σ corresponds to 24 counts in 2 msec. No 2 msec bins were detected above the background distribution at float altitude, indicating that no gamma flashes were observed on this

flight. This is expected since the payload remained tens of miles away from the nearest thunderstorm. For comparison, the expected normal distribution is also plotted (dashed line), showing an extra cosmic ray shower component above the expected background. Although no events were detected, the engineering flight of the LAGO payload in September of 2012 was deemed successful.
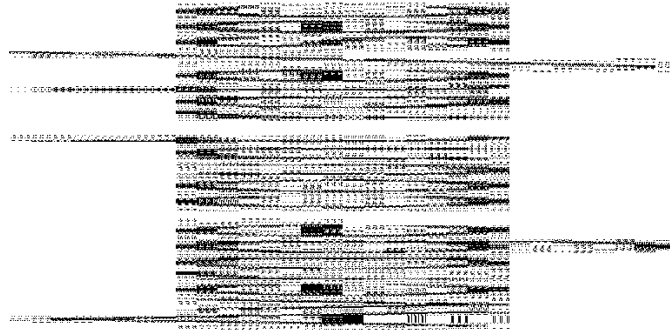
Figure 7.2 Averaged energy channel count rates per sec vs payload altitude during the 2012 flight. The solid line indicates the averaged anode (low energy) channel counts per sec. The dashed line indicates the averaged dynode (high energy) channel counts per sec. The vertical line at left indicates the payload launch time.
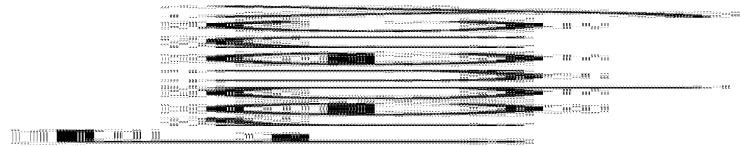
Figure 7.3 Frequency of the number of statistical standard deviations above the mean at float altitude (~110,000 ft) using 2 msec bins (solid line). The expected background distribution is also shown (dashed line), indicating an extra cosmic ray shower component. No 2 msec bins were detected above the background during the 2012 engineering flight

CHAPTER 8 – FUTURE PLANS: TETRA II

TETRA has produced a substantial list of TGFs observed from the ground, although with several limitations. The spectra of TETRA's events are restricted to 50 keV - 2 MeV by the thinness and density of its NaI scintillator plates. The source height of these TGFs was not determined. The current array cannot correlate events with TGFs seen by satellite instruments since it is located outside of their orbits. The frequency of detection is also limited by the modest lightning frequency in the local area. To address these limitations and provide capabilities for science beyond TETRA, we propose to build an upgraded version of the array, TETRA II. TETRA II will provide the opportunity to perform more detailed analyses of TGFs observed from the ground, correlate with TGFs observed from space, and begin to understand the storms that produce them.

The individual spectra of the TGFs observed with TETRA consist on average of ~20 photons with an average energy ~500 keV. In contrast, the spectral comparison performed in chapter 4 (Fig 4.5) used over 200 photons in the TGF portion alone to differentiate between the total background spectra and the TGF spectra. In order to perform spectral analysis of individual TGFs, we have designed TETRA II with a factor of 5 increase in sensitivity at 500 keV, resulting in at least 100 photons per TGF. By increasing the sensitivity with a denser, higher Z, and thicker detector element, TETRA II's energy range is extended up to several MeV or higher, where the more interesting portion of the TGF energy spectrum lies. One important result of TETRA II will be the detection of photons above 7 MeV -- the characteristic RREA energy scale -- providing confirmation of RREA photons in each event. The higher energy range will also allow discrimination between the TGF spectra observed and the spectrum of x-rays produced by lightning [Dwyer et al., 2012c]. With denser and thicker detectors, TETRA II will also be able to see TGFs from larger distances, thus increasing the rate and significance of detections. In addition to upgraded detectors, particle scintillators will also be added to study the particle component of TGFs from the ground. TETRA II will also be used to study longer duration events such as those described by Tsuchiya et al. (2013).

Fermi detections of TGFs in the Caribbean are greater than all other areas combined (see Fig. 2.4) [Briggs et al., 2013]. TETRA II will be located within the orbit of Fermi in the Caribbean to take advantage of these TGFs. Current prospects for a site include the northwestern tip of Puerto Rico or in the southern portion of central Jamaica. Both of these locations have annual lightning frequencies greater than TETRA's current local area (see Fig. 2.3). TETRA II's location will increase the frequency of TGF detections from the ground and provide opportunities to correlate ground observations of TGFs with satellite observations by Fermi. Fermi scientists have expressed interest in encouraging such correlations. Fermi's TGF data are publicly available at http://gammaray.nsstc.nasa.gov/gbm/science/tgf/.

TETRA II will also include on-site weather stations to further analyze the storms that produce TGFs. These stations will report lightning nearby via radio frequency sensors, electric field measurements, relative humidity and temperature measurements among others. Lightning sensor measurements will provide the latitude, longitude, height,

current, polarity and other properties of the lightning detected. Local radar observations, such as cloud density and height, will also be used to track the progression and other properties of local storms. These detailed measurements will enable the TETRA II team to perform individual and trend analyses of TGF storms to a greater depth than that reported in chapter 6.

TGFs detected from space are produced at altitudes ~10-15 km. However, TGFs observed with the Thunderstorm Energetic Radiation Array (TERA) at Camp Blanding, FL, have significantly lower altitudes, creating a disparity in altitudes between TGFs detected by satellites and those observed by ground-based arrays [Dwyer et al., 2012c]. TETRA II will initially have 10 detection boxes spaced over approximately a square kilometer, thus increasing the probability that a given TGF will be detected on more than one box. When TGFs are detected by three or more detection boxes, TETRA II will have the capability to determine the source height of the TGF. This independent calculation of the TGF source altitude will allow for comparison with the calculated lightning altitude. Given a source altitude of 2 km and a beaming half-angle of 30° as seen from space, the maximum radius from the center of the TGF for detection is ~1.2 km. If a TGF produced at 2 km happens to be centered on the array, then TETRA II will be able to see the event on *all* of the detection boxes in the array. More detection boxes will be added to TETRA II in future years.

The goal of TETRA II is to detect more TGFs with more photons per TGF with a reliable, proven system, such as TETRA. Therefore, only minor changes to TETRA's electronics and data acquisition software will be made. We have obtained permission to use the BGO crystals from the Advanced Thin Ionization Calorimeter (ATIC) balloon-borne cosmic ray detector [Chang et al., 2008] to upgrade the detectors. Each detection box in the TETRA II array will contain 6 1″ x 1″ x 10″ BGO scintillator crystals, each viewed individually by 1.5″ PMTs on each end. These BGO crystals will be arranged in a 3 x 2 array (3 across and 2 deep) to increase sensitivity to photons above 7 MeV -- the characteristic RREA energy scale. Just as in TETRA, a blank PMT will be included in each detection box to monitor for electronic noise. One to two plastic scintillators will be placed above each BGO array to discriminate between photons and particles in each TGF. These plastic scintillators will be viewed on each end by a PMT. In addition to on-site weather stations, a relatively inexpensive low frequency lightning detector array will be implemented to record CG and IC lightning locations and altitudes. Nearby existing VLF (very low frequency) lightning detection arrays will be used to provide lightning polarity information and lightning strike location comparisons.

The TETRA data acquisition system will be upgraded for TETRA II, partly to eliminate the timing issues that have been seen with TETRA. Also, given the greater sensitivity of TETRA II, we expect the new event data rate to be five times that of the rate seen on TETRA. With an estimated deadtime of 26 μsec, TETRA can detect a maximum of 42 timestamps per millisecond (or a burst rate of 42 kHz). One primary goal of the redesign is to increase the burst rate limit to above 50 timestamps/msec, resulting in more detectable counts per millisecond. This will be done partly by streamlining the hardware and data acquisition software to remove extra dead-time. Another way to accomplish this

is to minimize the number of channels read per event and rearrange the data channels on the stack. In other words, the number of channels allowed per stack will be limited and the data recording process will be altered to read only data channels with signals above a threshold and triggered within a small time window. The effect of the number of channels, the arrangement of the channels, the threshold level and the size of the triggering time window will be analyzed to determine values that produce the highest possible burst rates. The daily transfer and analysis of data from TETRA II as described in chapter 4 will remain automated, requiring a wireless or Ethernet network on site.

Table 8.1 Comparison of TETRA and TETRA II Properties

TETRA	TETRA II
1/4" x 8" x 8" NaI(Tl)	1" x 1" x 10" BGO
0.05 to 2 MeV	0.05 to 10 MeV
20 photons/EC	More than 100 photons/EC
No plastic scintillators	1-2 plastic scintillators/box
4 Boxes	10 Boxes
No satellite correlation	Fermi satellite correlation
4-8 lightning strikes/sq.km./month at height of thunderstorm season	$\geq$ 16 lightning strikes/sq.km./month at height of thunderstorm season
No lightning detection onsite	Lightning detection onsite

Most of the changes to the electronics and the mechanical structure involve a simple rearrangement or replacement of minor components, better troubleshooting options and more stable signal and power connections. To reduce false triggers due to PMT noise, the current design of the PMT bases will be changed from a cap style base to a small circuit board. The repeated large temperature swings in the Baton Rouge area combined with the angular detector support system have caused PMTs to crack and the optical cement joints between the PMTs and the acrylic light guides to fail over time. By choosing TETRA II's location to be in the Caribbean, temperature swings are limited to less than 30°F over the entire year as compared to the more than 80°F swing in Baton Rouge. As an additional effort to prevent this problem, the PMTs will be cemented directly onto the BGO crystals.

In addition to the modified design for TETRA II, an updated data analysis package must be developed. The current data analysis package is built for a maximum of four boxes with five data channels per box and requires a significant portion of the event analysis to be done by hand (see Appendix C). This package must be upgraded to handle TETRA II's larger array, to allow more of the event analysis to be automated and to incorporate a partially automated version of the storm analysis presented in chapter 6.

TETRA II's automated daily analysis package will be able to handle about ten data channels per stack with an indefinite number of detection boxes. Coincident signals above a threshold will be required on PMTs viewing the same scintillator to reduce noise. More than one operating BGO PMT set will be required to trigger in each TGF candidate to further reduce PMT noise such as that described in chapter 5. VLF and VHF lightning information will also be included in the daily reports. A software package will also be developed to automatically monitor the performance of each PMT and track their calibrations. These automated software packages will be necessary to monitor the health of the approximately 120 PMTs that will be used in TETRA II.

Once the basic software is upgraded, other deeper issues can be addressed. As described above, several TGFs should be detected on multiple boxes in TETRA II, allowing the TGF source height to be calculated. The software to perform this calculation must be written, tested and incorporated into the event analysis package. The development of storm tracking software will be also useful in monitoring the properties of the storm before, during and after it tracks across the array, including reporting the specific conditions across the array immediately surrounding TGF detection. This new software will assist in correlating storm characteristics with TGF production in greater detail and for a larger sample of storms than that described in chapter 6. A Monte Carlo package should also be developed to perform basic model calculations of the TGF properties detected with TETRA II. These calculations should include detector response simulations (including dead-time analysis), electron and particle flux calculation for each TGF detected, and avalanche properties. A separate software package will also be developed to search for longer duration enhancements in various energy ranges, such as those reported in Tsuchiya et al. [2013].

The goal of TETRA II is to provide a more reliable, sensitive and rugged TGF detector array with capabilities for science that do not yet exist. The most efficient way to accomplish this is to use an upgraded version of the ground based TETRA TGF array that has resulted in published relevant results with proven reliability. TETRA II is planned for installation in May-June 2015, with full operation scheduled for July 2015 in time for the peak of the 2015 thunderstorm season.

CHAPTER 9 – CONCLUSION

Here we have presented data for 28 gamma ray events observed from July 2010 to October 2013 with a self-triggered ground array, suitable for observing weak events from nearby distances without a bias caused by a lightning trigger. We find that events with durations < 5 msec and detected individual photon energies up to at least 2 MeV appear to be produced in conjunction with nearby negative polarity cloud-to-ground (-CG) lightning. In two CECs, these are most closely associated with -CG lightning 1.4 and 1.8 miles away. In the other CEC event, the nearest detected lightning strike in time is more than 6 seconds after the gamma ray event. Either this gamma ray event is not correlated with nearby lightning, the associated CG lightning strike was missed by the lightning network, or the event was due to intracloud (IC) lightning that was not detected by the lightning network.

The gamma ray events described here have durations ranging from 24 μsec to 4.2 msec. The similarity of these event durations observed by TETRA to those reported by BATSE, RHESSI, AGILE, Fermi, and ICLRT suggest that the TETRA events are also generated by the RREA mechanism. Dwyer et al. (2012c) compared the spectrum of x-rays from lightning to gamma rays from TGFs, showing a marked difference above 2 MeV, but the restricted energy range of TETRA and the low statistics make it impossible to draw strong conclusions from the observed TETRA spectra.

The events reported here were occurred within seven seconds of lightning detected by the USPLN within 5 miles of TETRA. Since the USPLN is a VLF lightning detection array, the majority of these flashes are cloud-to-ground lightning flashes. Ten of the TGFs detected by TETRA were detected within ±100 milliseconds of lightning within 5 miles. Thus, the association rate of the ten lightning-associated TETRA TGFs with all lightning detected by the USPLN within 5 miles of TETRA (8188 flashes) is approximately 1.2×10^{-3}. If an approximate CG to total lightning (IC + CG) ratio of 1:4 is used [Boccippio et al., 2001], then the lightning associated TETRA TGF to total lightning ratio becomes 4.9×10^{-4}. This value is comparable to the ratio reported by Fermi for the Americas [Briggs et al., 2013]. However, if the total number of TGFs observed by TETRA are considered, then the ratio of TETRA TGFs to CG lightning becomes 3.4×10^{-3}, resulting in a TGF to total lightning ratio of 1.4×10^{-2}. This ratio is much greater than the ratio reported by Fermi for Northern and Central Americas. This difference could be caused by the differing lightning detection arrays used for reference, differing TGF production altitudes and fluxes, and the different detector sensitivities and limitations. It is also possible that TGF production rates vary with altitude, resulting in detection rates that vary with location.

Ten of the 23 TGFs detected by TETRA with good timing were associated with negative polarity CG lightning flashes within ±100 msec, resulting in an TGF association rate of approximately 43%. Since lightning associations were not possible for five of TETRA's TGFs due to network timing difficulties, these five were not counted in the calculation above. If the time constraint is reduced to ±6 msec, the association rate becomes 39%. TETRA TGF-lightning associations closer than 1 msec were not possible due to the

timing accuracy of the lightning data. For comparison, the rate of Fermi TGF association with World Wide Lightning Location Network (WWLLN) detected lightning flashes (+IC) within 200 µsec is 30% for 601 TGFs [Connaughton et al., 2013]. Although these association rates are similar, caution should be used when comparing the two rates due to the small sample size of TETRA TGFs, the differing time constraints on the matches, and the differing lightning detection arrays used in each study.

Fermi GBM data also suggest that WWLLN detects shorter duration TGF sferics more efficiently than the longer ones because of the frequency constraints of the network (between 6 and 18 kHz). For the sferic signals found within a 400 µs window around the TGF gammas, the stronger sferics appear due to the TGF itself while the weaker sferics are due to associated +IC lightning [Connaughton et al., 2013].

The brightest TGFs seen by BATSE, RHESSI, and GBM produce $~10^{17}$ runaway electrons with a source altitude ~13 km [Briggs et al., 2010]. In contrast, the two TGFs previously reported from the ground by ICLRT are associated with -CG lightning [Dwyer et al., 2004, 2012c]. The 2009 ICLRT event produced $~10^{11}$ runaway electrons and was observed at a distance of ~2 km. If the TETRA events are characterized by typical energy 500 keV and distance 1 mile, then atmospheric absorption attenuates the flux by a factor of $~4 \times 10^{-8}$ at sea level. Assuming isotropic emission at a distance of 1 mile, a typical total of 20 photons observed in an event by TETRA then requires in excess of $~10^{18}$ photons at the source. Based on these calculations, either the ground level TETRA events are beamed, or they are distinctly different from the ICLRT events.

This study also reports a 79% correlation of TETRA TGFs with cloud formations showing decreasing altitude. Due to the small sample size, this rate does not strictly classify TGFs observed from the ground as indicators of decreasing storm strength. However, this high association rate does warrant further study into the possible mechanisms linking TGFs to collapsing clouds. It may also be possible to extend this study using Fermi TGFs. Although the majority of TGFs detected from space have position uncertainties near 300 km – much too large to associate with a specific portion of a thunderstorm – the positions of TGFs associated within 200 µsec of lightning are known to within 10 km. From this subset of Fermi TGFs, the events detected within range of local radar stations can be analyzed in a manner similar that presented in chapter 6 and compared to the results presented here.

Based on the results presented in this document, an upgraded version of TETRA is currently under construction. TETRA II will have 60 thicker, denser scintillators to increase the upper energy detection limit to a few MeV or more and to increase detector sensitivity by a factor of 5. These scintillators will be evenly distributed into 10 detection boxes covering a square kilometer in the Caribbean. Local VLF lightning detection arrays will be used to correlate the detected gamma-ray bursts with lightning. Local radar data will also be used to analyze the storms producing TGFs detected by TETRA II. Associations of these TGFs detected from the ground with those detected by Fermi from space will also be possible for the first time. The initial deployment of TETRA II will occur in the summer of 2015.

BIBLIOGRAPHY

Ackerman, S. A. and J. A. Knox (2007), Meteorology: Understanding the Atmosphere. *Thomson Higher Education,* University of California.

Amburn, S. A., and P. L. Wolf (1997), VIL Density as a hail indicator. *Weather and Forecasting* **12**, 473.

Andra, D., V. Preston, E. Quetone, D. Sharp, and P. Spoden (1994), An operational guide to configuring a WSR-88D principal user processor. *Operations Training Branch, Operational Support Facility.*

Bazilevskaya, G. A., and A. K. Svirzhevskaya (1998), On the stratospheric measurements of cosmic rays. *Space Sci. Rev.* **85**, 3-4, 431-521.

Boccippio, D. J., K. L. Cummins, H. J. Christian, and Goodman, S. J. (2001), Combined satellite- and surface-based estimation of the intracloud-cloud-to-ground lightning ratio over the continental United States. *Mon. Wea. Rev.* **129**, 108.

Briggs, M. S., *et al.* (2010), First results on terrestrial gamma ray flashes from the Fermi Gamma-ray Burst Monitor. *J. Geophys. Res.* **115**, A07323.

Briggs, M. S., *et al.* (2011), Electron-positron beams from terrestrial lightning observed with Fermi GBM. *Geophys. Res. Lett.* **38**, L02808.

Briggs, M.S., *et al.* (2013), Terrestrial Gamma ray Flashes in the Fermi Era: Improved Observations and Analysis Methods. *J. Geophys. Res. Space Physics* **118**.

Carey, L. D., M. J. Murphy, T. L. McCormick, and N. W. S. Demetriades (2005), Lightning location relative to storm structure in a leading-line, trailing stratiform mesoscale convective system. *J. Geophys. Res.* **110**, D03105.

Celestin, S., W. Xu, and V. P. Pasko (2012), Terrestrial gamma ray flashes with energies up to 100 MeV produced by nonequilibrium acceleration of electrons in lightning. *J. Geophys. Res.* **117**, A05315.

Chang, J., *et al.* (2008), An excess of cosmic ray electrons at energies of 300-800 GeV. *Nature* **456**, 362.

Chilingarian, A., *et al.* (2010), Ground-based observations of thunderstorm-correlated fluxes of high-energy electrons, gamma rays, and neutrons. *Phys Rev D* **82**, 043009.

Chilingarian, A., G. Hovsepyan, and A. Hovhannisyan (2011), Particle bursts from thunderclouds: Natural particle accelerators above our heads. *Phys Rev D* **83**, 062001.

Cohen, M. B., *et al.* (2010), A lightning discharge producing a beam of relativistic electrons into space. *Geophys. Res. Lett.* **37**, L18806.

Cohen, M. B., U. S. Inan, and G. Fishman (2006), Terrestrial gamma ray flashes observed aboard the Compton Gamma Ray Observatory/Burst and Transient Source Experiment and ELF/VLF radio atmospherics, J. Geophys. Res. 111, D24109.

Connaughton, V., *et al.* (2013), Radio signals from electron beams in Terrestrial Gamma ray Flashes. *J. Geophys. Res.* **118,** 2313-2320.

Cummer, S. A., *et al.* (2011), The lightning-TGF relationship on microsecond timescales. *Geophys. Res. Lett.* **38**, L14810.

Dwyer, J. R. (2003), A fundamental limit on electric fields in air. *Geophys. Res. Lett.* **30**, 20, 2055.

Dwyer, J. R., *et al.* (2004), A ground level gamma ray burst observed in associated with rocket-triggered lightning. *Geophys. Res. Lett.* **31**, L05119.

Dwyer, J. R. and D. M. Smith (2005), A comparison between Monte Carlo simulations of runaway breakdown and terrestrial gamma ray flash observations. *Geophys. Res. Lett.* **32**, L22804.

Dwyer, J. R. (2008), Source mechanisms of terrestrial gamma ray flashes. *J. Geophys. Res.* **113**, D10103.

Dwyer, J. R., *et al.* (2010), Estimation of the fluence of high-energy electron bursts produced by thunderclouds and the resulting radiation doses received in aircraft. *J. Geophys. Res.* **115**, D09206.

Dwyer, J. R. (2012a), The relativistic feedback discharge model of terrestrial gamma ray flashes, *J. Geophys. Res*. **117**, A02308.

Dwyer, J. R., D. M. Smith, and S. A. Cummer (2012b), High-energy atmospheric physics: Terrestrial gamma-ray flashes and related phenomena. *Space Sci. Rev.* **173**, 133.

Dwyer, J. R., *et al.* (2012c), Observation of a gamma ray flash at ground level in association with a cloud-to-ground lightning return stroke. *J. Geophys. Res.* **117**, A10303.

Ellison, B., *et al.* (2006), The Louisiana ACES student-built Balloon-Sat program, *Adv. in Space Res.* **38**, 2253.

Fishman, G.J., *et al.* (1994), Discovery of intense gamma ray flashes of atmospheric origin. *Science* **264**, 5163, pp. 1313-1316.

Fishman, G. J., *et al.* (2011), Temporal properties of the terrestrial gamma-ray flashes from the Gamma-ray Burst Monitor on the Fermi Observatory. *J. Geophys. Res.* **116**, A07304.

Fuschino, F., *et al.* (2011), High spatial resolution correlation of AGILE TGFs and global lightning activity above the equatorial belt. *Geophys. Res. Lett.* **38**, L14806.

Gjesteland, T., N. Østgaard, P. H. Connell, J. Stadsnes and G. J. Fishman (2010), Effects of dead time losses on terrestrial gamma ray flash measurements with the Burst and Transient Source Experiment. *J. Geophys. Res.* **115**, A00E21.

Gjesteland, T., *et al.* (2011), Confining the angular distribution of terrestrial gamma ray flash emission. *J. Geophys. Res.* **116**, A11313.

Gjesteland, T., *et al.* (2012), A new method reveals more TGFs in the RHESSI data. *Geophys. Res. Lett.* **39**, L05102.

Grefenstette, B.W., D.M. Smith, J.R. Dwyer, and G.J. Fishman (2008), Time evolution of terrestrial gamma ray flashes. *Geophys. Res. Lett.* **35**, L06802.

Grefenstette, B. W., D. M. Smith, B. J. Hazelton and L. I. Lopez (2009), First RHESSI terrestrial gamma ray flash catalog. *J. Geophys. Res.* **114**, A02314.

Grove, J. E. *et al.* (October 2012), A four-year survey of terrestrial gamma-ray flashes (TGFs) with Fermi LAT. Paper presented at the 2012 Fermi Symposium, Fermi Gamma-Ray Telescope, Monterey, CA (http://fermi.gsfc.nasa.gov/science/mtgs/symposia/2012/ program/c2/EGrove.pdf).

Gurevich, A. V. (1961), On the theory of runaway electrons. *Sov. Phys. JETP*, Engl. Transl., **12**(5), 904–912.

Gurevich, A.V., G.M. Milikh, and R. Roussel-Dupre (1992), Runaway electron mechanism of air breakdown and preconditioning during a thunderstorm. *Phys. Rev. Lett.* **165**, 463.

Hager, W. W., *et al.* (2010), Three-dimensional charge structure of a mountain thunderstorm. *J. Geophys. Res.* **115**, D12119.

Hazelton, B. J., *et al.* (2009), Spectral dependence of terrestrial gamma ray flashes on source distance. *Geophys. Res. Lett.* **36**, L01108.

Inan, U. S., M. B. Cohen, R. K. Said, D. M. Said and L. I. Lopez (2006), Terrestrial gamma ray flashes and lightning discharges. *Geophys. Res. Lett.* **33**, L18802.

Jacques, A.A., J.P. Koerner, and T.R. Boucher (2011), Comparison of the United States Precision Lightning Network (USPLN) and the Cloud-to-Ground Lightning Surveillance System (CGLSS-II). Proc. 91st American Meteorological Society Annual Meeting, https://ams.confex.com/ams/91Annual/webprogram/Paper185527.html.

Lu, G., *et al.* (2011), Characteristics of broadband lightning emissions associated with terrestrial gamma ray flashes. *J. Geophys. Res.* **116**, A03316.

MacGorman, D. R., *et al*. (2005), The electrical structure of two supercell storms during STEPS. *Monthly Weather Review* **133**, 2583.

Marisaldi, M., *et al.* (2010), Gamma-ray localization of terrestrial gamma-ray flashes. *Phys. Rev. Lett.* **105**, 128501.

Marisaldi, M., *et al.* (2011), AGILE observations of terrestrial gamma-ray flashes. *Nuovo Cimento,* **C034N3**, 279-284.

Marshall, T. C., M. P. McCarthy and W. D. Rust (1995), Electric field magnitudes and lightning initiation in thunderstorms. *J. Geophys. Res.* **100**, D4, 7097.

Metzger, E., and W. A. Nuss (2013), The relationship between total lightning behavior and radar-derived thunderstorm structure. *Weather and Forecasting* **28**, 237.

Moore, C. B., K. B. Eack, G. D. Aulich and W. Rison (2001), Energetic radiation associated with lightning stepped-leaders. *Geophys. Res. Lett.* **28**, 11, 2141.

National Weather Service, "High Resolution Full Climatology Annual Flash Rate." Accessed March 31, 2014, http://www.srh.noaa.gov/jetstream/lightning/hirez_72dpi.htm.

National Weather Service, "Life Cycle of a Thunderstorm." Accessed March 31, 2014, http://www.srh.weather.gov/jetstream/tstorms/life.htm.

Østgaard, N., T. Gjesteland, J. Stadsnes, P. H. Connell, and B. Carlson (2008), Production altitude and time delays of the terrestrial gamma flashes: Revisiting the Burst and Transient Source Experiment spectra. *J. Geophys. Res*. **113**, A02307.

Østgaard, N. T., T. Gjesteland, R. S. Hansen, A. B. Collier, and B. Carlson (2012), The true fluence distribution of terrestrial gamma flashes at satellite altitude. *J. Geophys. Res*. **117**, A03327.

Rakov, V. A. and M. A. Uman (2003), Lightning Physics and Effects. Cambridge Univ. Press, Cambridge, U. K.

Ringuette, R., *et al*, (2013), TETRA observation of gamma-rays at ground level associated with nearby thunderstorms. *J. Geophys. Res. Space Physics* **118**, 7841.

Rodger, C. J., J. B. Brundell, R. H. Holzworth and E. H. Lay (2009), Growing Detection Efficiency of the World Wide Lightning Location Network. *Am. Inst. Phys. Conf. Proc., Coupling of thunderstorms and lightning discharges to near-Earth space: Proceedings of the Workshop* **1118**, 15-20.

Schultz, C. J., W. A. Peterson, and L. D. Carey (2011), Lightning and severe weather: A comparison between total and cloud-to-ground lightning trends. *Weather and Forecasting* **26**, 744.

Shao, X-M., T. Hamlin and D.M. Smith (2010), A closer examination of terrestrial gamma-ray flash-related lightning processes. *J. Geophys. Res*. **115**, A00E30.

Smith, D. M., *et al.* (2005), Terrestrial gamma-ray flashes observed up to 20 MeV. *Science* **307**.

Smith, D.M. et al. (2010), Terrestrial gamma ray flashes correlated to storm phase and tropopause height. *J. Geophys. Res*. **115**, A00E49.

Smith, D. M., *et al.* (2011), A terrestrial gamma ray flash observed from an aircraft. *J. Geophys. Res.* **116**, D20124.

Stanley, M. A., *et al.* (2006), A link between terrestrial gamma ray flashes and intracloud lightning discharges. *Geophys. Res. Lett*. **33**, L06803.

Splitt, M. E., S. M. Lazarus, D. Barnes, *et al.* (2010), Thunderstorm characteristics associated with RHESSI identified terrestrial gamma flashes. *J. Geophys. Res.* **11**, A00E38.

Steiger, S. M., R. E. Orville, and L. D. Carey (2007), Total lightning signatures of thunderstorm intensity over north Texas. Part 1: Supercells. *Monthly Weather Review* **135**, 3281.

Strader, S. M., W. S. Ashley, and G. D. Herbert (2013), A comparison and assessment of the USPLN and ENTLN. *93rd American Meteorology Society Annual Meeting, Austin, TX, Jan 9, 2013.*

Stumpf, G. J., A. Witt, E. D. Mitchell, *et al.* (1998), The National Severe Storms Laboratory Mesocyclone Detection Algorithm for the WSR-88D. *Weather and Forecasting* **13**, 304.

Tavani, M., *et al.* (2011), Terrestrial gamma ray flashes as powerful particle accelerators. *Phys. Rev. Lett.* **106**, 018501.

Tsuchiya, H., *et al.* (2011), Long-duration γ ray emission from 2007 and 2008 winter thunderstorms. *J. Geophys. Res.* **116**, D09113.

Tsuchiya, H., *et al.* (2013), Hardening and termination of long-duration γ rays detected prior to lightning. *Phys. Rev. Lett.* **111**, 015001.

Xu, W., S. Celestin, and V. P. Pasko (2012), Source altitudes of terrestrial gamma-ray flashes produced by lightning leaders. *Geophys. Res. Lett.* **38**, L08801.

Williams, E. R. (2010), The origin and context of C T R Wilson's ideas on electron runaway in thunderclouds. *J. Geophys. Res.* **115**, A00E50.

Wilson, C. T. R. (1925), The acceleration of beta-particles in strong electric fields such as those of thunder-clouds. *Proc. Cambridge Philos. Soc.* **22**, 534–538.

APPENDIX A – TETRA ELECTRONICS

As described in chapter 3, the electronics and the PC104 stack for TETRA are designed to internally trigger and record the time and voltage of each PMT signal above a set noise threshold level. A linear voltage divider is used in the PMT base (circuit pictured in Figure A.1). The same circuit is used for the LAGO PMT bases. For TETRA, the separate dynode eight signal (CH1 signal in Fig. A.1) is ignored.
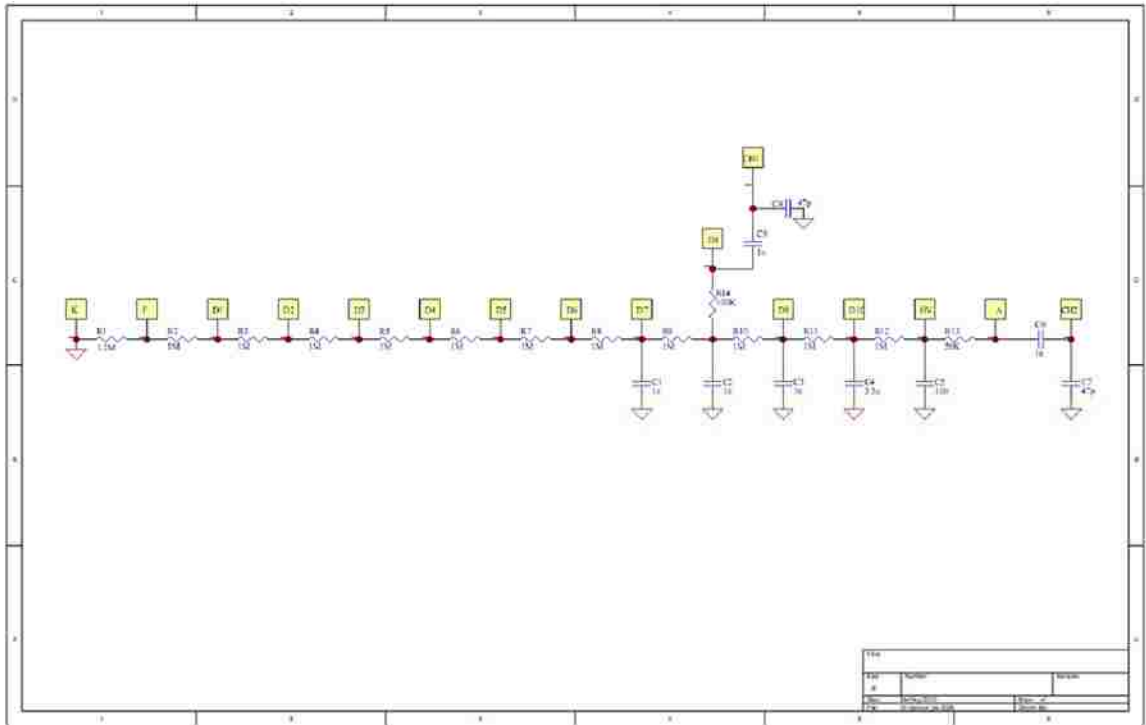
Figure A.1 Linear voltage divider used in TETRA PMT bases.

The signal generated by the PMT through the base circuit is sent to Front End Module (FEM). Figures A.2 and A.3 are the circuit diagrams of the FEM. If the voltage of the anode signal (CH2 in Fig. A.1) is above the threshold value (set at TP4), a trigger is sent via the 'DLo' output on the FEM board to the Trigger Logic Module (TLM) on the PC104 stack. (The high threshold circuit located at the bottom of Figure A.2 is not used for TETRA or LAGO.) The TLM then communicates this trigger to the FEM board (J5 to J10 in Fig. A.3). The FEM board lengthens the triggering signal and sends it to the ADC board to enable the ADC to record voltages. In order for the signal voltage from the PMT anodes to be recorded, the anode signal is inverted, the maximum voltage is held and delayed (top circuit in Fig. A.2). This final voltage is sent from the FEM to the ADC board on the stack and is recorded.

Once the signal from the TLM has been processed by FEM board, the PMT's maximum signal voltage is recorded by the 12-bit ADC board. When the energy of the PMT signal corresponds to an energy deposit of at least 50 keV, the signal is referred to as a count. In general, counts do not occur on more than one PMT within the signal integration time
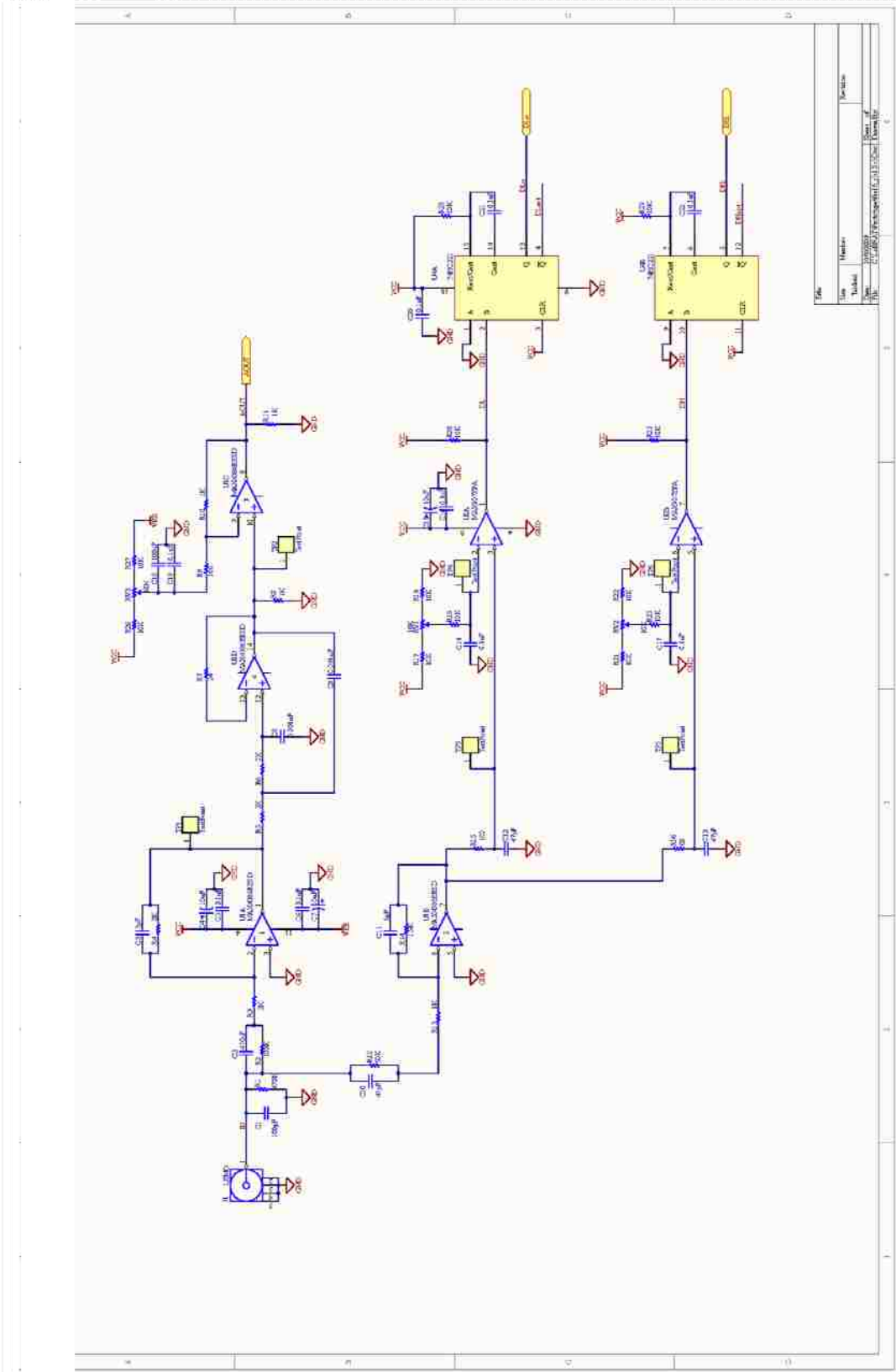
Figure A.2 Circuit diagram for one of the 16 signal channels on the FEM board.
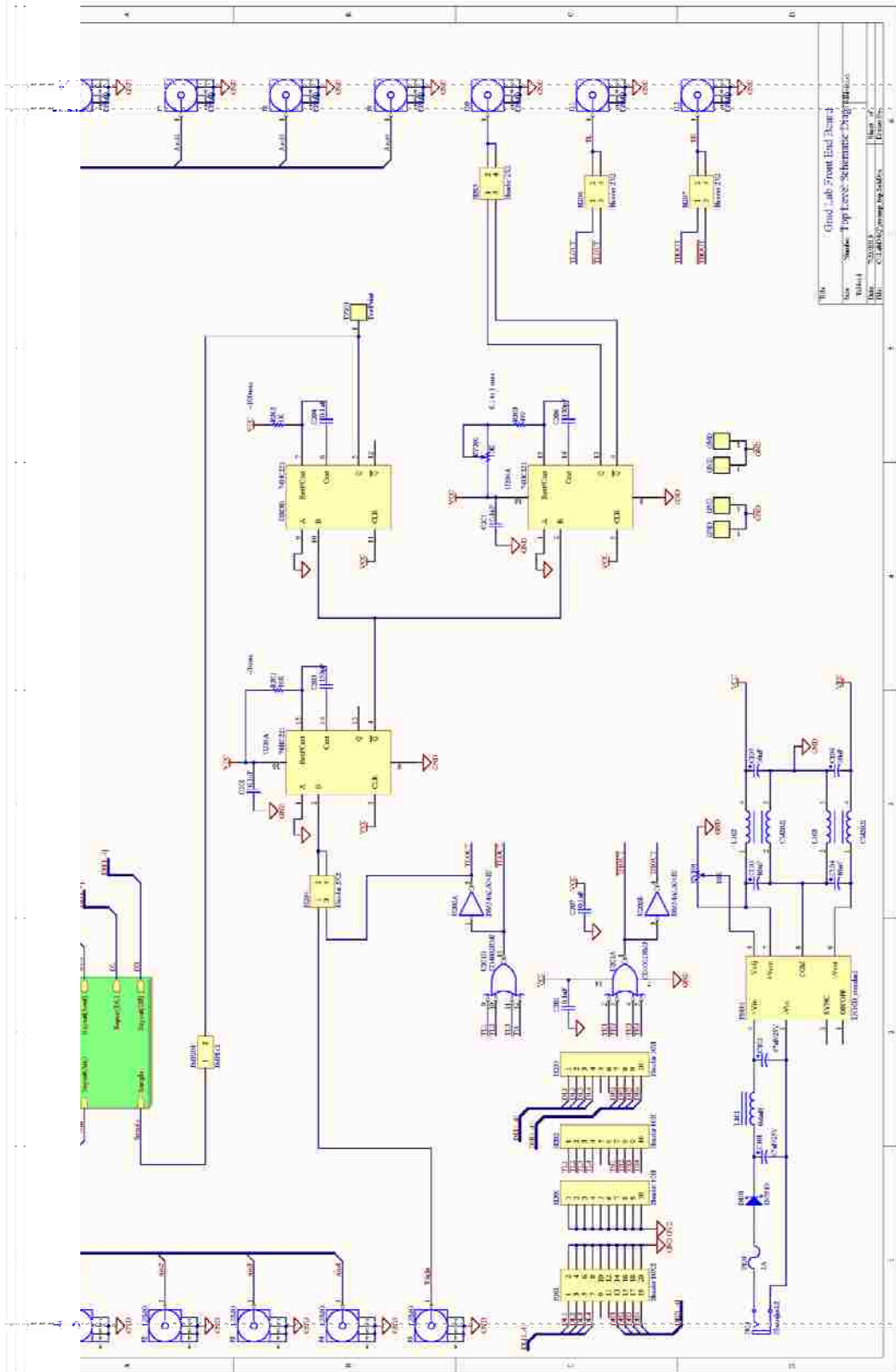
78

Figure A.3 Circuit diagram of the FEM board used for TETRA.

(a few μsec), resulting in a unique timestamp for each count. For each count, a record of the timestamp and the ADC value is recorded. The format of each data file is shown in Figure A.4. The file header contains various information such as the date, time and number of events in the file. Each individual event record contains the timestamp and the ADC value. For high-rate events such as the event candidates shown in chapters 4-6, signals above the threshold can be generated on more than one PMT. These additional ADC values are recorded in the same event record. The same data format is used for the LAGO data files.

The high voltage and low voltages required by TETRA are generated by the auxiliary board. The circuit and layout of the auxiliary board are given in Fig. A.5. Both the high voltage and the low voltage converters used on the TETRA auxiliary board require 12V and ground inputs. Three signal amplifier circuits are used to amplify the temperature sensor outputs by a factor of 2. The fourth amplifier circuit is used for the relative humidity sensor (x1 factor). These signals are recorded by the ADC board each time a trigger is processed. For TETRA, the P1_LEMO, P2_LEMO, P3_LEMO and P4_LEMO circuits in Figure A.5 are not used.

File Header

Date / Time (2-byte ints)

Year (2010)   Month (01)   Day (06)   Hour (13)   Minute (57)   Second (46)
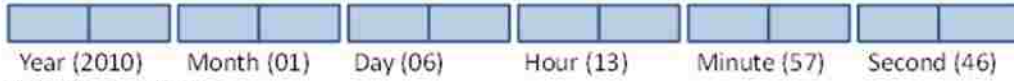
File Description

x 512

(string) 512 characters (ends with Null '\0')

Enabled Channels (Register)

Each byte represents on/off for channels -31

Total # Events in File
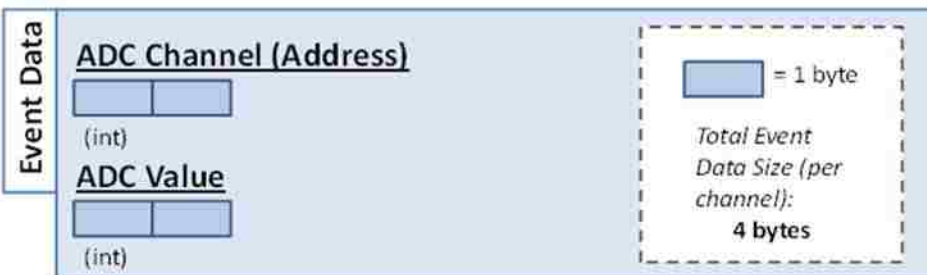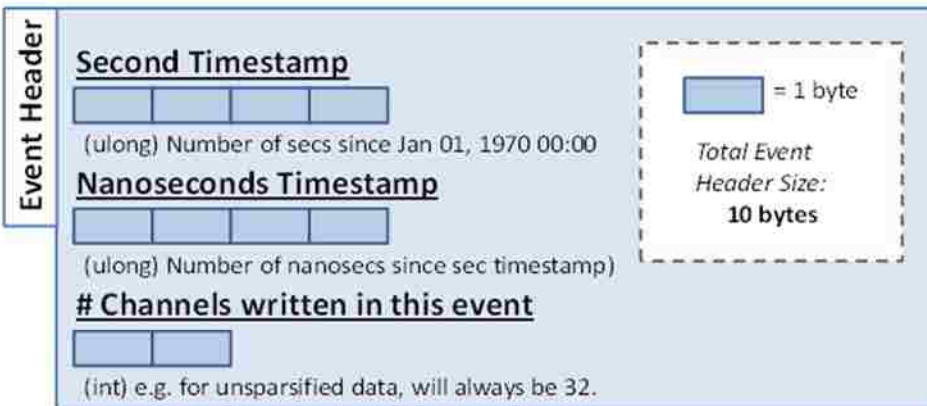
(ulong)

Total # Channel Written

(ulong) e.g. for un-sparsified file, should equal (total # events) x (total enabled channels)

Total Time (ms)

(ulong) should just be END time minus START time, NOT 'ACTIVE' TIME.

= 1 byte

Total File Header Size: 538 bytes

Event

Event Header

Second Timestamp

(ulong) Number of secs since Jan 01, 1970 00:00

Nanoseconds Timestamp

(ulong) Number of nanosecs since sec timestamp)

Channels written in this event

(int) e.g. for unsparsified data, will always be 32.

= 1 byte

Total Event Header Size: 10 bytes

Event Data

ADC Channel (Address)

(int)

ADC Value

(int)

= 1 byte

Total Event Data Size (per channel): 4 bytes

e.g. x 32

Figure A.4 File Structure of the TETRA and LAGO data files.
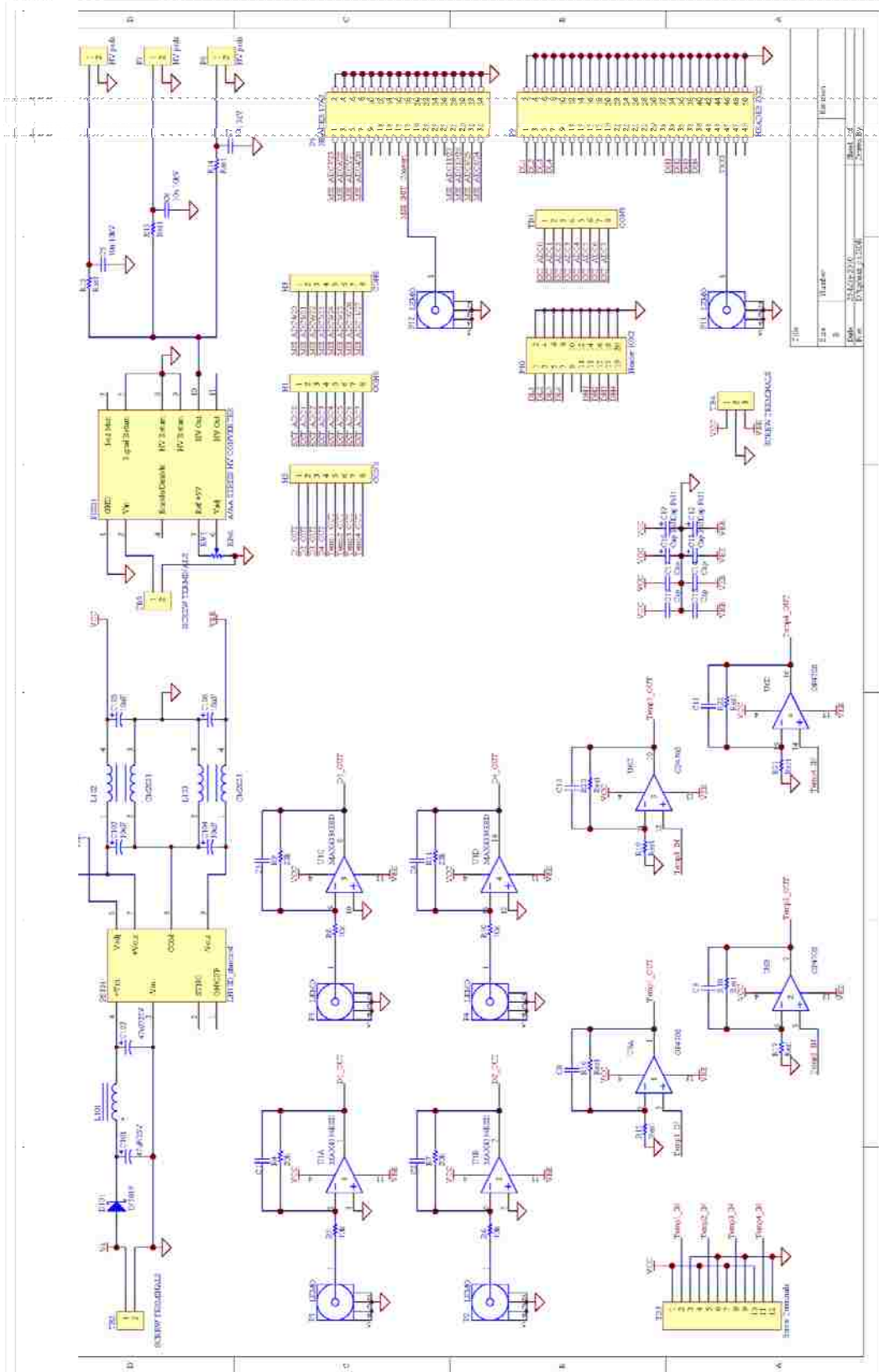
Figure A.5 Circuit diagram of TETRA's auxiliary board.

APPENDIX B – LAGO ELECTRONICS

As described in chapters 3 and 9, the electronics and the PC104 stack for LAGO are designed to internally trigger and record the time and voltage of each PMT signal above a set noise threshold level. The same linear voltage divider used in the TETRA PMT bases is also used in the LAGO PMT bases (circuit pictured in Figure A.1 in previous section). The CH1 signal is used to monitor higher energy pulses from the eighth dynode, before the final two stages of amplification. The CH2 signal is used to count lower energy pulses from the anode of the PMT. For LAGO, a circuit board was used for the PMT base circuit (pictured in Figure B.1).
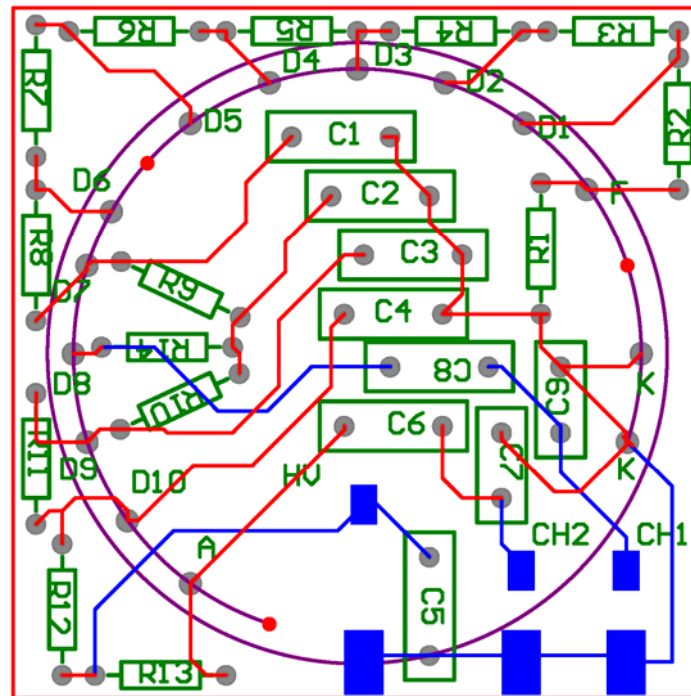
Figure B.1 Circuit layout of the linear voltage divider used in LAGO PMT bases.

The signal generated by the PMT through the base circuit is sent to Front End Module (FEM). Figures B.2 and B.3 are the circuit diagrams of the four-channel FEM used in LAGO. The PMT signals for LAGO are processed and stored in the same way as the PMT signals for TETRA. For LAGO, the timestamp is calculated with an internal clock rather than a GPS clock since only ±1msec timing accuracy is needed to match with lightning strikes detected by USPLN.

The circuitry shown in Figure B.2 is designed to shape and trigger off of a negative amplitude signal, such as that given by the PMT anodes. In LAGO, the positive amplitude signal from the eighth dynodes is also sent through this circuit, resulting in a signal correctly shaped for the ADC, but with a negative amplitude. Since the ADC and TLM require positive amplitude signals to trigger and assign an ADC value, a different wiring scheme was used (pictured in Figure B.4). Signals from FEM channels with a
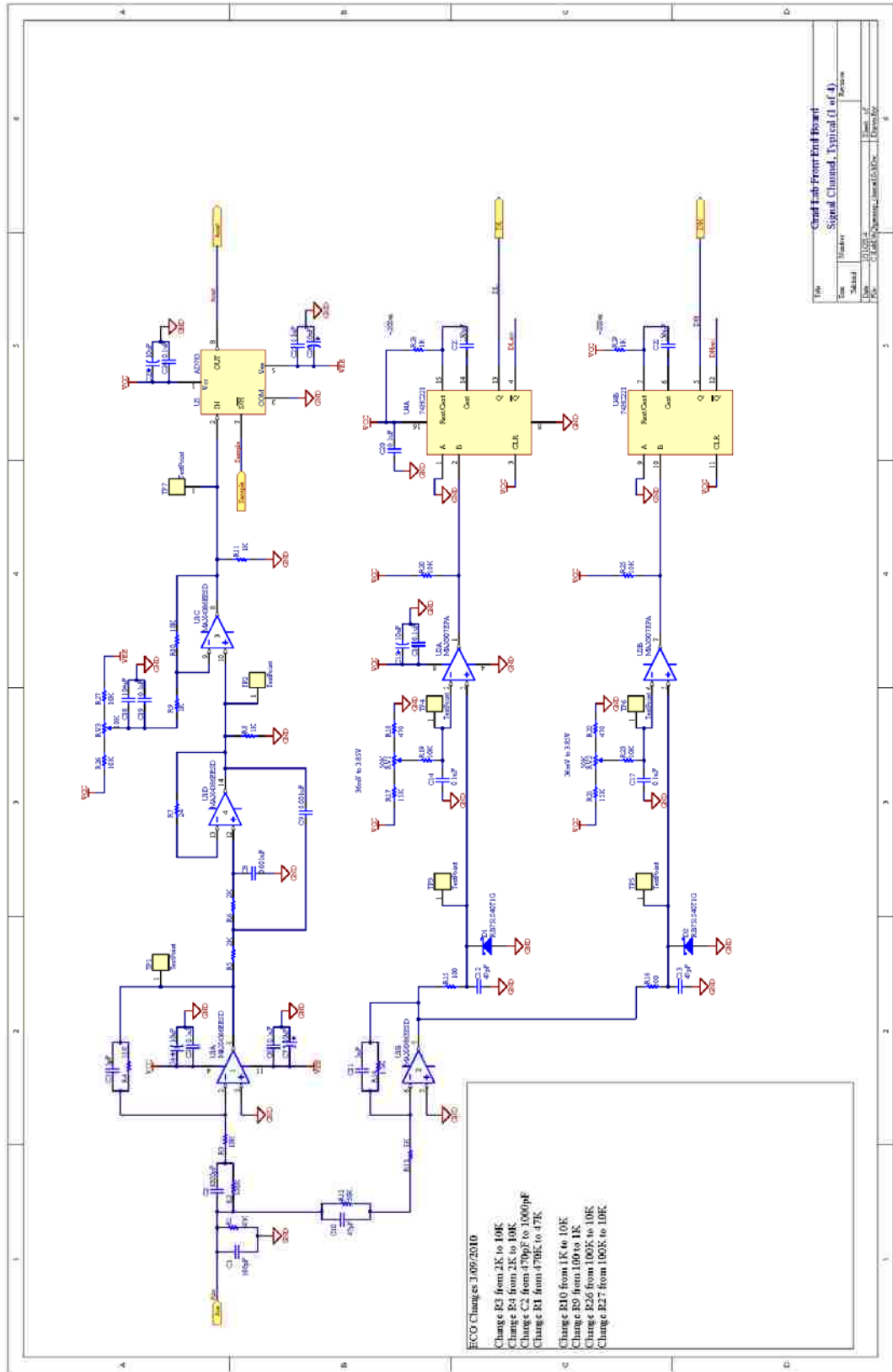
Figure B.2 Circuit diagram for one of the 4 signal channels on the FEM board.
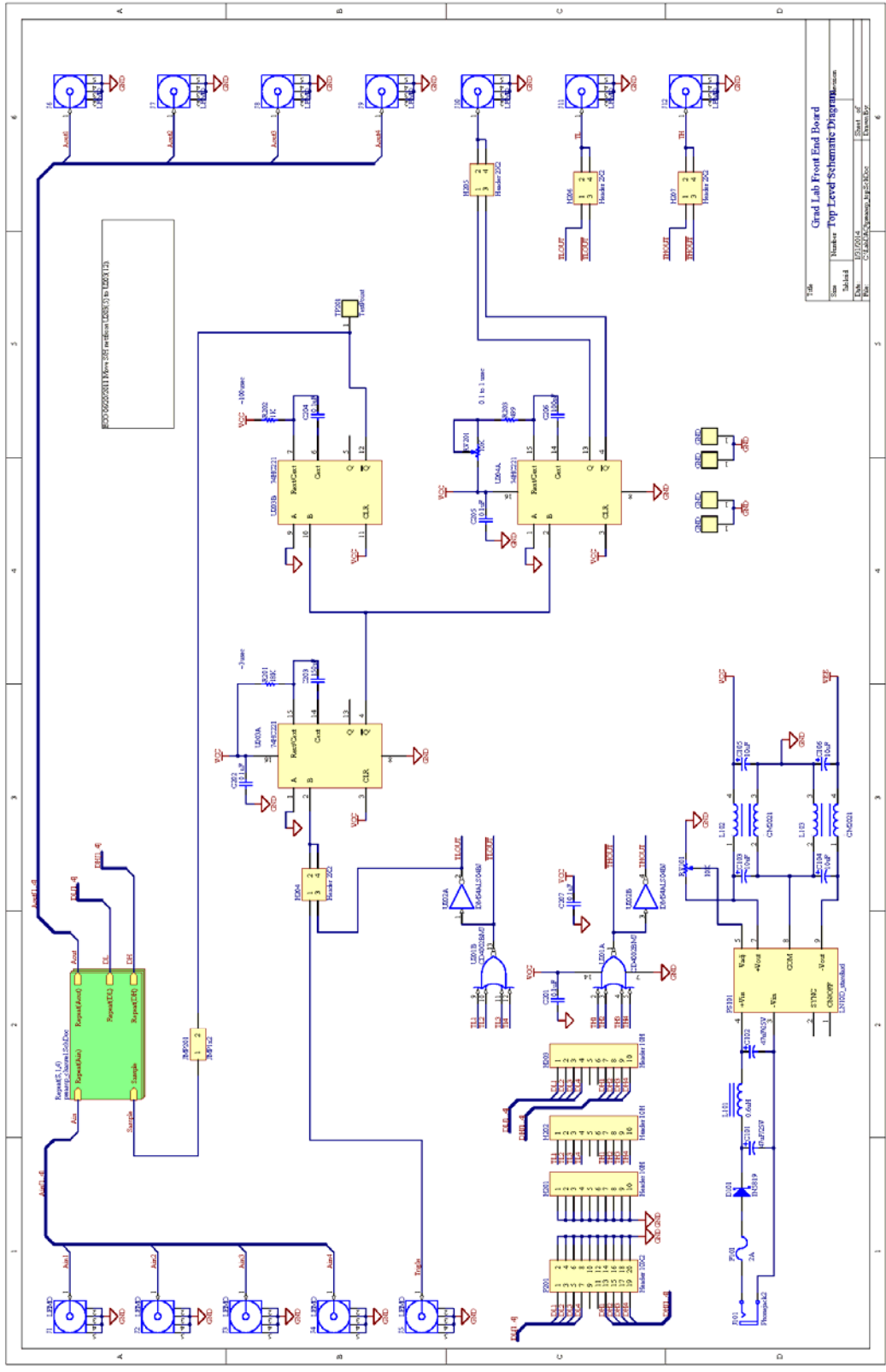
Figure B.3 Circuit diagram of the FEM board used for LAGO.

positive amplitude (anode signals) are sent directly through the auxiliary board to maintain their amplitude. The dynode signals from the FEM board are inverted and sent to the ADC board on the PC104 stack to be recorded. The trigger is sent from the stack through the auxiliary board to the FEM board and finally to the ADC.
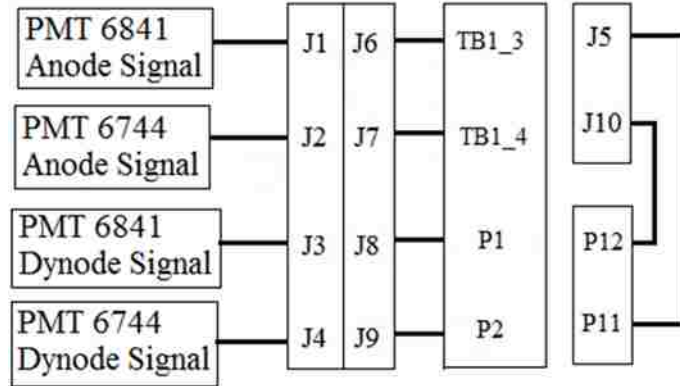

Figure B.4 Wiring Assembly for LAGO FEM and Auxiliary boards.

The high voltage and low voltage required by LAGO are generated by the auxiliary board (Fig. B.5). Both the high voltage and the low voltage converters used on the LAGO auxiliary board require 24 - 32V and ground inputs. This voltage is chosen to match the flight batteries provided by CSBF. As with TETRA, four signal amplifier circuits are used for temperature and relative humidity sensors. These signals are recorded by the ADC board each time a trigger is processed.
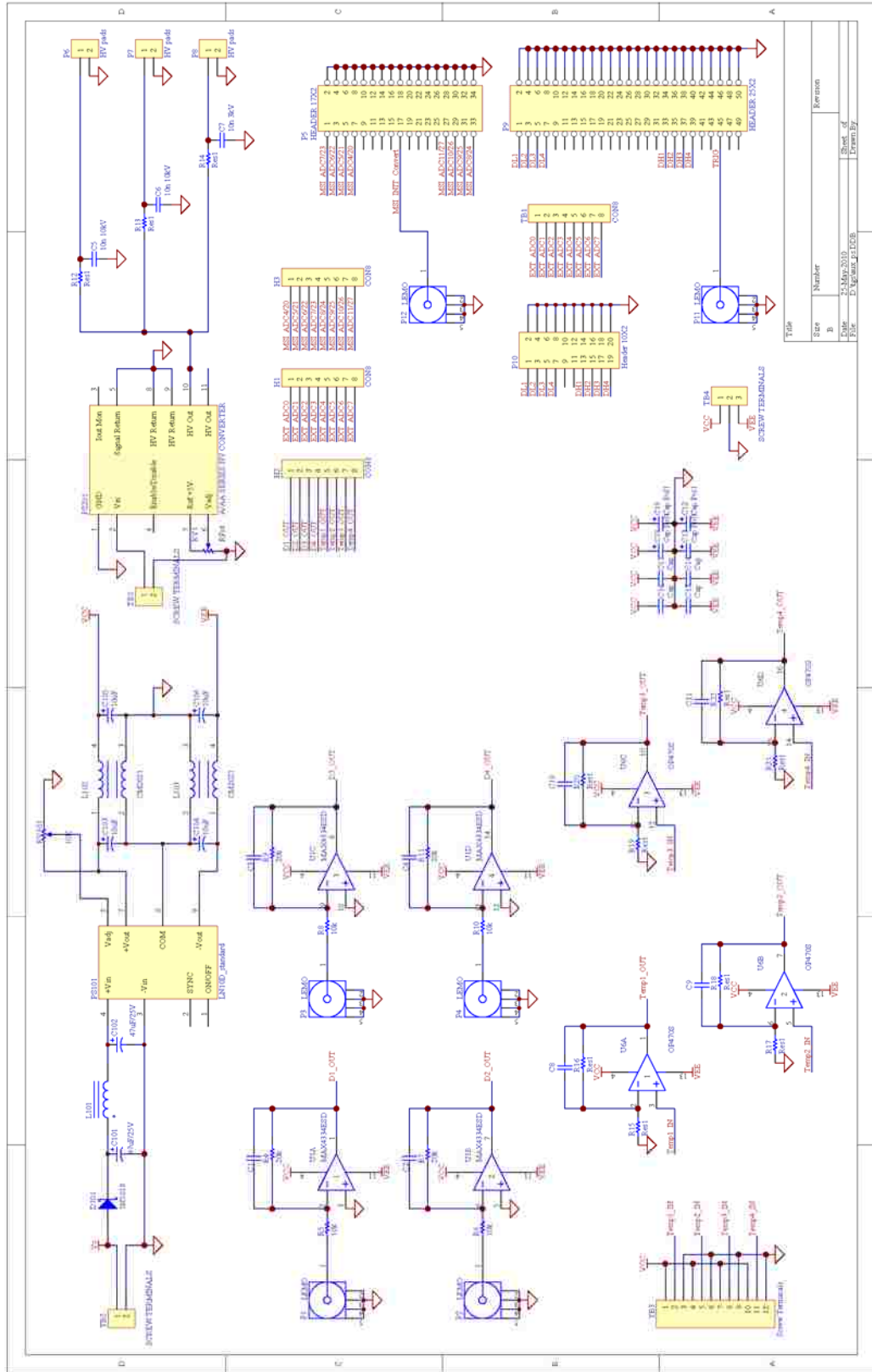
Figure B.5 Circuit diagram of LAGO's auxiliary board.

APPENDIX C – ANALYSIS PROCESS

There are two types of code used to analyze TETRA data: the automated daily analysis and the event analysis packages. The daily analysis process (Run_Daily_Data.prj) is described in chapter 3. The automated package produces a list of potential ECs and various plots, such as those in Figs. 4.1 and 4.3. A similar automated analysis package is used to process LAGO data ('Plot_Det_Balloon.prj'). The DAQ timing behavior described in chapters 5 and 11 was analyzed using 'Time_Test.prj'. This appendix describes the standard analysis of event candidates using the code provided at http://heastro.phys.lsu.edu/lsutgfcode.

The analysis of the event candidates was performed on the entire data set in several steps. First, 'Storm_Processing.prj' is used to ignore triggers occurring on noisy boxes and calculate the live storm time described in chapter 4. Some manual analysis is then performed to keep only ECs detected on boxes where more than one detector was operating. Calibrations are then produced using 'Energy_Histogram.prj' for all dates and boxes that detected an event candidate. 'Alarm_Data_Processing.prj' is then used to analyze each EC, providing various information such as the T_{90} duration, total energy and lightning behavior. This code also produces time history plots and spectra for each event. The time history of each EC must be manually checked to make sure the event detected was observed on more than one detector. This check ensures that noise ECs, such as the one described in chapter 5, are not reported as real ECs. 'Alarm_Data_Processing.prj' is further used to plot the CEC time histories (Fig. 4.6), summed spectra (Fig. 4.7) and EC lightning activity (Fig. 4.8).

Once the event candidates have been analyzed, comparisons must be made between the EC spectra and the background spectra. 'Trigger_Data_Processing.prj' is used to analyze the remaining triggers. Accompanying manual analysis is needed to gather calibrations and remove triggers detected on boxes when only one detector was operating and triggers correlated with calibration visits and ECs. Once the summed trigger spectrum is produced, it can then be compared with the net EC spectrum using plot_spectral_comp.pro (Figs. 4.5 and 5.5).

The significance of the ECs must also be compared to the background to provide statistical confirmation that the events observed are not noise. The program 'Frequency_Sigma_Lightning.prj' is used to calculate the time that the detectors were running (not including noisy days) and the significance of each 2 millisecond bin over the lifetime of the experiment. The significance data are separated into two categories: (1) within ± 7 seconds of lightning within 5 miles of TETRA (storm data) and (2) all other times (background data). The background significance data are scaled by the background run time and then compared to the storm significance data, producing the plots shown in Figs. 4.4 and 5.4. These two data sets are then compared by the Kolmogorov–Smirnov test (ks_test.pro).

The tables shown in chapters 4 and 5 are produced manually. The information for each EC is found in the titles of the daily reports produced by the automated analysis package

and a net output file produced by 'Alarm_Data_Processing.prj'. The timing offset, storm type and probability of CEC must be calculated manually for each event. The timing error for each event can be calculated using 'ec_time_error.pro'. The timing offset must be calculated using the clock files produced by the data acquisition software on each stack. The storm type can be determined with radar images within several hours of the event. The probability of a particular CEC occurring is described in chapter 4. The equation is repeated here: $P_{CEC} = (4 \text{ msec} \times N/86400 \text{ sec})^{b-1}$, where N is the total number of random 20 σ triggers detected per day and b is the number of boxes triggered in the event. Multiplying by the number of ECs then gives the expected number of spurious CECs involving multiple boxes occurring by chance.
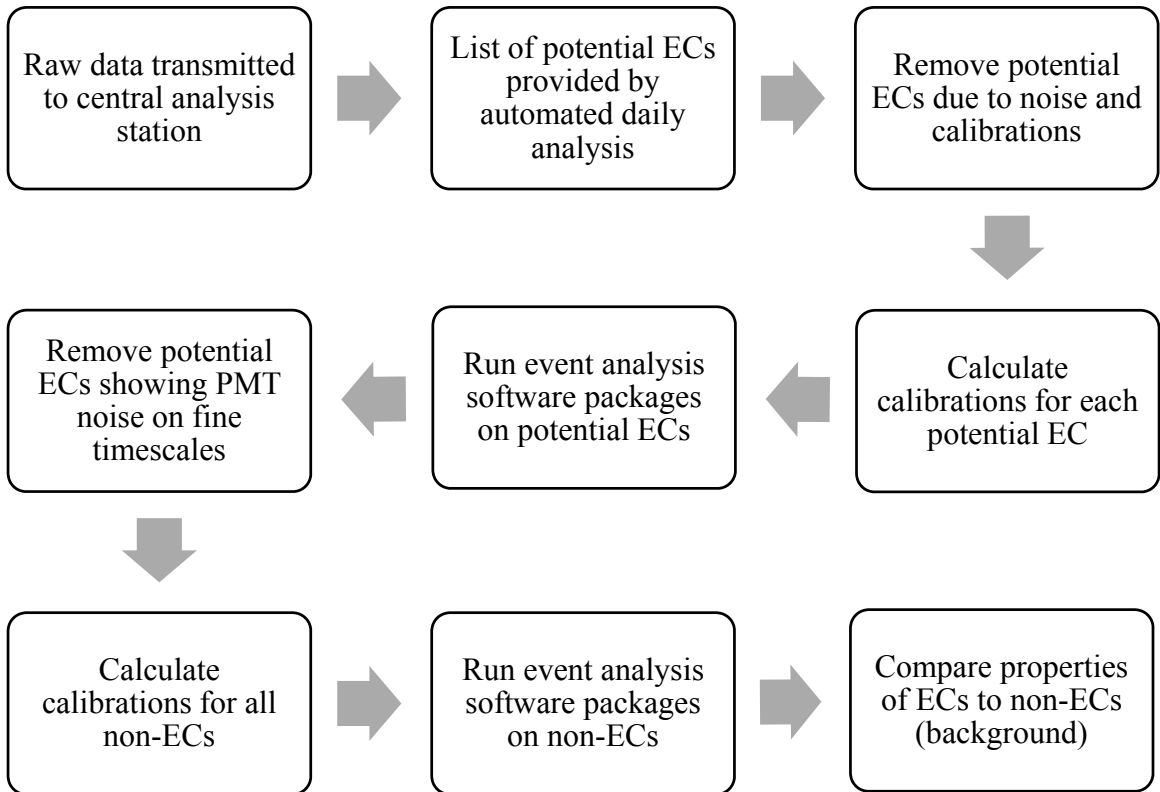
Figure C.1 TETRA Analysis Flowchart

Other calculations reported in this document are the expected number of random ECs and the fraction of 500 keV photons penetrating ~1 mile of atmosphere at STP. The expected number of ECs is calculated by # = (number of clean triggers)*(storm time in hrs)/(total live time in hrs). The second calculation is $N_i/N_{total} = e^{-\rho\sigma x}$, where N_i is the number of 500 keV photons that penetrate the atmosphere without interaction, N_{total} is the number of 500 keV photons that were initially produced, ρ is the density of air at STP, x is equal to 1 mile, and σ is the cross section for photons in air at 500 keV. The uncertainty in the T_{90} determination is calculated using a simple Monte Carlo simulation of the data. The analysis code used for this calculation is included in the software located at http://heastro.phys.lsu.edu/lsutgfcode. These values are reported in chapters 4 and 5.

APPENDIX D – PERMISSION

Link to license: http://creativecommons.org/licenses/by-nc-nd/3.0/

VITA

Rebecca Ringuette of Baton Rouge, Louisiana, received her bachelor's degree at Louisiana State University in 2007. She then served as the Math Program Director at Sylvan's Learning Center in Denham Springs, Louisiana. In August 2008, she returned to Louisiana State University and received her master's degree in 2013. She is a candidate to receive her doctoral degree for the summer of 2014 and plans to teach on the college level and continue research after graduation.